The Thesis Committee for Ahmet Ali Mert
Certifies that this is the approved version of the following Thesis:

Geotechnical Properties, One-Dimensional Consolidation Behavior and Liquefaction Susceptibility of the Glaciolacustrine Clay Samples from the Oso Landslide

APPROVED BY
SUPERVISING COMMITTEE:

Robert Gilbert, Supervisor

Jorge G. Zornberg

Geotechnical Properties, One-Dimensional Consolidation Behavior and Liquefaction Susceptibility of the Glaciolacustrine Clay Samples from the Oso Landslide

by

Ahmet Ali Mert

Thesis

Presented to the Faculty of the Graduate School of

The University of Texas at Austin

in Partial Fulfillment

of the Requirements

for the Degree of

Master of Science in Engineering

The University of Texas at Austin

May 2019

Dedication

For my parents, Nebihe and Arif, who supported me in every way, and believed in me always; for my brother, Alper, who is there as my best friend; and for my wife, Petra, who has been there for me during the whole process.

Acknowledgments

I would like to thank my advisor, Dr. Robert Gilbert, for his guidance and advice throughout this research project, he allowed this research to be a great learning experience for me. I would also like to thank Dr. Jorge Zornberg for his contribution as a reader.

I would like to extend my thanks to the entire Geotechnical Faculty at UT Austin for all their hard work in ensuring that my education meets the highest standards of education. I would like to thank Dr. Hande Gerkus, for always listening to my concerns and helping me work through the problems. I would also like to thank Dr. Chadi El Mohtar and Federico Castro for their guidance in the lab. I would like to thank my colleagues, Hamza Jaffal, Ashim Gajurel, Joseph Vantassel, Jiali Han, Ugur Arslan, and Yucel Alp for sharing their ideas with me and keeping the brainstorming going. I would also like to thank Dr. Krishna Kumar for providing me with valuable information about the Oso Landslide.

Last, but not least, I would like to thank my family, my wife, and my friends, who have helped me through the last years in Austin.

May 2019

Abstract

Geotechnical Properties, One-Dimensional Consolidation Behavior and Liquefaction Susceptibility of the Glaciolacustrine Clay Samples from the Oso Landslide

Ahmet Ali Mert, M.S.E.

The University of Texas at Austin, 2019

Supervisor: Robert Gilbert

Involving a wide range of ground movements, such as rock falls, deep slope failures, and shallow flows of debris, landslides may cause damage to property, injury, and death. Such a landslide occurred in Washington state, near Oso, in 2014. Synthesized available literature on identical soil material was used for the investigation. On the two samples, S1 and D5 from the event site, plasticity tests and one-dimensional consolidation testing were performed.

Main objectives were to compare the volume of the 2014 debris run-out with the volume of the colluvium at the toe of the slope prior to the 2014 slide, to estimate the properties of the colluvium, to explore hypotheses about how the strength of the colluvium reduced enough for it to flow like a liquid, and to provide guidance for future projects to identify the possibility of a large run-out like this event.

To achieve these objectives, a literature review and an experimental program comprised compiling all the available information about the 2014 debris flow, conducting

supplementary laboratory testing on remolded samples from the slope, summarizing the synthesized available literature on the mechanisms of the 2014 debris flow, and investigating hypotheses to explain the Oso debris flow.

Provided the conducted test results and the obtained available data from the literature, two conclusions may be drawn:

1. The debris flow volume included more than only colluvium, with previously in-place materials behind it,
2. It is hard to explain whether the debris flowed like a liquid based on the critical state line, liquidity indices, or undrained remolded shear strengths obtained.

Table of Contents

List of Tables

List of Figures

CHAPTER 1: INTRODUCTION

1.1 Problem Statement

Defined as the movement of a masses of earth (soil), rock, or debris, down a slope (under the impact of gravity) (Cruden, 1991), landslides are causing roughly $3.5 billion in damage, while killing between 25 and 50 people every year in the U.S. (National Research Council, 1985). In Washington state, a landslide occurred in 2014, taking 43 lives and destroying about 50 homes of the Steelhead Drive Community (Fig. 1.1) (Fig. 1.2) (Keaton et al. 2014; Iverson et al. 2015 and Wartman et al. 2016). The 2014 event was about three times higher, compared to three previous landslides at this location in the past 60 years, and involved ten times the volume of material having a run-out seven times further, being the deadliest in the history of the United States. In retrospect, this slope has a risk that is above thresholds to the people below, which is considered acceptable for other landslides in the U.S. However, it is similar to or even smaller than that affiliated with flooding from levees at various locations in the U.S. (Gilbert et al. 2016).

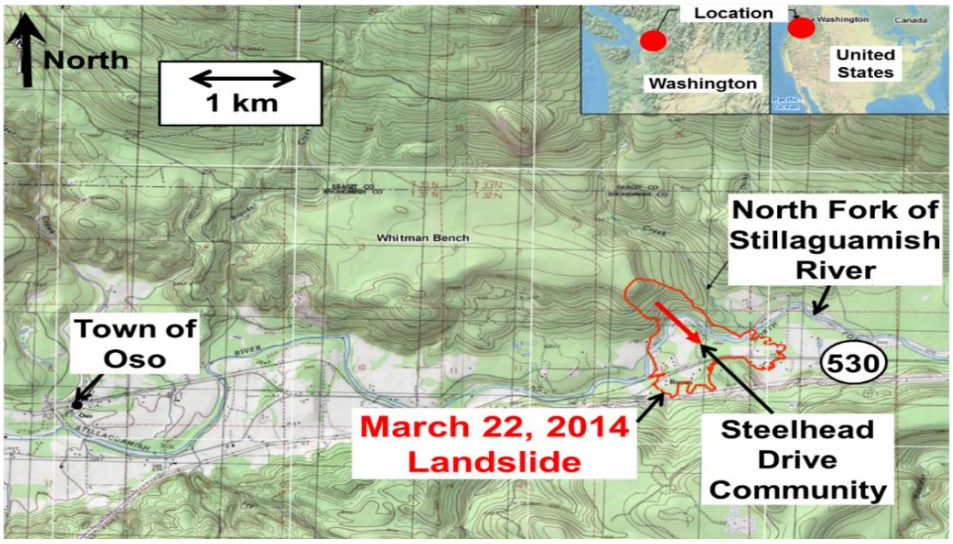

Figure 1.1: Site Plan (from Gilbert et al. 2016)

Figure 1.2: Aerial Photographs of Steelhead Drive Community before and after 2014 Landslide (photos from Google Earth®, from Gilbert et al. 2016)

Given the two-phase failure mechanism related to the 2014 Oso Landslide by Keaton et al. (2014), the first major movement stage is interpreted as remobilizing the 2006 slide mass and a headward extension that included part of the prehistoric slide's forested slope. As such, Stage 1 consisted largely or entirely of previous landslide deposits, along with material from the 2006 landslide and older ancient debris that formed a topographic mid-slope bench. Stage 1, with the first mobilization of the saturated 2006 slide debris could almost coincide with two phases of failure that disrupted the slide debris exposed in the near vertical 2006 head scarp.

Stage 2 was interpreted as to be followed by the unloading (i.e., loss of buttressing) from Phase 1 and the redirection of principal stresses. Stage 2 involves retrogression in a sequence of nested extension failures into the Whitman Bench of approximately 90 meters horizontally from the ancient slide scarp. The slip surface for Phase 2 likely entered the slip surface of Phase 1 (and that of the ancient and 2006 slides) in depth, but formerly, Phase 2 also included previously in-place outwash, till and lacustrine deposits. Stage 2

quickly moved to the more intact headward blocks on the trailing edge of the Stage 1 slide mass and came to rest.

Also, according to another two-phase failure mechanism by Stark et al. (2017), a slide mass located above the frequent landslides in the lower portion of the slope, extending to near the slope crest is included in the first phase. This slide mass with significant potential energy moved downslope and pushed the water-filled colluvium that had accumulated around the slope toe across the valley, resulting in it to flow almost 1.5 km. Removal of the phase I slide mass left the upper portion of the slope unbuttressed and oversteepened. It caused a second landslide (Phase II), but it primarily remained on the main slope, since the back corner of the Phase I slide mass hindered further movement, and the unsaturated and dense upper soils did not undergo a significant strength loss like the water-filled colluvium.

Oso landslide occurred within the Vashon Stade of the Fraser Glaciation, which was in deposits of the final major continental glaciation into the Puget Lowland (Armstrong et al., 1965). In the lower part of the Vashon sequence, the basal slide surface developed mainly within intact glaciolacustrine deposits (Qglv) (Keaton et al., 2014; Badger, 2015; Pyles et al., 2016).

Qglv deposits are typically very stiff to hard, laminated to thinly-bedded, non-plastic silt to fat clay deposits (Mullineaux et al., 1965; Landau Associates, 1998; Badger, 2015 and 2016). The clay fraction consists mainly of illite, smectite, and chlorite (Gault, 2015).

One conclusion can be drawn from the experiments for the advance glaciolacustrine clay that loss of cohesive strength over the long term, rather than the hydroclimatic pressure response of the pores, is the most significant contributor to reduced stability and, in some

cases, the initiation of the first landslides in Qglv deposits. The shear strength and consolidation behavior of the clay must, therefore, be further studied.

Liquefaction potential should also be further investigated to understand the mechanism of the long, progressive run-out, which acted like a liquid and flowed across the valley when sheared by the slide mass pushing on it.

1.2 Research Objectives

The primary objectives of this research are:

- To compare the volume of the 2014 debris run-out with the volume of the colluvium at the toe of the slope prior to the 2014 slide,
- To estimate the properties of the colluvium,
- To explore hypotheses about how the strength of the colluvium reduced enough for it to flow like a liquid,
- To provide guidance for future projects to identify the possibility of a large run-out like this event.

To achieve these objectives, a literature review and an experimental program comprising the following was conducted:

1. Compiling all the available information about the 2014 debris flow,
2. Conducting supplementary laboratory testing on remolded samples from the slope,
3. Summarizing the synthesized available literature on the mechanisms of the 2014 debris flow,
4. Investigating hypotheses to explain the Oso debris flow.

1.3 Organization of Thesis

This document consists of six chapters. After this introduction, Chapter 2 provides a literature review of previous research. The literature review covers information about the relationships between Atterberg limits and liquidity index and remolded shear strength, empirical run-out mobility predictions, liquefaction and cyclic mobility, liquidity index, sensitivity and effective consolidation stress, rainfall-induced debris flows, field stress path and the stress transfer, one-dimensional consolidation and void ratio, and the steady-state lines for soils with various fines content and the description of the intrinsic compression line and other hypotheses that might have led to the 2014 debris flow.

Background on Oso landslide, along with the geotechnical properties of the advance glaciolacustrine clay in the Qglv deposits and synthesized available data from the literature were presented in Chapter 3.

Investigation of the colluvium by comparison of the colluvium volume with the run-out, and the experimental program, with test results and pre-analyses were presented in Chapter 4.

In Chapter 5, the given hypotheses about the cause of the liquefaction was investigated to understand how the colluvium acted like a liquid and flowed across the valley when it was sheared. Using the correlations for liquefaction susceptibility, an attempt was made to examine the agreement of the tested specimens with those descriptions of mechanism. The conducted tests are also used to utilize the data from the literature, and to determine if the information available is consistent with that description of the mechanism, and with our data.

Lastly, the six chapter concludes the document with conclusions and summaries. Recommendations for future research are provided, as well.

CHAPTER 2: LITERATURE REVIEW

2.1 Introduction

This chapter provides background information on the scope and purpose of this thesis. The empirical run-out mobility predictions for debris flows and Oso landslide is discussed. Liquefaction and cyclic mobility, liquidity index, sensitivity and effective consolidation stress, rainfall-induced debris flows, field stress path and the stress transfer, one-dimensional consolidation and void ratio, and the steady-state lines for soils with various fines content and the description of the intrinsic compression line and other hypotheses that might have led to the 2014 debris flow are also presented. The relationships between Atterberg limits and liquidity index and remolded shear strength and water content are subsequently investigated. A further description for the debris flows and the deposition are also included. The literature review aims to discuss the published information, particularly within the subject of the thesis.

2.2 Empirical Predictions for Run-Out Mobility

In order to assist decision-makers with hazard zoning and possible mitigation actions, a clear understanding of the mechanics of debris flows and flow slides is essential to model the effects of this type of failure. However, there is a lack of full understanding of how flow slides keep the ability to move long distances over low-angle slopes at high speeds. Their mobility depends heavily on the presence of water in the sliding mass, the nature and volume of the slide mass, the size and nature of the debris involved in the flow, the slope angle in the failure zone, the slope angle and ground surface roughness and constraints / obstacles in the run-out zone, and the presence of any water bodies along the run-out zone, such as entrainable river or stream flow (Keeton et al., 2014).

There are two issues involved: 1) slide triggering and 2) high-velocity, unstable, non-uniform subsequent motion. As far as triggering is concerned, a high degree of saturation appears to be required in the pre-slide failure zone; one basic scenario would be that, as pore pressure increases due to a rising groundwater table, the effective stress decreases and thus the shearing resistance on the potential failure plane decreases, allowing the slope to fail and the sliding material to mobilize (Anderson and Sitar, 1995). While many landslides can be modeled as solid blocks sliding over defined surfaces of failure, ultimately debris flows mobilize the entire mass of sliding material as a viscous flow with distributed shear.

The assessment of run-out distances is based on several factors including sliding mass volume, slope height, slope angle, type of geological material, site topography and morphology, obstructions, distribution of grain size, water content, saturation degree, strength parameters, and types of failure. Determination of run-out distances continues to be highly empirical but critical to zoning for safe development. Methods for predicting run-out distances were developed using volumes of landslides, which could potentially expand by 10 to 30% compared to in-place material (Jaboyedoff et al., 2008). The methods are simple and are based on historical data from events with broad changes in materials, conditions and morphology. The significant scattering of past events observed results in estimates which cannot be used with great certainty in practice (McDougall, 2006). Analytical prediction methods were also developed and can improve empirical estimates in some cases. The analytical methods are however complex and require knowledge and/or several parameters to be estimated. Analytical method discussion is beyond the scope of this thesis. As the initial failed mass travels downhill collecting surface materials, trees, scouring the landscape, and incorporating water from valley sediments and water bodies such as creeks and rivers, run-out distances are also greatly influenced by material

entrainment. Run-out distances are also affected by various obstacles in the run-out area of debris which can either shorten or increase the distance due to channelization. Water, silt and clay tend to promote larger run-out distances. As the content of silt and clay increases, it helps to maintain high water pressure in the debris flow (Iverson, 2003). Wang and Sassa (2001) found, using a number of flume experiments, that these high excess pores occur after failure, rather than before failure.

The reach angle (α) or angle of travel, also known as fahrböschung (Heim, 1932), is an angle from the top of the scarp to the distal edge of the debris flow (Fig. 2.1) and can be used to estimate the run-out distances on a volume basis, V. The landslide geometry indicates the landslide height (H) ratio to the horizontal distance between the top of the landslide and the distal edge (L) as tan (α).

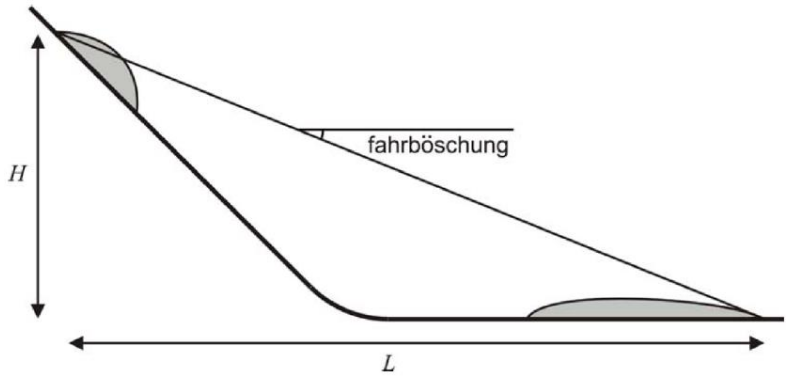

Figure 2.1: Definition of fahrböschung or angle of reach (from McDougall, 2006)

The travel angle chart is shown in Fig. 2.2 as a function of the volume of a landslide (note that the angle of travel is displayed indiscriminately as α and β). The trend also shows that the run-out is increasing for the same volume as the tan (α) decreases. Due to sliding stages, spreading of the debris flow to the east and west of the Oso Landslide, and the incorporation of river water from the Stillaguamish North Fork, estimating the run-out

length is a difficult task. Furthermore, the initiation point for Stage 1 can only be estimated, making it difficult to assess the volume of debris in Stage 1. Corominas (1996) used debris slides, debris flows and avalanches to develop an empirical relationship between the angle of reach and the volume of the debris flow, V:

$$\boldsymbol{tan(\alpha) = \frac{H}{Lmax} = 0.97V^{-0.105}}$$

Hungr et al. (2005) subsequently revised the term by a landslide type, which resulted in a slightly better relation between debris flows as reflected in the regression coefficients given in Table 2.1.

$$\boldsymbol{log(tan(\alpha)) = A + Blog(V)}$$

Landslide Type	Paths	A	B	R^2
Debris Flows	All	-0.012	-0.105	0.76
	Obstructed	-0.049	-0.108	0.85
	Unobstructed	-0.031	-0.102	0.87

Table 2.1: Regression Coefficients (from Hungr et al., 2005)

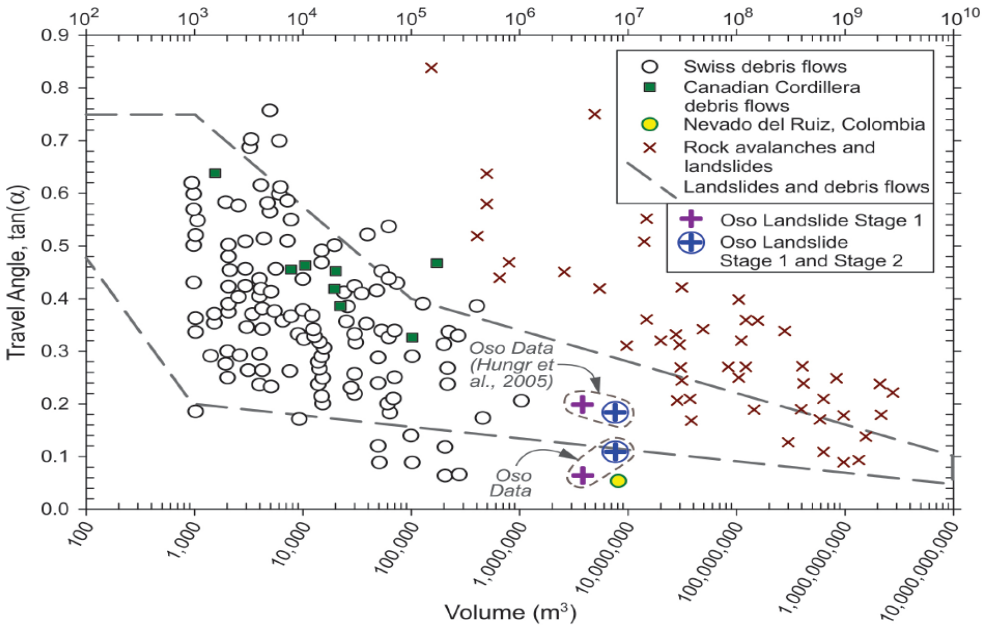

Figure 2.2: Travel Angle vs. Volume of Mass Movement (from Jakob and Hungr, 2005)

The maximum run-out distance was estimated by Rickenmann (1999) on the basis of data from 154 debris flow events as showed in the following equation:

$$\boldsymbol{Lmax = 1.9V^{0.16}H^{0.83}}$$

Legros (2002) has suggested a relationship between landslide run-out length and volume instead of the apparent friction angle (H / L). He argued that in predicting run-out length the H / L ratio is physically meaningless and thus proposed a relationship based on volume (V in km^3) rather than falling height. Equation below, with coefficients c and n given in Table 2.3 represents the general form of his power-law equations for volcanic and non-volcanic landslides and debris flows:

$$\boldsymbol{Lmax = cV^n}$$

Event Type	c	n
Non-volcanic	8	0.25
Volcanic	15.6	0.39
Debris Flow	235	0.39

Table 2.2: Empirical Relationship Parameters of Legros (2002)

Landslides tend to form into debris flows due to adequate fluid input and thus increase in mobility (Iverson, 1997).

The observations made at Oso landslide considered the possibility of a two-phase failure as well as a single phase that includes the whole slide mass, using these various formulations. L_{max} can be measured for Phase 1 of the Oso Landslide in cross sections shown in Fig. 4.2 and it is estimated at 1433 m (4700 ft) in height H equal to 90 m (300 ft). The L value of the two phases is 1677 m (5500 ft) and H is 182.9 m (600 ft). The total volume of the Oso landslide can be estimated at approximately 7.6 million m^3 (9.9 million yd^3), with the estimated volume of Stage 1 at 50–85 % of the total. Using values given in Table 2.2, using the equation from Rickenmann (1999) for the predicted run-out underestimates run-out for a two-phase failure, but with the less probable one-stage failure, it agrees well. Results after using Legros (2002) method and equation for the volcanic debris flows, shows the observed run-out in a closer agreement with the volume of Stage 1 being 50% of the total slide volume. These predictions endorse the possibility that a two-phase event occurred and is consistent with the recorded seismic signals (Keaton et al., 2014). The power-law relationship of Legros (2002) for debris flows led to unreal run-outs of more than 35 kilometers. Overall, these other empirical procedures seem to predict the observed run-out distances reasonably well.

Fig. 2.2 illustrates the angles of travel derived from the improved expression of Corominas (1999) given in Hungr et al. (2005) and the calculated values from Oso

landslide. The results suggest that the prediction method for Oso Landslide based on the total volume of 7,6 million m^3 (9,9 million yd^3) gives a traveling angle as Corominas predicts. However, the supposed travel angles for the Stage 1 and Stage 1 and 2 cases fall below or are similar to Swiss Alpine debris flows at the Corominas' line lower bound.

Failure Scenarios	Volume (km^3)	H (m)	tan (α)	tan (α) Hungr et al. (2005)	Measured L_{max} (m)	Predicted L_{max} (m) Rickenmann (1999)	Predicted L_{max} (m) Legros (2002)
Total Volume	0.0076	183	0.109	0.185	1675	1808	2326
80% of Total	0.00608	92	0.064	0.189	1435	982	2132
50% of Total	0.0038	92	0.064	0.199	1435	910	1775

Table 2.3: Predicted Run-out Distances for 2014 Oso Landslide based on Estimated Total Volume of $7.6x10^3$ m^3 ($268x10^6$ ft^3) (from Keaton et al., 2014)

Legros (2002) for volcanic landslides, and Hungr et al. (2005) for unobstructed debris flows were used for the predictions.

2.3 Liquefaction and Cyclic Mobility

2.3.1 Liquefaction and The Critical State Line (CSL) Definitions

Castro and Poulos (1977) describe liquefaction as a phenomenon in which a saturated sand loses a high percentage of its shear resistance (due to cyclic or monotonic loading) and flows like a liquid until the shear stresses that act on the mass are as low as its reduced shear strength. Thus, according to their description, a liquefying slope would not come to rest until the slope has been reduced to a few degrees, and a building with its liquified foundation soil will float or sink until the shear stresses in the foundation are coherent with the reduced shear resistance. They also called the state in which a soil sample is flowing at constant effective minor principal stress, under constant shear stress and at constant volume (later modified to include the constant velocity requirement by Poulos

(1981)), “steady-state of deformation”, and the relationship between the void ratio and the steady-state effective stress the “steady-state” line.

Casagrande (1969) presented the definition of cyclic mobility as the progressive softening of a saturated sand specimen under constant water content cyclic loading. According to Castro and Poulos (1977), in laboratory tests, the large strains resulting from cyclic mobility on dilative sands are mainly due to the redistribution of the void ratio in the specimen during cyclic loading. The steady-state line shown in Fig. 2.3 represents the locus of states where a soil can flow at a constant effective minor principle stress, constant void ratio, constant shear stress, and constant velocity.

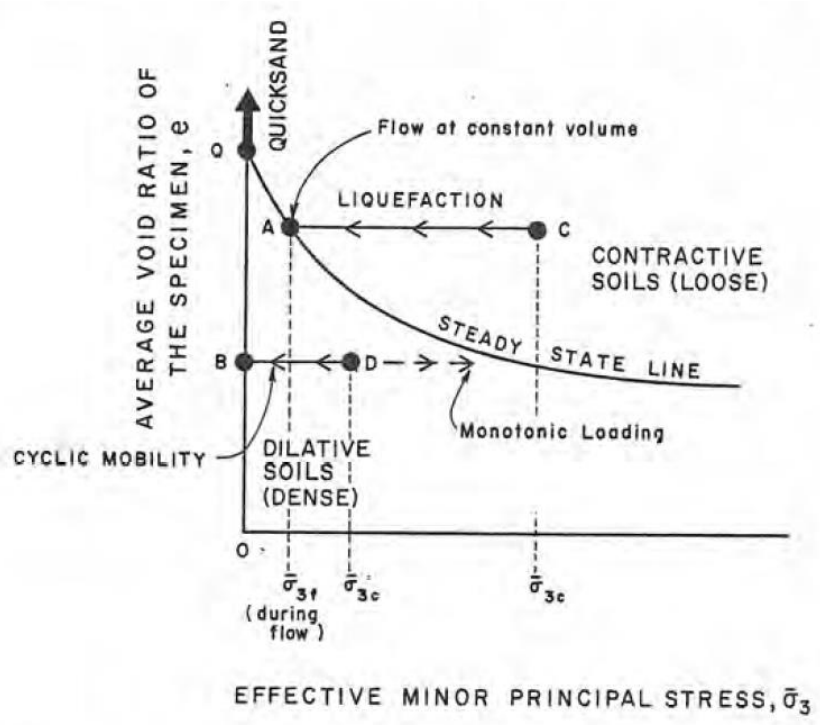

Figure 2.3: State Diagram for Undrained Tests on Fully Saturated Sands (from Castro and Poulos, 1977)

As they define, if the cyclic stresses are sufficiently large, in the laboratory, any soil in any state can develop cyclic mobility, while liquefaction is to occur most likely in uniform fine clean loose sand. Static loads or cyclic loads that cause shear stresses larger than the steady-state strength may cause liquefaction.

2.3.2 STATIC LIQUEFACTION AND BRITTLENESS INDEX FOR THE RESIDUAL UNDRAINED SHEAR STRENGTH

Poulos et al. (1985) express the factor of safety against the initiation of static liquefaction as:

$$F.S. = \frac{Required\ shear\ stress\ to\ initiate\ liquefaction}{Developed\ shear\ stress\ by\ loading\ in\ soil\ mass} = \frac{\tau f}{\tau d}$$

As Kramer and Seed (1988) suggest, liquefaction results in a reduction in soil shear strength that may be small or large. After the initiation of liquefaction, the magnitude of the strength loss does not directly affect the factor of safety against liquefaction initiation, but on the consequences of liquefaction, it has a significant effect. In the process of an element deforming until it reaches the steady-state of deformation, after the initiation of liquefaction, the shearing resistance drops to the steady-state shear strength from the peak undrained shear strength. The difference between the residual and the peak shear strengths define the amount of deformation that is required to reach equilibrium conditions. Flow sliding may develop if the reduction in shear resistance is large. If the discussed factor of safety is greater than one, flow sliding will not occur.

Bishop (1967) indicated that the undrained strength of a strain-softening material was reduced in terms of a "brittleness index" defined as:

$$IB = \frac{\tau f - \tau r}{\tau r}$$

where τ_r = residual undrained shear strength; and τ_f = peak undrained shear strength as shown in Fig. 2.4.

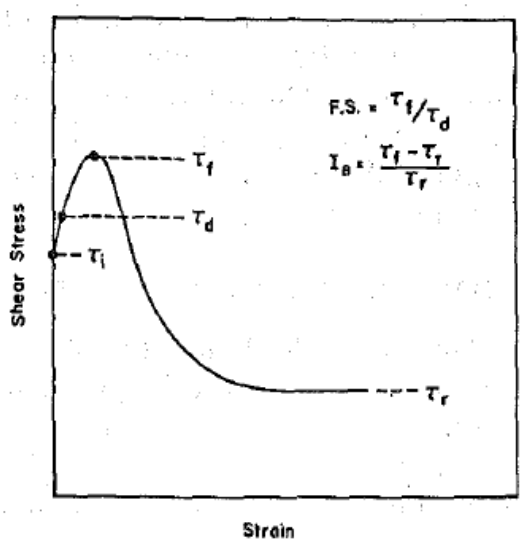

Figure 2.4: Stress-Strain Diagram for the Previously Discussed Factor of Safety and Brittleness Index Definitions (from Kramer and Seed, 1988)

The residual shear strength has also been described by other researchers as the steady-state shear strength. Effects of liquefaction will strongly be influenced by Bishop's "brittleness index" (Kramer and Seed, 1988).

Natural clay-like soil sensitivity can be related to soil liquidity index (LI) and effective consolidation stress (Boulanger and Idriss, 2004). Soft normally consolidated or lightly overconsolidated clays will typically have higher natural water content, higher LI values, and higher sensitivities ($S_t > 8$), and are therefore most likely to lose strength during shearing. Well compacted and heavily overconsolidated clays will have reduced natural water content, lower LI values, and generally be much less sensitive to remolding.

2.3.3 PLASTICITY INDEX FOR ESTIMATING LIQUEFACTION POTENTIAL OF CLAYEY SANDS

In their technical note after performing undrained cyclic stress-controlled ring-shear tests, Gratchev et al. (2006) indicate that an increase in plasticity index (PI) decreased the soil liquefaction potential, and, consistent with the results of other researchers, a soil with PI>15 seemed to be non-liquefiable. These tests were carried out on artificial sand mixtures with different clays saturated with water.

2.3.4 LIQUEFACTION OF COHESIVE SOILS (PERLEA, 2000)

Sand, with some fine contents or clean, has been thoroughly studied for liquefaction, and liquefaction is currently a reasonably predictable phenomenon. Study of the behavior of cohesive soils during and immediately after cyclic loading is particularly difficult because of their structural variability and the significant impact on the dynamic properties of structural characteristics. This leads to the testing of reconstituted samples of little interest in natural deposit evaluation. There are various categories of potentially liquefiable cohesive soils, which are considered: silty clays or clayey silts of low plasticity meeting the “Chinese Criteria”; collapsible loess; highly sensitive clays. In the report, natural materials with at least 50% fines (particles passing the 75μm sieve), the plasticity index (PI) of at least 4, and any measurable liquid limit (LL), are considered cohesive soils.

In China, during strong earthquakes from 1966 to 1976, especially during Haicheng (1975) and Tangshan (1976) earthquakes, as observed through the ejection of liquefied soil to the ground surface, many cohesive soil deposits liquefied. The cohesive soils liquefied had: liquid limit between 21 and 35, plasticity index from 4 to 14, less than 20% clay fraction, and higher water content than nine-tenths of the LL (Wang, 1979). In Japan, Kishida (1969) noted liquefaction of soils up to 70% fines and 10% clay, while Tohno and Yasuda (1981) reported soil liquefaction with up to 90% fines, and 18% clay fraction.

Japanese standards consider easily liquefiable soils with up to 25% clay fraction and up to 100% fines (Japan Society of Civil Engineers, 1977).

In the United States, a liquefaction of "very silty" hydraulic fill sands was attributed to the upstream flow slide failure in lower San Fernando Dam following the 1971 San Fernando earthquake (Seed et al., 1989). Investigation of the effects of the Izmit earthquake in Turkey (August 1999, local magnitude of 7.4) revealed that buildings in Adapazari (30 km epicentral distance) rotated up to 50 degrees or sank to a depth as much as 2 meters, due to liquefaction of sand-silt-clay soil mixtures and silts (Hynes,1999).

One of the three identified categories of liquefiable soils based on observations during Chinese earthquakes by Wang (1981) was; soft clays with the unconfined compressive strength less than 0.5 daN/cm^2, the liquidity index greater than 0.75, sensitivity above 4, and SPT blow counts less than 4. Fig. 2.5 shows the adapted Chinese criteria to ASTM definition of soil properties for liquefaction.

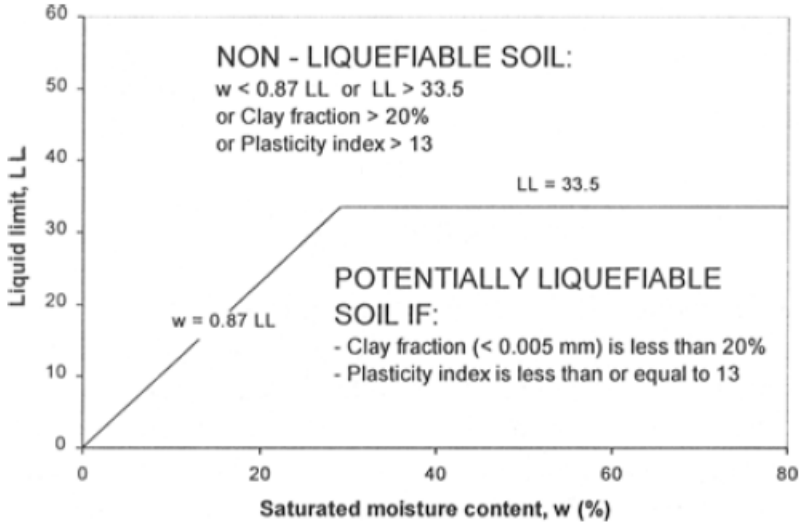

Figure 2.5: Adapted Chinese Criteria to ASTM Soil Properties Definition (from Perlea, 2000)

Particular Liquefiable Soils: Sensitive (Quick) Clays

As another example of natural soil deposit, sensitive clay is already on the verge of collapse before an earthquake which can induce its failure. The term sensitivity refers to the undrained shear strength loss which may develop due to disturbance of the undisturbed specimen structure. It is measured by the sensitivity ratio, S_t = Peak undisturbed strength / Remolded strength. The strength is usually determined by in-situ vane test, and in the laboratory through unconfined compression test. Clays with S_t = 2 to 4 are considered medium sensitive, while $S_t > 8$ defines quick clay. The flocculated structure and the slight cementation require very little strain to break the bonds in sensitive clay at particulate contacts. If saturated sensitive clay is remolded under undrained conditions, the structure is disintegrated and the pore water is increased, thus reducing the undrained strength dramatically.

There are many examples of liquefaction and subsequent mud-flow failure of sensitive clay, particularly in overconsolidated deposits, in non-earthquake actions. Like other disturbance sources, the earthquake can cause slides in gentle sloping sensitive clay deposits. The landslides at Anchorage during the 1964 Alaska earthquake were among the best-documented cases of seismic induced clay failures (Stark and Contreras, 1998; Olsen, 1989; Idriss, 1985). The clay had the following characteristics on average: PI = 14-17, LL = 37-39, OCR = 1.2, clay-size fraction (<0.002mm) = 58%, peak undrained shear strength ratio $S_u/\sigma_{vc}' = 0.23$-0.28, residual undrained shear strength ratio $S_r/\sigma_{vc}' = 0.06$-0.07, and sensitivity ratio, $S_t = S_u/S_r = 3$-4 (by direct simple shear or constant volume ring shear test). Back analyses show that in various portions of the landslides, the mobilized undrained strength varied between at least 80% of S_u and the residual strength, S_r.

2.3.5 GRAIN SIZE DISTRIBUTION, WATER CONTENT, AND PLASTICITY

2.3.5.1 Chinese Criteria

Described earlier, the "Chinese Criteria" were the first criteria for liquefaction susceptibility screening for fine-grained soils in the United States (Wang 1979). The soils falling in the Chinese Criteria seem to have the characteristics illustrated in Fig. 2.5.

	LL[1] < 32	LL[1] > 32
Clay Content[2] < 10%	Susceptible	Further Studies Required (*Considering non-plastic clay sized grains – such as mica*)
Clay Content[2] ≥ 10%	Further Studies Required (*Considering non-plastic clay sized grains – such as mine and quarry tailings*)	Not Susceptible

Table 2.4: Modified Chinese Criteria proposed by Andrews and Martin (2000)

Andrews and Martin proposed modified Chinese Criteria limits, based on differences in index tests in Chine and the USA (Table 2.4). The liquid limit is determined by Casagrande-type percussion apparatus and clay is defined as grains finer than 0.002 mm.

2.3.5.2 Seed et al. (2003)

Seed et al. (2003) propose the criteria shown in Fig. 2.6 based on post-earthquake observational data combined with subsequent laboratory tests. In this figure, three zones, zones A, B and C, are identified which relate to different levels of susceptibility to classic cyclic liquefaction, which they define as the significant loss of strength and stiffness caused by the cyclic pore pressure generation. They further distinguish “classic cyclic liquefaction” (i.e., liquefaction triggering) from “sensitivity”, where the latter was defined

as the strength loss due to monotonic shearing and/or remolding as a result of larger, unidirectional shear deformations. The plasticity index (PI) is used in place of the percent clay fines used in the Chinese Criteria in Seed et al. (2003) criteria, whereas w_n (or w_c) and LL are still part of the criteria. Only Zone A soils in the Seed et al. (2003) criteria are considered likely susceptible to liquefaction triggering and may be evaluated by the simple procedure (e.g., Youd et al. 2001). Soils falling into Zone B might be susceptible to liquefaction triggering. In many cases, however, the simpler procedure does not allow for evaluation but must instead be sampled and tested in the laboratory. Finally, zone C soils (i.e., outside of Zone A and B in Fig. 2.7) are not generally considered susceptible to liquefaction triggering but might be sensitive.

The criteria Seed et al. (2003) do specify the applicability as a function of fines content (FC), as opposed to the Chinese criteria that do not. The criteria of Seed et al. (2003) apply: FC $\geq$ 20 percent if PI > 12 percent and FC $\geq$ 35% if PI < 12%. These limitations are consistent with Polito & Martin's (2001) and Thevanayagam et al. (2002) concept of "limiting" fines content (FC_L). In this context, when FC > FC_L, the coarse grains "float" in the soil matrix of fine grain and the behavior of a soil whose FC is larger than FC_L is clearly different from that of a soil whose FC is less than FC_L.

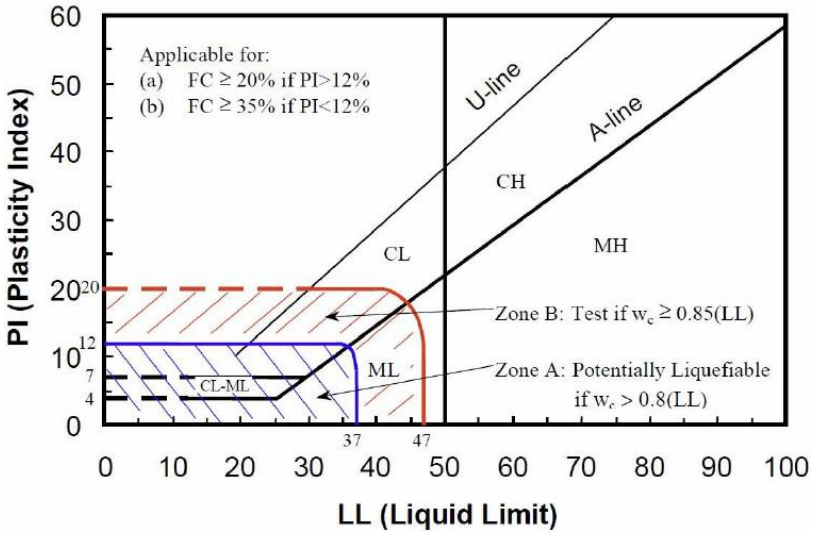

Figure 2.6: Criteria Proposed by Seed et al. (2003) for Liquefaction Susceptibility

2.3.5.3 Bray and Sancio (2006)

Based also in conjunction with subsequent laboratory tests on post-earthquake observational data, Bray and Sancio (2006) proposed criteria for liquefaction susceptibility of fine soil; their criteria are illustrated in Fig. 2.7. Three zones are identified in this figure: not susceptible, moderately susceptible and susceptible. By Bray and Sancio (2006), soils in the 'susceptible' zone are considered to have potential liquefaction triggers where liquefaction triggering is defined according to Youd et al. (2001): 'liquefaction is a dramatic loss of strength resulting from increased pore water pressure and decreased efficient stress.' Soils that fall in the area of "non-susceptible" are not considered to be susceptible to liquefaction, but are sensitive (i.e., considerable reductions in strength after remolding). As in the Seed et al. criteria (2003), the Bray and Sancio (2006) criteria have an intermediate zone between 'Susceptible' and 'Not susceptible', as indicated by Figure 2.7 as 'Moderately Susceptible'. Caution is taken from Bray and Sancio (2006) that many factors are responsible for controlling the cyclical behavior of fine-grained soil and they recommend

sampling and testing of soils falling into the 'Susceptible' and 'Moderately Susceptible' areas to assess their strain potential and liquefaction susceptibility. This contrasts with the criteria of Seed et al. (2003) for a simplified procedure for evaluating Zone A soils' liquefaction potential where Zone A soils in Seed et al. (2003) criteria are somewhat analogous to 'susceptible' soils in Bray & Sancio (2006).

Finally, the Bray & Sancio (2006) criteria are founded on data for soils with a mainly FC ≥ 50 percent (Bray & Sancio 2008), which should be far beyond the FC_L, irrespective of PI. The Bray&Sancio (2006) criteria should therefore be assumed to apply only to soils with a FC ≥ FC_L.

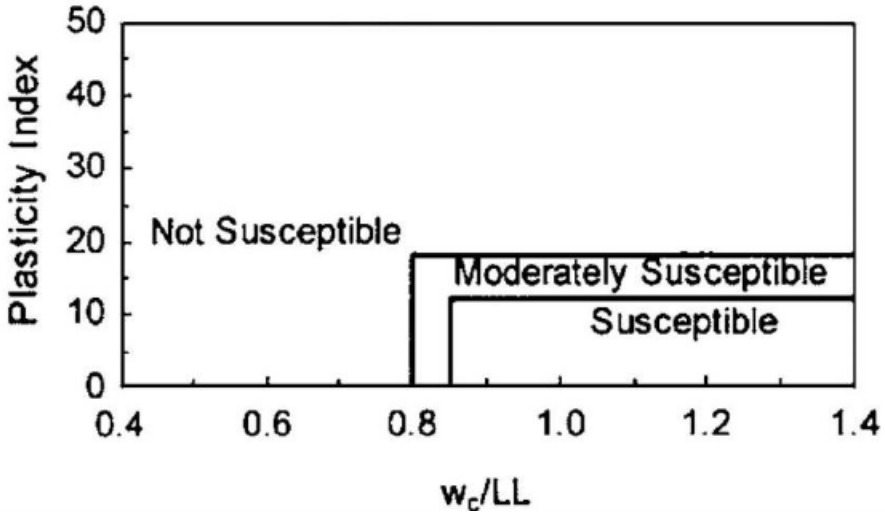

Figure 2.7: Criteria Proposed by Bray and Sancio (2006) for Liquefaction Susceptibility

2.3.6 Atterberg Limits and Remolded Shear Strength—Water Content Relationships

- **A Recent Approach for the Relationships**

O'Kelly, 2013 uses published regression analyses to draw generalized conclusions regarding soil strength variation with water content (w). These include s_{ur} values mobilized

for the Casagrande liquid limit (LL) and plastic limit (PL), and therefore the variation in shear strength across the plastic range. Many of which assuming a strength variation of 100 over the plastic range, reported methods to deduct strengths from water content (w) measurements at Atterberg limits are examined. Regression analysis of logw: $\log s_{ur}$ correlations for four organic sediments and 14 mineral soils indicated that there are generally no 100 variations in strength and that they may vary significantly among the soils. A new approach to predict remolded undrained strength values mobilized for different water contents is therefore proposed. The approach proposed is based upon direct strength measurements and water content in two test specimens, whereas existing formulations are based on empirical s_{ur} values associated with Atterberg limit values.

In many geotechnical applications, including pile design, submarine soil investigations for offshore structures and glacial soil study, the remolded undrained shear strength (s_{ur}) is of importance (Kayabali and Tufenkci 2010).

Reference	Equation (s_{ur}, in kPa)	
Wroth and Wood (1978)	$s_{ur} = 170\exp(-4.6I_L)$	(1*a*)
Leroueil et al. (1983)	$s_{ur} = 1/(I_L - 0.21)^2$	(1*b*)
Locat and Demers (1988)	$s_{ur} = (19.8/I_L)^{2.44}$; $I_L > 1.0$	(1*c*)
Hirata et al. (1990)	$s_{ur} = \exp(-3.361I_L + 0.376)$	(1*d*)
Terzaghi et al. (1996)	$s_{ur} = 2(I_L)^{-2.8}$	(1*e*)
Yilmaz (2000)	$s_{ur} = \exp(0.026 - 1.21I_L)$	(1*f*)
Koumoto and Houlsby (2001)	$s_{ur_{FC}} = \exp\ [(1.070 - I_{LN})/0.217]$	(1*g*)
NGI (2002)	$s_{ur} = 4.2(I_L)^{-1.6}$	(1*h*)
NGI (2002)	$s_{ur} = 3.9(I_L)^{-2.0}$	(1*i*)
Yang et al. (2006)	$s_{ur} = 159.6\exp(-3.97I_L)$	(1*j*)

Table 2.5: Selection of Published Correlations of Strength – Water Content for Remolded Soils [Note: Eqs. 1a and 1g are based on $s_{ur(LL)}$=1.7 kPa and R_s=100; a dynamic $s_{ur(LL)}$=1.38 kPa mobilized for the 60 g-60° fall cone, with LL defined by a cone penetration depth of 11.5mm and assuming R_s=100, respectively. (from O'Kelly, 2013)]

From the theoretical analysis of cone penetration, which combines penetration resistance with strength in the fall cone test, and builds on relations after Butterfield (1979), Koumoto and Houlsby (2001) suggest the empirical result:

$$w = asur^{-b}$$

where the coefficient a (%) corresponds to s_{ur}=1 kPa water content, and b is the gradient of the water content of the strength correlation represented in a bi-logarithmic plot (see Fig. 2.8). The coefficient a in the equation relates to soil water absorption/water retention and therefore mainly depends on grading and mineralogy, the shape, the texture of the surface and the clay mineral activity, while the coefficient b relates to the compressibility of the soil.

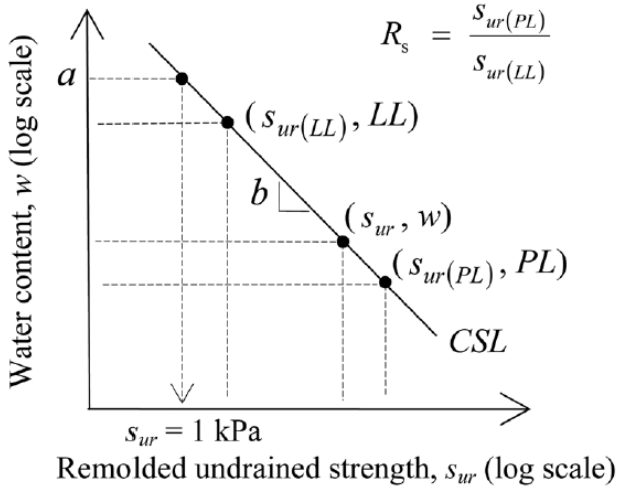

Figure 2.8: Water Content (%) against Remolded Undrained Strength (kPa) for Saturated Soils [Note: CSL is the projection of the critical state line (from O'Kelly, 2013]

This logw: $\log s_{ur}$ relationship has also been examined and reported to be valid for both amorphous organic and fine-grained mineral soils across the complete plastic range (Zentar et al. 2009; O'Kelly 2013a). Measuring very low strength values mobilized for LL

water content is a problem, with reports of values invariably determined through miniature vane tests although the interpretation of these data is open to question (Koumoto and Houlsby 2001; Kayabali and Tufenkci 2010). It is open to debate whether the vane failure mechanism in the soil is the same in its LL and PL conditions. Unconfined triaxial compression tests on water contents around the LL state are not possible. Specimen preparation is difficult for the PL condition because of the general stiff consistency of the soil, and the saturated specimens are also challenging to prepare. Reconstituted at PL, unsaturated specimens would mobilize strengths greater than $s_{ur(PL)}$.

Hence, instead of measuring $s_{ur(LL)}$ and $s_{ur(PL)}$ values directly for a wide range of soils, a different approach was decided in the study (O'Kelly, 2013). As a result, new parameters for relative water content W_{LN} and relative strength Is_{ur} are presented and defined as:

$$\boldsymbol{WLN} = \left(\frac{\boldsymbol{logw - logwA}}{\boldsymbol{logwB - logwA}}\right)$$

$$\boldsymbol{Isur} = \left(\frac{\boldsymbol{logsur - logsurB}}{\boldsymbol{logsurA - logsurB}}\right)$$

where w_A and w_B are corresponding water contents, $s_{urA,}$ and s_{urB} are the measured undrained strengths of test specimens A and B, respectively, with $w_A<w_B$. It should be noted that the W_{LN} and Is_{ur} values have purely relative importance and are not linked to any standard test or procedure. The W_{LN} against Is_{ur} relationship is linear, since the logw: $logs_{ur}$ relationship is also linear, with these parameters in reverse connection by:

$$\boldsymbol{Isur} = \mathbf{1} - \boldsymbol{WLN}$$

$$\boldsymbol{Iogsur} = (\mathbf{1} - \boldsymbol{WLN})\left(\boldsymbol{log}\left(\frac{\boldsymbol{surA}}{\boldsymbol{surB}}\right)\right) + \boldsymbol{logsurB}$$

- **Conclusions**

There is no unique value of the undrained strength that can be assigned at Casagrande LL or PL for soils. Regression analysis of the logw: $logs_{ur}$ correlations of the different soils indicated that the strength of R_s may be very varied, considering R_s=43–128 (average of 75) for 14 mineral soils and R_s=10–27 (average of 18) for four organic sediments. Strengths obtained at Casagrande LL and PL were within the range of literature-reported values, but the average values were below $s_{ur(LL)}$≈1.7, $s_{ur(PL)}$≈170 and R_s≈100, which some researchers considered to be typical of many fine-grained mineral soils.

Given that, the value of the strength ratio (R_s) is not the same for every soil, a new way of predicting values of remolded undrained resistance mobilized for various water content within the plastic range has been presented. The well-established power law relationship between strength and water content resulted in new parameters of relative strength Is_{ur} and relative water content W_{LN}. Inversely related, these indices generate a strong correlation for soils when introduced into the final proposed relationship. On the other hand, existing logw: $logs_{ur}$ correlations postulate a value (usually 100) for the stress ratio, which is usually not the case, especially for organic soils, as shown in the present study and by other researchers.

2.4 Liquidity Index, Sensitivity and Effective Consolidation Stress

Given earlier, the liquidity index is represented:

$$\boldsymbol{LI = \frac{wn - PL}{LL - PL}}$$

which, relative to both the PL and the LL, compares the w_n. LI has shown a good correlation with the soil sensitivity (S_t), which is the proportion of the peak S_u in the soil to its fully remolded (residual) undrained shear strength (S_{ur}).

$$St = \frac{Su}{Sur}$$

High w_n / LL or high LI ratios generally correspond to high S_t values, so these indications show a susceptibility of soil to a loss of strength following a cyclic failure in earthquakes (Boulanger and Idriss, 2004). The use of LI or w_n / LL to evaluate the soil's sensitivity may be complicated in the case of fine-grained, low plasticity soils (e.g., PI<10), as they are sensitive to normal variances in each of the three measurements (PL, LL, w_n). The LI cannot be computed in non-plastic fine-grained soils, and the utility of w_n / LL in practice is not clear, particularly since w_n and LL measurement mistakes are potentially higher for almost non-plastic soils. In short, the comparison of the soil w_n with the Atterberg Limits has been concluded that it does not provide a means of distinguishing between the behavior of sand and clay but can help to evaluate the risk of strength loss if earthquakes (or shearing due to landslides) are strong enough to cause a drop into residual shear strength.

For instance, Fig. 2.9 shows a correlation of the effective vertical consolidation stress, S_t, and LI while Fig. 2.10 shows the corresponding correlation of LI with remolded undrained shear strength.

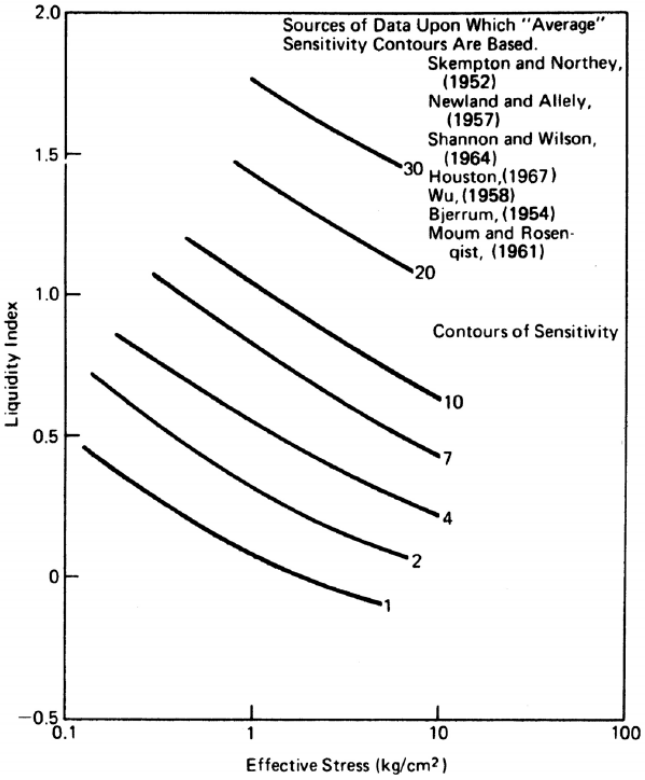

Figure 2.9: Relationship between Effective Consolidation Stress, Sensitivity, and Liquidity Index (Mitchell, 1993)

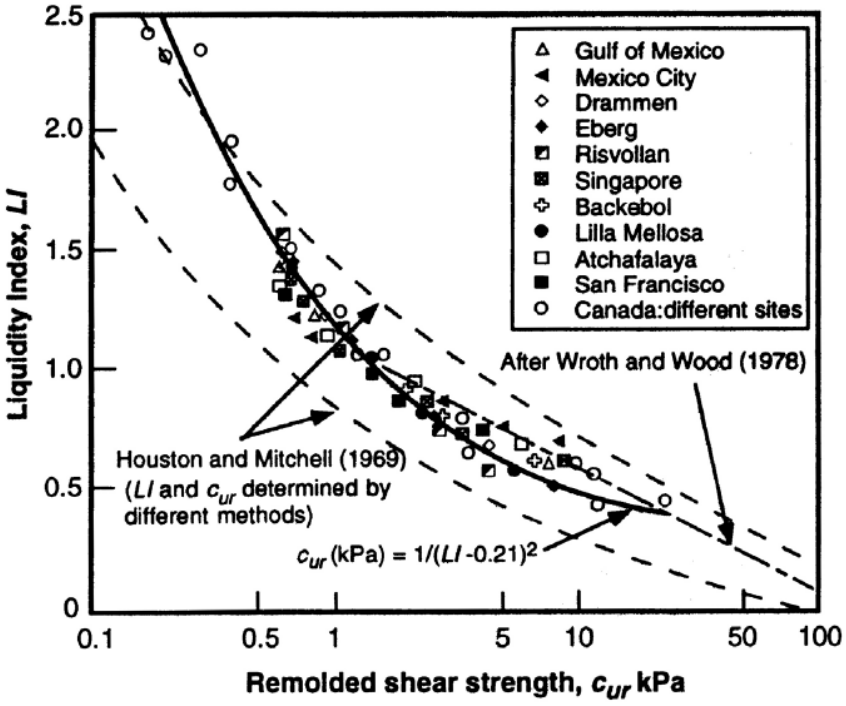

Figure 2.10: Relationship between Liquidity Index and Remolded Undrained Shear Strength (Mitchell, 1993)

2.5 Rainfall-Induced Debris Flows, Field Stress Path and the Stress Transfer due to the Hydrologic Response

Rainfall-induced debris flow is a flow failure in residual and colluvial soils, caused by reducing confining stress during and after intense rainfall periods as a result of a pore-water pressure rise (Anderson and Sitar, 1995). Constant-shear-drained triaxial tests, that simulate the stress path on the field and anisotropically consolidated undrained tests performed at the in-situ stress-level to show undrained loading as a condition of flow failure. Mechanisms of stress transfer are proposed to explain how the initially drained displacement along the stress path may lead to undrained mobilization. In order to determine the potential for failure initiation, a complete stability analysis including an effective stress analysis with constant-shear-drained parameters, and an undrained strength

analysis using undrained residual strength to determine the potential for mobilization of the debris flow are required, because a debris flow involves both drained initiation and undrained mobilization.

Heavy precipitation often leads to shallow slope failures, where the failed material loses strength and flows. These failures are rainfall-induced debris flows and occur across different soil types, including colluvial and residual soils of various gradations (Ellen, 1988). Debris flows tend to occur on geologically young, steep and naturally marginally stable slopes. Then the initial stress state is close to failure stress state and a relatively small disturbance can lead to failure. A completely dry (or hydrostatically submerged) infinite planar slope is considered first, to determine the initial stress state. Although the hydrostatically submerged or dry assumption is not realistic, it allows the gravity-induced shear stress isolation from the seepage-induced stresses. On such a slope, the in-situ stress is gravity-induced and related only to soil density, slope angle, and depth.

For a while, there have been conceptual models for the hydrological response leading to debris flow initiation. Based on the idea that the regolith has increased density and reduced hydraulic conductivity with depth, and if the rate of rainfall exceeds the rate of deep percolation, in the regolith, a perched water table forms in this model. The implicit assumption is that the flow in this saturated area is approximately parallel to the slope in the most critical stability analysis situation. The saturated zone reaches the surface and this height restricts the pore-water pressure. The findings of recent field studies, however, indicate in many instances that this conceptual model is simplified excessively (Johnson and Sitar, 1990). Measurements at different fields show that in general, the unsaturated gradient is downwards in steady precipitation and may rotate downward as the precipitation rate decreases, or even to an upward and out-of-slope orientation as the slope drains (Weyman, 1973; Harr, 1977, Tanaka et al., 1988). In summary, past research shows that

the exact nature of the hydrological response varies significantly and that it is specific to the specific conditions at the site. It is however obvious that heavy rainfall causes an increase of pore water pressure temporally and spatially, which results in a reduction in the effective confining stress and an increase in in-situ principal stress ratio, $K_c = \sigma_1'/\sigma_3'$.

Anderson and Sitar (1995) call the field stress path as the stress resulting from the hydrologic response. Brand (1981) stressed that in a standard triaxial compression test the field stress path is very different from the stress path presented in Fig. 2.11, in terms of $p' = (\sigma_1'+\sigma_3')/2$ and $q = (\sigma_1-\sigma_3)/2$.

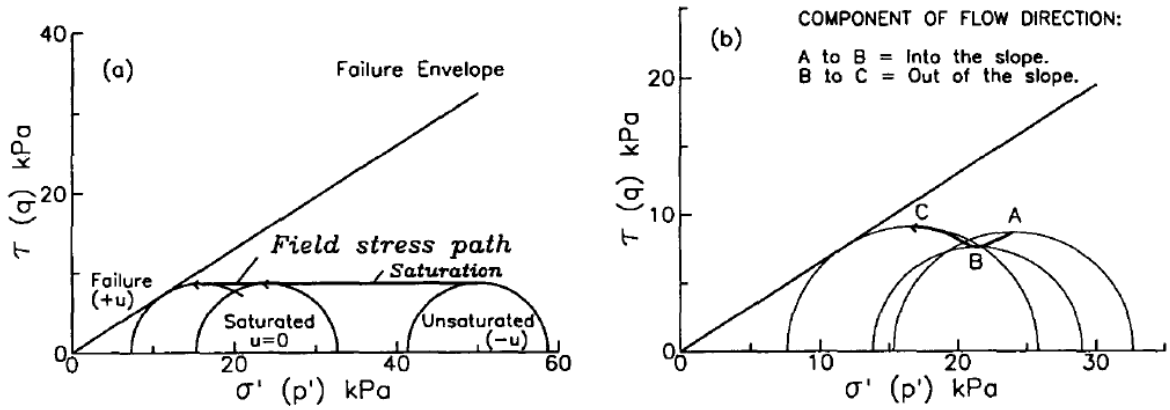

Figure 2.11: Field Stress Path: (a) Assumed; (b) Possible Variation due to Seepage Direction Rotation

The shear stress can actually increase as the soil profile gets saturated, but in most cases, failures occur after some rainfall, at which point weight gain due to the final saturation stage is relatively small (Johnson, 1987). Once the soil has reached saturation, an increase of pore-water pressure does not change the magnitude of shear stress, but a change in the direction of the seepage or the hydraulic gradient can affect the shear stress. The stress path in the field increases K_c and starts with a shear strain at a certain critical

value when $K_c = K_f$. This point of yield is the initiation of a failure and a stress change caused by the hydrologic response to rainfall is achieved.

A conventional account of conditions that lead to failure would suggest that the travel rate along the field stress path is first only driven by the hydrologic response, but that when the soil starts to shear, the travel rate increases because loosely packed soil particles tend to collapse into the saturated void space. In effect, undrained deformation is triggered by the path of field stress, followed by liquefaction and flow failure when this occurs within a region of potential instability (Lade, 1992; 1993). Laboratory study has also shown that this can happen suddenly and even in drained tests, causes undrained failure. In drained triaxial tests where the stress rate was limited, Riemer (1992) measured the sudden collapse of the loose sand by generating the field stress path. Also, when there was no strain control, similar tests show the collapse is rapid and undrained (Sasitharan et al. 1993). Eckersley (1990) has also shown, by gradually increasing the water levels in an instrumented slope of a laboratory model, that the drained failure can result in undrained mobilization of flow failure.

A mechanism for undrained loading is necessary to reconcile the observations that the CSD (or field stress path) leads to dilation while shearing, whereas the ACU path leads to contractive strain-softening, and failures at the site mobilize into the debris flow. There are two mechanisms to demonstrate that stress transfer sufficient to cause undrained failure mobilization may result from deformation initiation once soil failures occur along the stress path of the field. The first mechanism is the stress concentration that develops near the base of the tension cracks that occur as a result of failure initiation. If the transfer of stress is sufficiently rapid to prevent drainage, mobilization of undrained failure could result from stress transfer/concentration at the base of increasing tension cracks. A progressive failure mechanism in which the shear stresses are transferred from a region of a slope that has

failed along the field stress path to a region that has not, is the second mechanism for stress transfer. Because of the highly variable nature of the hydrologic response causing the factor of safety (FS) to be dependent on the location along the slope profile, this is a probable scenario (Johnson and Sitar, 1989). It is also possible that the reaction causes the field stress path to continue in one location beyond the failure initiation point, while the adjacent slope parts still have FS > 1. Fig. 2.12 represents the stress path for a soil element subjected to an increase in the pore water pressure, causing p' to move below its value at failure.

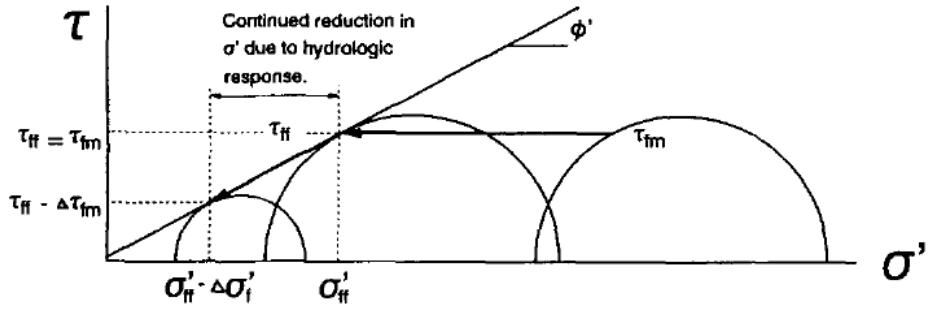

Figure 2.12: Stress Transfer Schematic due to Hydrologic Response

2.6 Steady-State Lines for Various Fines Contents and Intrinsic Compression Line Definition

The following equation replaces the relationship usually recommended for the description of the test results of oedometer for normally consolidated soils (Gibson et al., 1981),

$$e = e0 - Cclog10\left(\frac{\sigma'}{\sigma o'}\right)$$

where e_0 is a reference void ratio, σ_0' is the corresponding effective stress, and C_c is the compression index. Given below are the figures from different sources to represent steady-state lines for sands with various fines content ranges. The SSL (steady-state line)

establishes the relationship between the mean effective stress p' (=(σ_1'+2σ_3')/3) and the ultimate void ratio in a triaxial test.

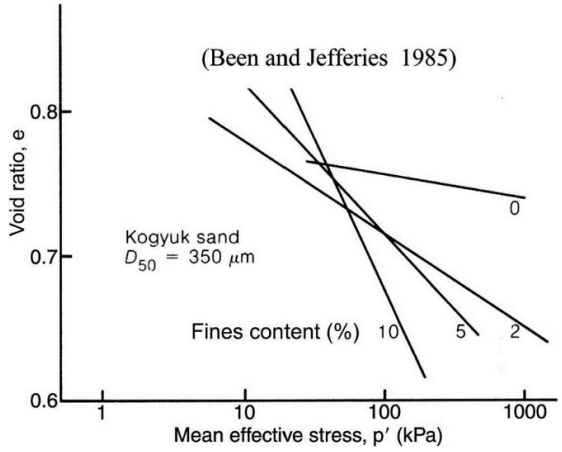

Figure 2.13: Steady-State Lines for Sands with Fines Contents Ranging Between 0% and 10% [Note: D_{50} is the mean grain size for the coarser grains (from Been and Jefferies, 1985]

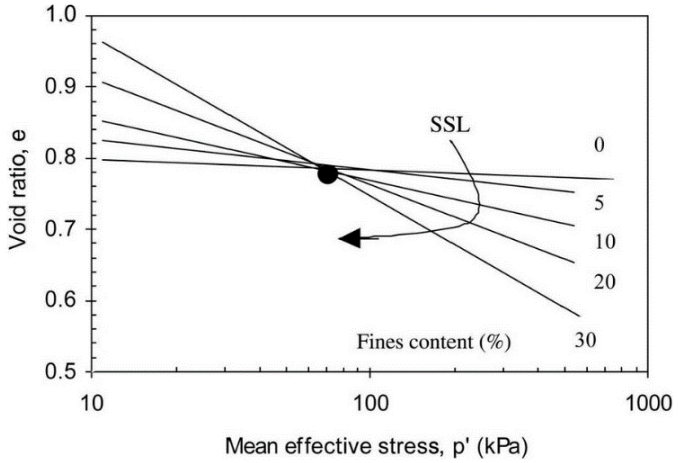

Figure 2.14: Effect of Fines Content and the Effective Stress Level Idealized on the Steady-State Lines in the e-lnp' Space (from Bouckovalas et al. 2003)

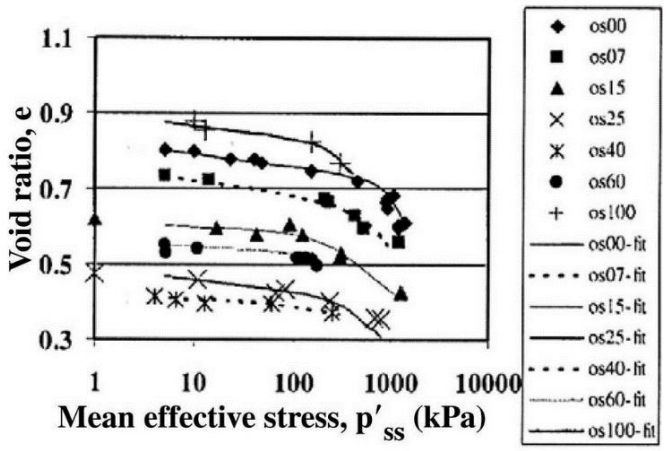

Figure 2.15: Steady-State Lines for Sand with Fines Contents Ranging Between 0% and 100% (from Thevanayagam et al., 2002)

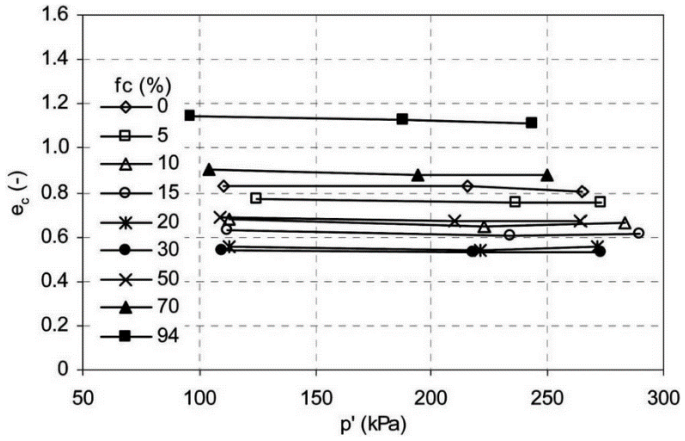

Figure 2.16: Steady-State Lines for Samples with Various Fines Content (fc), Under Drained Conditions and Based on the After-Consolidation Void Ratio (e_c) (from Yang et al. 2006)

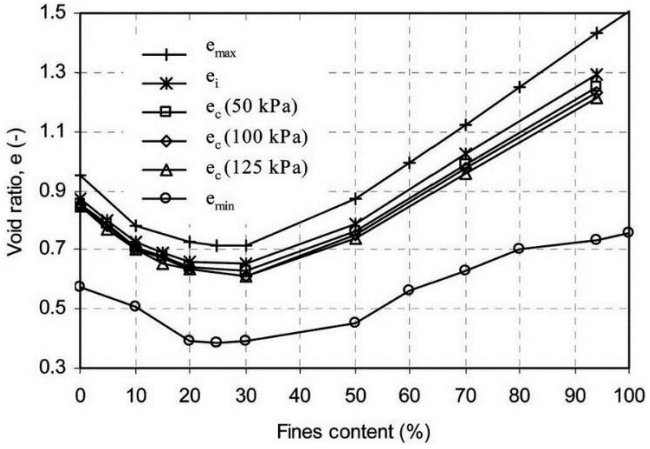

Figure 2.17: Void Ratios for Different Fines Content [Note: e_{max}, maximum void ratio; e_i, initial void ratio; e_c (50 kPa), void ratio after consolidation for 50 kPa confining pressure; e_c (100 kPa) void ratio after consolidation for 100 kPa confining pressure; e_c (125 kPa) void ratio after consolidation for 125 kPa confining pressure; and e_{min}, minimum void ratio (Yang et al., 2006)]

Some authors discussed the problems in accurately defining the soil's steady-state condition, both in situ and in laboratory test specimens because of uncertainties in the determination of void ratios (Poulos et al. 1985; Castro et al. 1985; Sladen and Handford 1987; Kramer 1989; Vaid and Sivathayalan 1996; Garga and Zhang 1997). An error in the void ratio resulting from the measurement of specimen properties may result from errors in specimen height, diameter, mass and specific gravity measurement.

In the context proposed by Burland (1990), which relies on the normalization of compression curves using the void index, I_v, comparisons between reconstituted and treated soils may be established. The definition of I_v is based on the following: e_{100}* and e_{1000}*, the intrinsic void ratios, that is, the soil void ratios in the reconstituted state at stresses of 100 kPa and 1000 kPa, respectively:

$$Iv = \frac{e - e100^*}{e100^* - e1000^*}$$

With such a normalization the compression curves of reconstituted-remolded soils fall around a unique line called the ICL (intrinsic compression line), and in-situ condition in the normally consolidated state plots in a band on the right of the ICL for a variety of sedimentary natural clays (Bobet et al., 2011). Hong et al. (2010) performed oedometer tests on three reconstituted clays with different liquid limits, beginning with a very small effective vertical stress of 0.5 kPa. Ranging from 0.7 to 2.0 times their corresponding liquid limits, the soils were prepared at different initial water contents. They observed that the e-logσ'_v compression curves have an inverse 'S' shape as a result of deformation-resistant suction pressure similar to that of soft natural clays caused by consolidation yield stress. As reported by Burland (1990), for stresses greater than 10 kPa, and at an initial water content of 1.0-1.5 times the liquid limit, the e-logσ'_v compression curves of reconstituted clays are in a shape slightly concave upwards. Hong et al. (2010) also reports that the previously discussed I_v can also be expressed as follows:

$$Iv = 2.45 - 1.285log\sigma'v + 0.015(log\sigma'v)^3$$

where σ'_v is expressed in kPa. Burland (1990) recommended that ICL only be used for effective vertical stress between 10 kPa and 4000 kPa. Obtained by Cerato and Lutenegger (2004), the results of oedometer tests performed on four clays at initial contents of $1w_L$, $1.25w_L$, $1.5w_L$ and $1.75w_L$ illustrates that the values of e_{100}* and e_{1000}* may significantly be affected by the initial water contents.

2.7 Debris Flow Physics and Deposition

According to Iverson (1997), debris flows occur when masses of poorly sorted, agitated and water-saturated sediments have risen on its own slopes in response to gravitation. Solid and fluid forces influence the movement, distinguishing debris flows

from related phenomena such as rock avalanches and sediment-laden water flows. Whilst solid grain forces dominate avalanche physics and fluid forces prevail over flood physics, solid and fluid forces must work together to produce debris flows.

Other criteria for defining debris flows stress the concentration of sediment, distribution of grain sizes, flow velocities, shear strengths and shear rates (Beverage and Culbertson, 1964; Varnes, 1978; Pierson and Costa, 1987), but interacting solid and fluid forces is a wider, more mechanistic distinction. Many events have been identified with this rationale as debris torrents, debris slides, debris floods, mudslides, mudspates, mudflows, hyper-concentrated flows, and lahars perhaps seen as debris flows (Johnson, 1984). The interaction of solid and fluid forces not only physically differentiates the debris, but also gives them unique destructive power.

Major and Iverson (1999) claims, measuring the pore-fluid pressure and the total bed-normal stress of several experimental debris flows of ~10 m^3 provides new insight into the debris-flow deposition process. During flow movements and accelerations, pore-fluid pressures almost sufficient to cause liquefaction were developed and maintained, persisted in the debris flow interior during flow deceleration and deposition, and were significantly dissipated during post-deposition consolidation. In contrast, there was little or no positive pore fluid pressure on the leading edges of the debris flows. Therefore, deposition resulted from concentrated grain contact friction and bed friction on flow margins. This finding is in conflict with models which generally invoke excess pore-fluid pressure, uniform viscoplastic yield strength or pervasive grain-collision stresses to explain deposition of debris flows. In addition, the findings show that deposit thickness is not used to deduce the flowing debris strength.

Iverson (2003) presents that models that employ a fixed rheology cannot provide accurate interpretations or predictions of the movement of debris flows because the

evolving behavior of debris flows is too complex for any rheological equation that uniquely relates stress and strain. The field observation and experimental data indicate that the behavior of debris may vary, due to temporal and space variations in pore fluid pressure and mixture agitation, from nearly rigid to highly fluid. In addition, behavior can change if the composition of debris changes as a result of the segregation in grain size and the gain or loss of solids and fluids in transit. A Coulomb Mixture theory model, which may represent variable interactions between solid and fluid constituents in heterogenous surges of high-friction debris- flow, coarse-grained heads and lower friction, liquefied tails, provides an alternative to fixed-rheology models.

They generally hypothesize that water pressures become very large, which is why debris flows can include rocks and blocks of overconsolidated clay.

2.8 Summary

The scope and purpose of this thesis were provided in this chapter. The empirical mobility predictions for debris flows and Oso landslide were discussed. Liquefaction and cyclic mobility, liquidity index, sensitivity and effective consolidation stress, rainfall-induced debris flows, field stress path and the stress transfer, one-dimensional consolidation and void ratio, and the steady-state lines for soils with various fines content and the description of the intrinsic compression line and other hypotheses that might have led to the 2014 debris flow were also presented. The relations between Atterberg limits and the liquidity index and the remolded shear strength and water content have been examined subsequently. A further description was also provided for the debris flows and the deposition. The literature review seeks to discuss the information published, in particular within the topic of the thesis.

CHAPTER 3: BACKGROUND ON OSO LANDSLIDE

3.1 Introduction

In this chapter, first, general information on Oso landslide is presented, followed by the synthesized available literature on the mechanisms of the 2014 debris flow including hydrology, stability, subsurface conditions, material properties, and the history of the landslide. Secondly, geotechnical soil characterization of Qglv deposits are summarized, after which the geotechnical, geomorphic, and hydrogeologic properties are discussed, determined by performing several tests.

3.2 2014 Oso, Washington Landslide

On March 22, 2014, a massive and fast-moving landslide destroyed the Steelhead Haven Community near Oso, Washington, across the North Fork of the Stillaguamish River in Snohomish County. Another referral for the landslide is the SR530 Landslide because the flowslide debris buried Washington State Route 530 (SR530) that connects Oso and Darrington, Washington, and some Oso residents prefer not to name the landslide after their community. The landslide is considered the deadliest in the history of the continental United States with 43 fatalities (Wartman et al. 2016). The entire landslide involved approximately 8.3 million-m^3 of glacial deposits and water-filled colluvium from prior landslides present along the slope toe. On the south side of SR530, the colluvium-derived flowslide traveled more than 1.5 km to its distal edge. Stark et al., 2017, examined landslide features and exposed geology, obtained soil samples for laboratory testing to estimate engineering properties during various site visits (May 22–24, 2014, February 28, 2015, and April 16, 2015). They also reviewed aerial photographs and conducted stability analyses to assess the impact of changes in slope geometry with time. Compared to the three previous landslides, the 2014 event was about three times higher, involved about ten

times the volume of material and had a run-out of landslide debris about seven times further from the toe of the slope (Gilbert et al. 2016).

3.2.1 GEOLOGY AND REGIONAL PHYSIOGRAPHY

The landslide occurred in glacial sediments (Fig. 3.1) on the north side of the North Fork of the Stillaguamish River valley (Fig. 1.1). These sediments were deposited during the most recent glacial period ending about 15,000 years before present. The 2014 event was preceded by three documented failures of the lower part of the slope occurring in 1949, 1967 and 2006 (Fig. 3.2) (Gilbert et al. 2016).

The crest of the Oso landslide slope is located at an elevation of approximately 270 m (880 ft), of the west-trending valley of the Stillaguamish River on the north side, which is at an altitude of approximately 75 m (246 ft). This corresponds to a slope height of approximately 200 m (650 ft). Stillaguamish River Valley floor width at this location varies from 2.0 km to more than 6.0 km. The slope is part of a massive glacial terrace deposit which developed after the last advance of continental glacial ice sheets into the Puget Sound. The 2014 landslide occurred at a relatively narrow reach of the river, where it flows north and then west along the slope toe. The river erosion, particularly in the eastern end, has caused some landslides in the lower portion of the slope including landslides in 1937, 1951, 1952, 1967, 1988, and 2006, (see 2006 landslide in Fig. 3.3). The 2014 landslide did not involve bedrock, but the bedrock in the immediate landslide area consists of Jurassic metasedimentary, metavolcanic, and ultramafic rocks in the western portion of the valley and Tertiary sedimentary and volcanic rocks in the eastern portion (Dragovich et al. 2003; Keaton et al. 2014). Quaternary-age surficial deposits overlie the bedrock and include a series of deep glacial soil deposits, which are discussed subsequently (Stark et al. 2017).

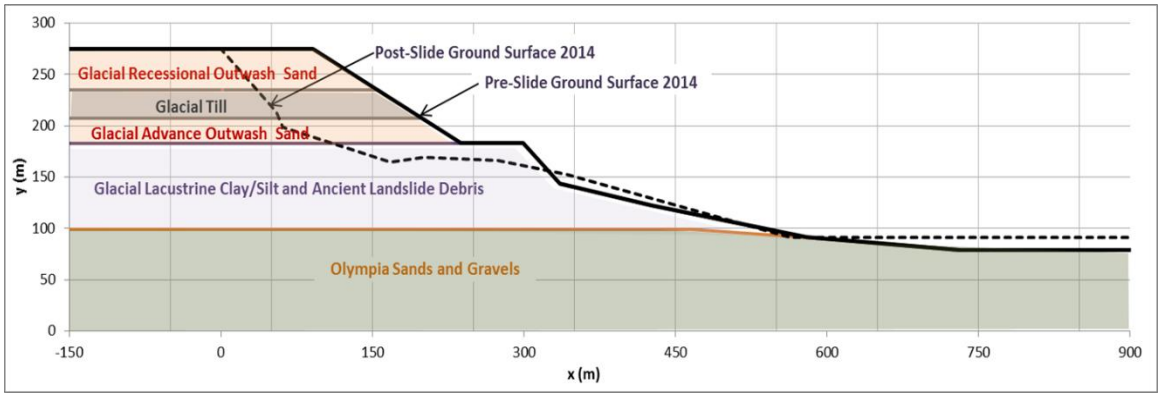

Figure 3.1: Cross-Section from North to South of 2014 Landslide (from Gilbert et al. 2016)

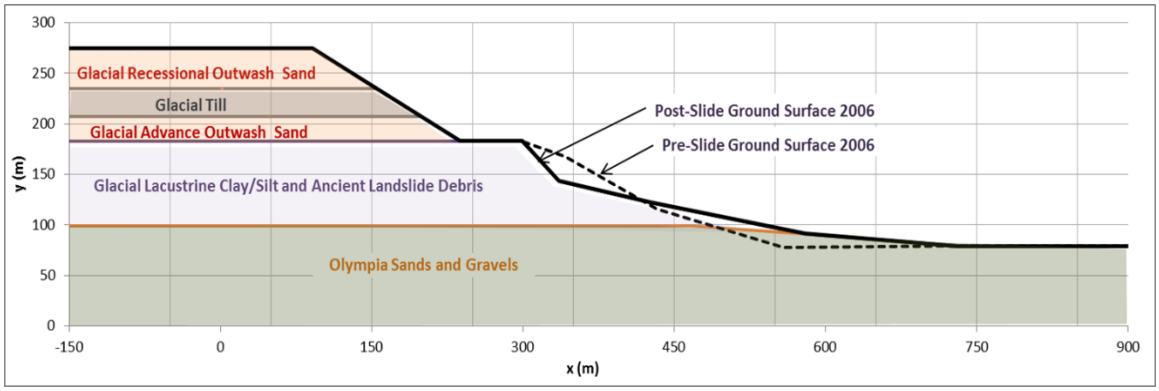

Figure 3.2: Cross-Section from North to South of 2006 Landslide (from Gilbert et al. 2016)

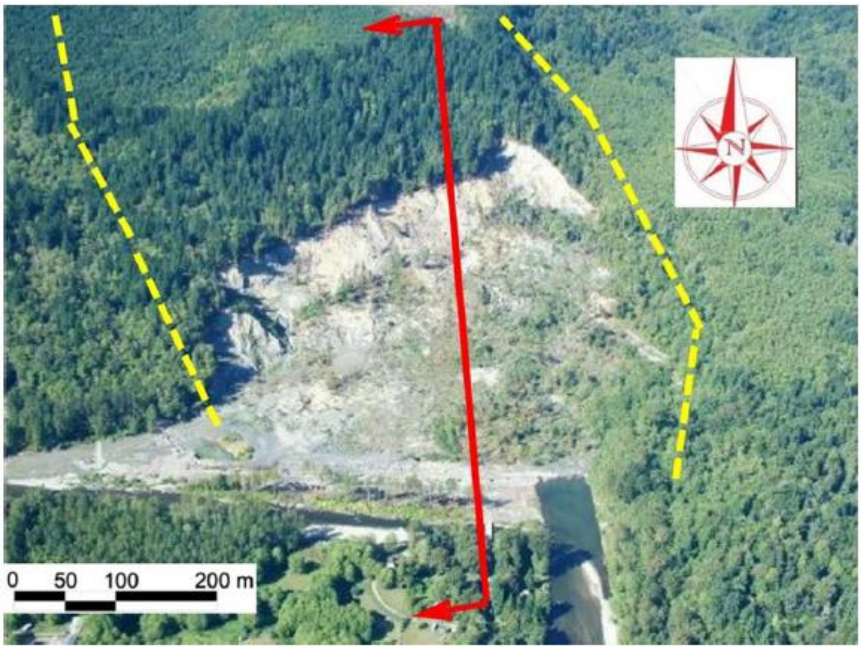

Figure 3.3 Aerial View of 2006 Landslide, Location of The Cross-Section in Fig. 3.4 (solid line), and Outline of Sides of 2014 Landslide (dashed lines) (image courtesy of Rupert G. Tart) (from Stark et al. 2017)

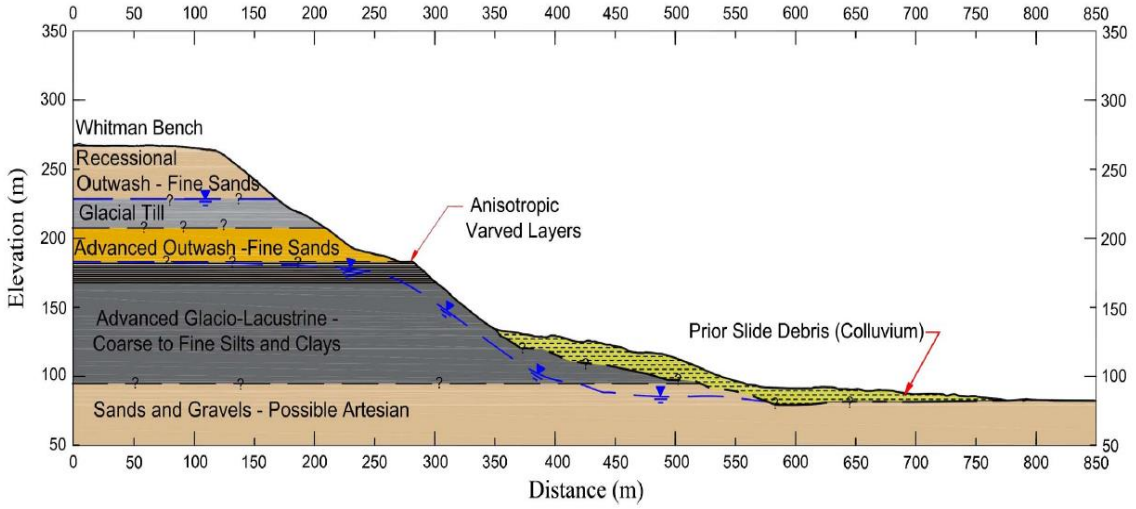

Figure 3.4: Slope Cross-Section at the Location in Fig. 1.1 prior to 2014 Landslide with Phreatic Surfaces Inferred from Inverse Stability Analyses except where Observed in Borings from the Whitman Bench (from Stark et al., 2017)

3.2.2 HYDROLOGY

The weather was clear and dry when the 2014 landslide occurred. There was about 20 mm of precipitation three days before the landslide. In the year before the landslide, the only remarkable aspect of the hydrology was the cumulative precipitation for the period 21 days before the event; this 21-day cumulative precipitation has a return period of about 100 years based on historical records (Henn et al. 2015).

3.2.3 STABILITY

The documented landslides before the 2014 event were all within the glaciolacustrine clay (Fig. 3.2). A stability analysis of the 2006 event indicates one plausible hypothesis for this failure: the drained shear strength of the glaciolacustrine clay was mobilized (i.e., negative pore water pressures induced by previous shearing events eventually dissipated). Mobilization occurred with a fully softened shear strength in the "intact" material and a shear strength between the fully softened and residual shear strengths in a zone of the previous shearing from ancient 2014-like events that created the existing slope (ancient head scarp) above the glaciolacustrine clay (Fig. 3.3). A mobilized shear strength in the zone of ancient shearing that is 80-percent of the way between the residual and fully softened shear strengths gives a factor of safety of close to one for the 2006 slope (Fig. 3.5) (Gilbert et al., 2016).

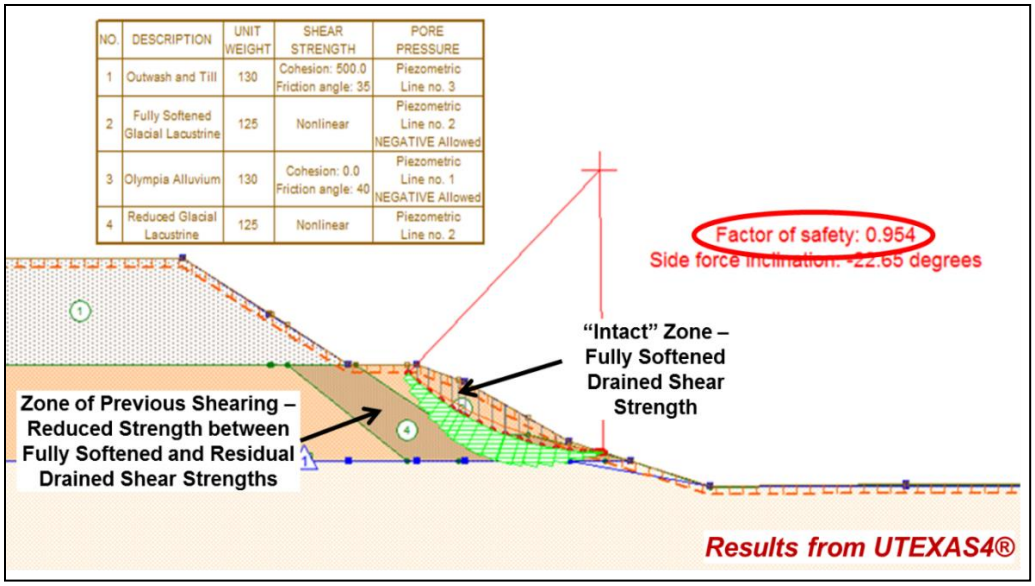

Figure 3.5: Stability Analysis for 2006 Landslide (from Gilbert et al. 2016)

Following the same approach that gives a factor of safety of one for the 2006 event, the factor of safety with the topography at the time of the 2014 event (i.e., the post-2006 landslide topography) is also about one (Fig. 3.6). If the geometry of the head scarp in the lower slope was similar to what was produced by the 2006 event, then the factor of safety for the slope above the glaciolacustrine clay is well below one after a failure of the lower slope (Fig. 3.7). Therefore, a plausible hypothesis for the massive 2014 landslide is that it was triggered by a smaller landslide similar to the 2006 event at the toe of the slope, which destabilized a more substantial extensional failure that extended up nearly 200 m to the top of the valley side.

The run-out of landslide debris from the 2014 landslide was the cause of the catastrophe for the community. The run-outs from both the 1967 and 2006 landslides at this location did not directly impact homes and people in the Steelhead Drive Community (note that the community was not there prior to 1960). However, the community was destroyed by the 2014 landslide because the debris ran out across the valley (Fig. 1.2).

Field exploration after the failure indicated there were two stages of failure: the first stage involved a larger debris avalanche/flow responsible for the destruction of the Steelhead Drive Community. The latter smaller stage was an extensional failure that came down and ran onto the back side of the first stage (Wartman et al. 2016). Based on empirical correlations with the volume of debris, the run-out from the 2014 landslide is consistent with other landslides in similar geologic settings (Fig. 3.8) (Gilbert et al. 2016).

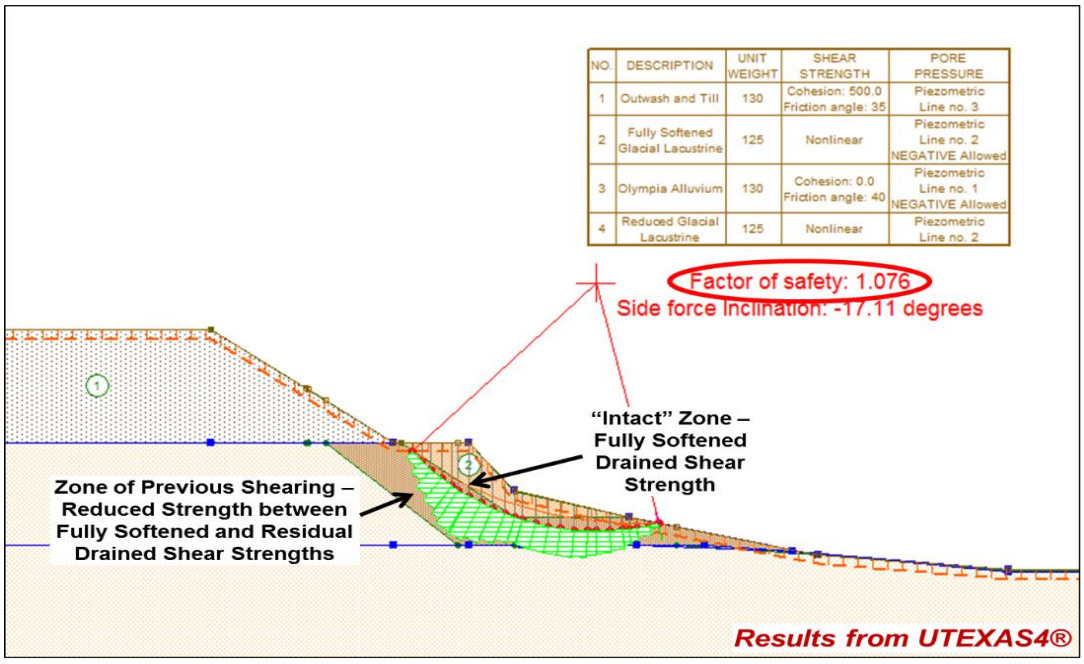

Figure 3.6: Stability Analysis for 2014 Landslide – Initial Condition (from Gilbert et al. 2016)

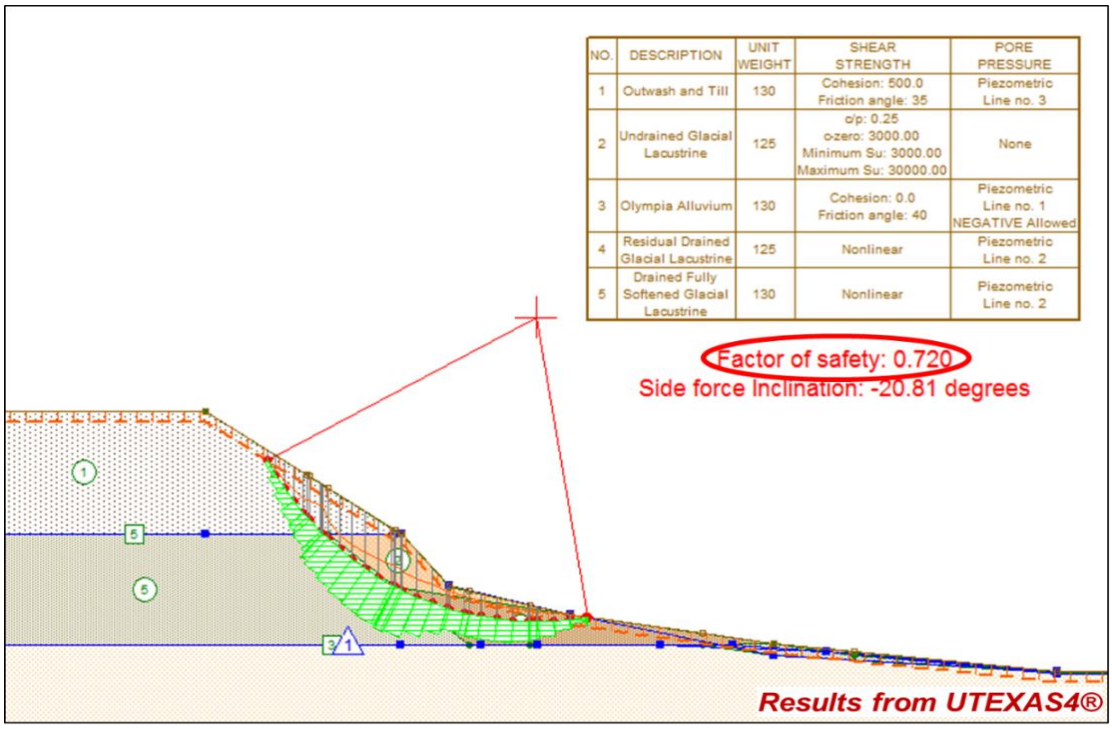

Figure 3.7: Stability Analysis for 2014 Landslide – Post-Failure of Lower Slope (from Gilbert et al. 2016)

3.2.4 SUBSURFACE CONDITIONS

Knowledge of the pre-2014 landslide subsurface conditions is critical for understanding the failure mechanism because a comparison of the final and initial locations of the various glacial soil deposits helps to understand the landslide initiation, movement, and run-out. Based on the exposed landslide head scarp, hand and shovel excavations during various site visits, geologic maps, borings before (Shannon 1952) and after the landslide (Badger 2015), and soil samples collected and tested here, the subsurface profile prior to the 2014 landslide is shown in Fig. 3.4 and located at the cross section location in Fig. 3.3 (Stark et al. 2017).

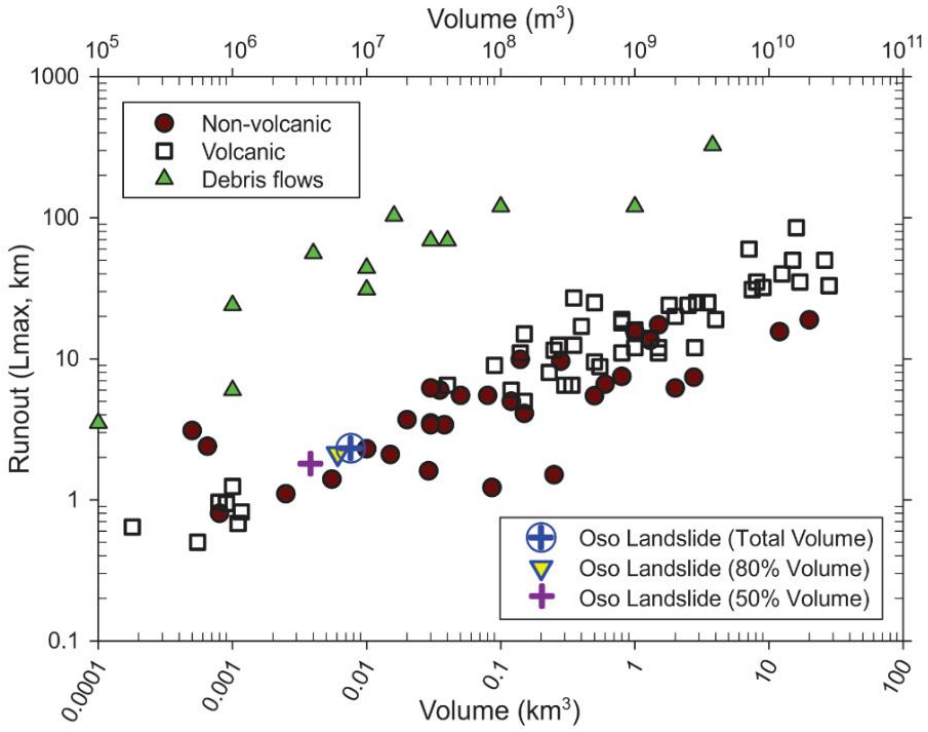

Figure 3.8: Comparison of Run-Out from 2014 Oso Landslide with Other Landslides (from Gilbert et al. 2016)

This subsurface profile consists of (from top to bottom):

2 Recessional outwash: Tan to light brown unsaturated cohesionless fluvial deposits, medium-dense to dense fine to coarse sands with cross beddings. The thickness of this outwash is approximately 40 m (130 ft) from elevation 270 to 230 m (886 to 755 ft). The top of this deposit is referred to locally as the Whitman Bench or Upper Plateau (Fig. 3.4).

3 Glacial till: Light gray unsaturated stiff to very stiff, consolidated, and unsorted mixtures of sand, silt, clay, and gravels with scattered boulders and cobbles. From the elevation, 230 to 207 m (755 to 680 ft), the thickness of this layer is approximately 21 m (70 ft).

4 Advanced outwash: Tan to light brown unsaturated fluvial medium-dense coarse sand and sandy gravel with localized clay and silt interbeds. The advanced outwash thickness is approximately 30 m (100 ft) from elevation 207 to 177 m (680 to 580 ft).

5 **Advanced glaciolacustrine:** Light to dark gray, medium stiff to stiff, unsaturated to saturated with horizontally laminated low to high-plasticity clays and silts with occasional fine sands laminae. From the elevation, 177 to 95 m (580 to 310 ft), the lower thickness of this layer is approximately 82 m (270 ft), and it was also involved in most, if not all, of the earlier landslides caused by river erosion of the deposit along the slope toe. The unsaturated condition of the Advanced Glacio-Lacustrine deposit is evident in surficial exposures and available borings. Higher degrees of saturation may exist further behind the eroded valley scarp.

6 Sands and gravels: Well-sorted fine- to medium-grained sands and gravel with possible artesian pressures.

Fluvial deposits and alluvium: Oxidized deposits of loose saturated sands and silts forming the river floodplain, mixed with debris from prior landslides exposed near the base of the slope; it is the youngest deposit which is not part of the stratigraphic sequence (Stark et al. 2017).

3.2.5 LANDSLIDE HISTORY

The 2014 landslide occurred in a slope with a history of prior landslides. Modern accounts of landslides in the lower portion of the slope date back to 1932 (Thorsen 1969). More recent high-resolution topographic relief images generated by light detection and ranging (LiDAR) show many significant ancient landslides including one at the location of the 2014 landslide have occurred in this valley. The documented history of landsliding at this site reveals two types of event: (1) massive prehistoric landslides that involve the upper

glacial terrace deposits, i.e., the Whitman Bench (Figs. 3.4 and 3.9), that are similar to the 2014 landslide, and (2) smaller landslides in the lower portion of the slope primarily caused by river erosion.

The occurrence of a large prehistoric landslide at the location of the 2014 landslide is essential because it created the Ancient Landslide Bench shown in Fig. 3.9, which supported and protected the Whitman Bench from landslides in the lower portion of the slope primarily caused by river toe erosion and precipitation. Based on the geometry of neighboring high-elevation landslides also shown in Fig. 3.9, it is anticipated that the prehistoric landslide at this location occurred through the weak varved lacustrine layers in the upper portion of the advanced glaciolacustrine deposit and evacuated some of the overlying Whitman Bench (Stark et al. 2017).

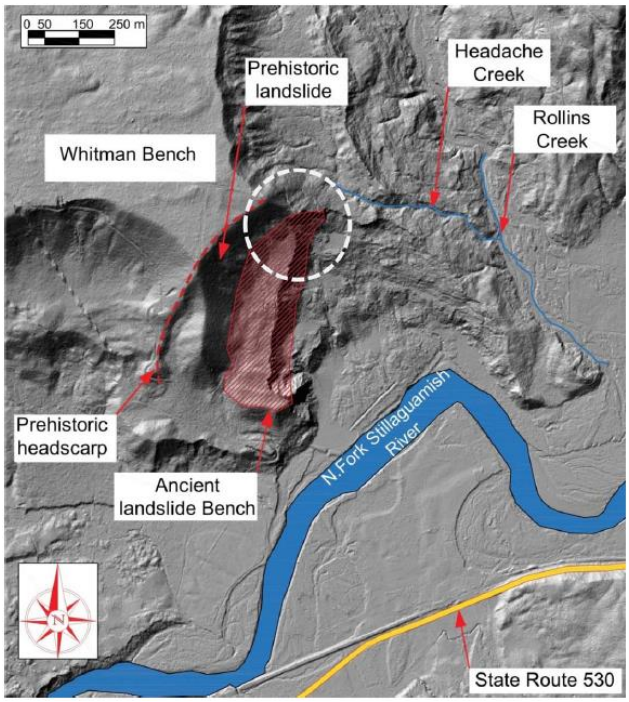

Figure 3.9: 2013 LiDAR-Derived Topography Showing the Oso, Washington, Landslide in context with the Ancient Landslide Bench (base courtesy of Puget Sound Lidar Consortium) (Stark et al. 2017)

After this landslide, a bench or ledge was created that supported the overlying Whitman Bench slope and protected the Whitman Bench from over-steepening by landslides in the lower portion of the slope primarily caused by river toe erosion until after 2006. The ancient slide mass traveled down the slope and across the Stillaguamish River, where it was eroded over geologic time. This is easy to visualize because the ancient slide mass consisted primarily of two unsaturated sandy outwash deposits that are quickly eroded by the river as witnessed after the 2014 landslide. During a site visit only two months after the 2014 landslide, a significant amount of the aforementioned sandy outwash deposits had already been eroded by the Stillaguamish River (Stark et al., 2017).

This explains the lack of a significant portion of the ancient slide mass being present on the valley floor before the 2006 and 2014 landslides. Aerial photographs of 1937, 1951, 1952, 1967, 1988, and 2006 landslides assembled by the Seattle Times (2016), Kim et al. (2015), and Sun et al. (2015) show only the lower portion of the slope was involved and these landslides involved only the advanced glaciolacustrine clay deposit. There was still sufficient width of the bench to support the overlying Whitman Bench until after the 2006 landslide, although the landslides in the lower portion of the slope removed some of the Ancient Landslide Bench. Based on the dates of prior landslides and aerial photographs, it took approximately 35–40 years to erode enough landslide debris and colluvium to initiate another landslide in the lower portion of the slope. Nevertheless, in each of these low-elevation landslides, the active river channel would be moved by the slide mass to the south, away from the slope toe. The river would then start eroding the prior landslide debris to the north until it was again undermining the advanced glaciolacustrine clays (Stark et al. 2017).

The 2014 landslide is significantly different from 1937, 1951, 1952, 1967, 1988, and 2006 landslides in the following four main aspects:

1. River erosion did not play a serious role because the river channel had been pushed significantly south of the slope by the 2006 landslide;
2. The 2014 landslide occurred only eight years after the 2006 landslide, not 35–40 years;
3. In comparison to mobilities such as 85 m (280 ft), 200 m (656 ft), and 250 m (820 ft) in the 1947, 1967, and 2006 landslides, respectively (Iverson et al. 2016), slide mobility was much more significant, resulting in the slide mass traveling more than 1.5 km; and
4. The 2014 slide mass is much larger than the previous 1937, 1951, 1952, 1967, 1988, and 2006 slide masses.

As a result, a different failure mechanism than river toe erosion had to initiate the 2014 landslide. The first factor considered for the 2014 landslide is precipitation. The 2014 landslide occurred during a dry, sunny morning after a period of unusually intense rainfall. 86 years of data from the nearby precipitation gauges indicate the rainfall during the month prior to the landslide was significantly higher than average (Keaton et al. 2014). In particular, these data show the 45-day period before the landslide was wetter than 98% of the same 45-day period in the 86-year historical record (Iverson et al. 2016). Cao et al. (2014) and Henn et al. (2015) show the cumulative precipitation for the 21 days before the March 22, 2014, landslide corresponds to a return period of approximately 97 years, making the 21 days prior to the landslide the wettest [403 mm (15.8 in.)] on record at the Darrington, Washington, rain gauge. It is anticipated this intense rainfall, higher groundwater, and increased runoff along the eastern side of the 2014 landslide mass triggered a landslide that removed the small remaining portion of the Ancient Landslide Bench on the eastern end (see the dashed circle in Fig. 3.10), and undermined the Whitman

Bench slope as discussed later. This resulted in the initiation of the two-phase failure mechanism described subsequently.

In summary, the rainfall during the fall 2013 and winter 2014 was below average to average, but the rainfall from March 1 to 22, 2014, corresponds to a 97-year return period and is the wettest period in the 86 years of historical data. Even with a record rainfall in March 2014, the Oso landslide is the only massive landslide in the valley and region, therefore, as an oversteepened and/or undermined Ancient Landslide Bench on the eastern end, this site had a unique feature. LiDAR images show no other ancient landslide bench in this area was oversteepened and/or undermined to the extent of the bench shown in Fig. 3.10.

Hypothesized phases of the landslide are as follows:

- Phase I of Failure Mechanism: Initial Slide Mass
- Colluvial Flowslide of Phase I (Fig. 3.11)
- Phase II of Failure Mechanism: Whitman Bench Slide Mass
- Liquefaction of Colluvium and Precedent

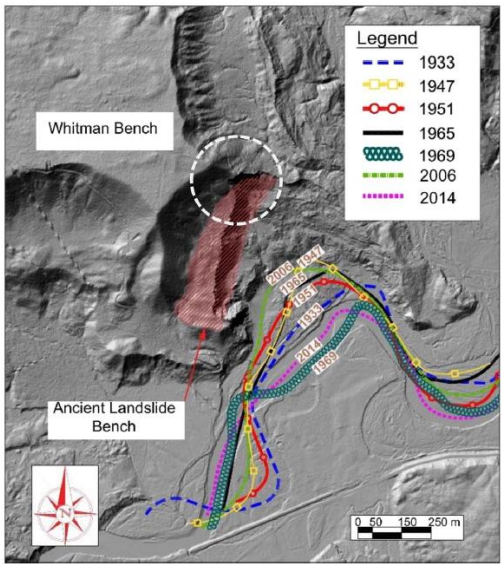

Figure 3.10: Changes in Stillaguamish River Channel between 1933 and 2014 due to Previous Landslides in the Lower Part of the Slope shown on 2013 LiDAR-Derived Topography (base courtesy of Puget Sound Lidar Consortium) (Stark et al. 2017)

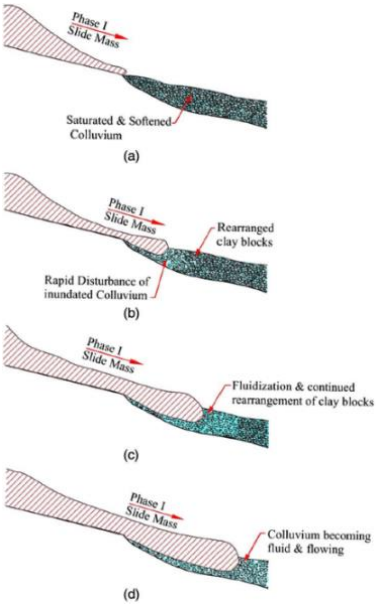

Figure 3.11: Phase I Slide Mass Rapidly Moving Downslope and Initiating the Colluvial Flow Slide: (a) Rapid Upslope Slide; (b) Pushing of Colluvium, Initiation of Undrained Strength Loss; (c) Colluvial Flow Slide Initiation; (d) Colluvial Flow Slide Enlargement (Stark et al. 2017)

3.2.6 SUMMARY

The significant findings of the investigation, testing, analysis, and slope history used to determine the two-phase failure mechanism of the March 22, 2014, landslide near Oso, Washington, that destroyed more than 40 homes and fatally injured 43 people, are:

- The 2014 landslide occurred in two phases. Phase I consists of an initial landslide involving the upper plateau, i.e., Whitman Bench, that was oversteepened by the 2006 landslide. Phase II is a retrogressive landslide in the upper terrace caused by the evacuation of the Phase I slide mass, which left the upper plateau unsupported.
- Rainfall in the 21 days before the 2014 landslide is the highest on record and corresponds to a 97-year return period, which, on the eastern end of the ancient landslide bench, contributed to the initiation of the Phase I landslide.
- The Phase I landslide impacted, pushed and overrode the water-filled, disturbed, and softened colluvium along the slope toe, causing a dramatic undrained strength loss (liquefaction) that enabled the colluvium to flow approximately 1.5 km across the valley.
- Phase II did not exhibit a substantial run-out because the materials are dense, unsaturated, frictional, and were stopped by the back of the Phase I slide mass.

  The size and run-out of the 2014 landslide are not unprecedented for similar ratios of slope height to run-out distance in this valley and other locations (Hunter and Fell 2003a).

3.3 Information from the Literature about the Colluvium and the Run-out

Riemer et al. (2015) proposed a report to comprehend the hazards posed by highly mobile Pacific Northwest, USA landslides, Geological Survey (USGS), together with its

project partners, the Washington State Department of Transportation (WSDOT), and the University of California, Berkeley Dept. of Civil and Environmental Engineering (UCB), has undertaken a study to identify the geotechnical, hydrogeologic, and geologic conditions in which these large landslides initiate, as well as the responsible processes of this, and possibly other landslides for their exceptional mobility in the region.

The report describes the methods of obtaining and testing the intact stratigraphy of the soil behind the headscarp of the 22 March landslide. For 25 soil samples representing a stratigraphy at 20 different depths along a 650 ft (198 m) soil profile, detailed geotechnical index test results are presented. This includes (1) soil in situ water content and unit weight (when applicable); (2) specific gravity of soil solids; (3) the distribution of grain-size in each sample; (4) critical limits for the contents of fine-grain water (i.e., Atterberg limits) ; and (5) official Unified Soil Classification System (USCS) designation. Moreover, preliminary stratigraphy and geotechnical relationships are presented within and between soil units.

In the fall of 2014, WSDOT performed geotechnical drilling at three locations close to the landslide. In order to sample major stratigraphic units present in the landslide deposit, two borings (H-1-14 and H-2-14), located ca. 300 ft and 360 ft (91 and 110 m) behind the 2014 headscarp (Fig. 3.12), had been drilled to 650 ft and 635 ft (198 m and 194 m) depths, respectively (Fig. 3.13). A third boring of 300-ft (91 m) was drilled on the other side of the valley from the 2014 landslide through a prehistoric landslide, to investigate stratigraphic relations through the valley, to determine the existing depth of the shear plane of the prehistoric landslide, and to characterize the groundwater conditions inside and beneath the landslide mass. The report contains only samples of the two boreholes closest to the landslide (H-1-14 and H-2-14).

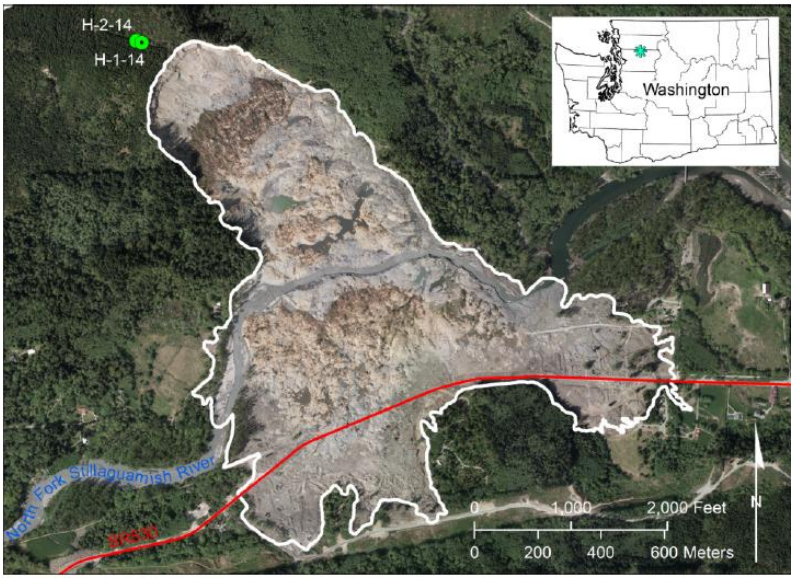

Figure 3.12: Oso Landslide Site Map [Shown are the locations of two boreholes, where samples for geotechnical testing were obtained for the report, with main geographical features of the area (Photo base and date: Washington State Department of Transportation, May 1, 2014)]

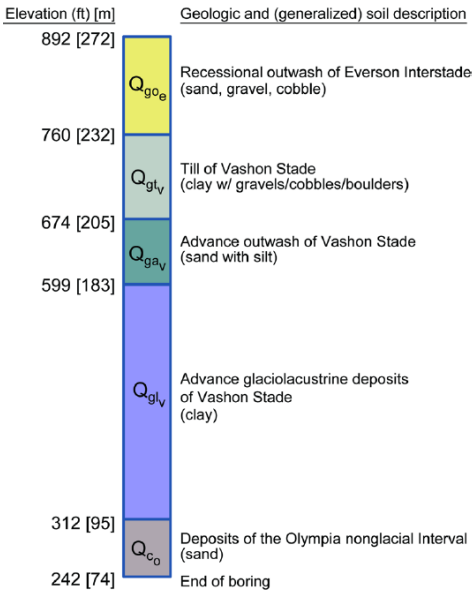

Figure 3.13: General Stratigraphic Glacial and Non-glacial Deposits Column forming the Oso Landslide Area. [Naming convention of Dragovich et al. (2003) were followed, and for presentation purposes, unit contacts are assumed to be horizontal (from Riemer et al., 2015)]

Geotechnical index testing on selected samples, depending on their sampling method (e.g., unit weight was measured only for samples taken and stored in protective tubes), and the soil type (e.g., Atterberg limits were performed only for plasticity showing samples), included water content (ASTM D2216-10), unit weight (ASTM D7263-09), specific gravity (Gs) (ASTM D854-14), grain-size distribution (ASTM D422-63 (2007)), Atterberg limits (ASTM D4318-10e1), and Unified Soil Classification System (USCS) Designation (ASTM D2487-11). The results of this geotechnical index testing, along with grain size curves for various samples are below. No data shows that the tests were either not or could not have been performed on these samples.

Sample no.	Depth below ground surface[1] (ft)	Mean elev.[2] (ft)	Sample type	Water content, w_c (%)	Moist unit weight, γ (lb/ft^3)	Specific gravity, G_s	Liquid limit, LL (%)	Plastic limit, PL (%)	Plasticity Index, PI (%)	Fines content (%)	Clay content (%)	USCS desig.
Recessional outwash of Everson Interstade (Qgoe)												
H-1-14-D2	39.0-40.5	850	Bulk							11	3	SW-SM
H-2-14-D1B	50.0-52.0	839	Brass liner	4.5	119.7							
H-1-14-D3	59.0-60.5	830	Bulk			2.73				14	3	SM
H-2-14-D2A	98.5-100.5	790	Brass liner	23.2	117.8							
H-1-14-D7	119.0-120.5	770	Bulk			2.73				44	5	SM
Till of Vashon Stade (Qgt_v)												
H-1-14-@176	176.0-178.0	713	Loose core		140.3[3]	2.76	40	18	22	56	22	CL
Advance outwash of Vashon Stade (Qga_v)												
H-1-14-C34A	242.5	648	Lexan tube	24.7		2.76				49	3	SM
H-1-14-C34B	245.5	645	Lexan tube	26.4		2.79	27	24	3	63	2	ML
H-2-14-C5L	271.0	619	Lexan tube			2.73	26	25	1	47	4	SM
Advance glaciolacustrine deposits of Vashon Stade (Qgl_v)												
H-1-14-C51	319.5-320.5	570	Loose core			2.81	53	21	32	98	40	CH
H-1-14-@354	353.0-355.0	536	Loose core			2.80	39	19	20	96	26	CL
H-1-14-C64	379.5-380.5	510	Loose core	26.0		2.81	58	24	34	100	45	CH
H-1-14-C72	418.0	472	Lexan tube	35.0	123.5	2.77	48	25	23	100	42	CL
H-1-14-C78	449.5-450.5	440	Lexan tube	28.6	122.2	2.78	57	24	33	100	38	CH
H-1-14-C86	487.5-490.5	401	Lexan tube	35.8	116.5	2.77	69	26	43	100	66	CH
H-1-14-C94	529.5-530.5	360	Lexan tube			2.81	70	25	45	100	57	CH
H-2-14-C9L	562.0	328	Lexan tube	26.4		2.79	54	25	29	99	35	CH
H-1-14-C103	572.0	318	Loose core			2.83	62	27	35	100	64	CH
Deposits of the Olympia nonglacial Interval (Qco)												
H-2-14-C11L	582.5	308	Lexan tube		140.0	2.76				18	3	SM
H-1-14-C114	627.5	263	Lexan tube	4.9		2.75				3	0	SP

Table 3.1: Geotechnical Index Test Data for Oso Landslide Deposits. [USCS desig.: United Soil Classification System designation (from Riemer et al., 2015)]

[1]Single values of depth represent those samples where the exact location of the sample is known within the core (as opposed to a range).

[2]Sample elevation is based upon an estimated ground surface elevation of 890±5 feet relative to NAVD88 and rounded to the nearest foot.

[3]For the till sample, only a dry density (γ_d) was measured

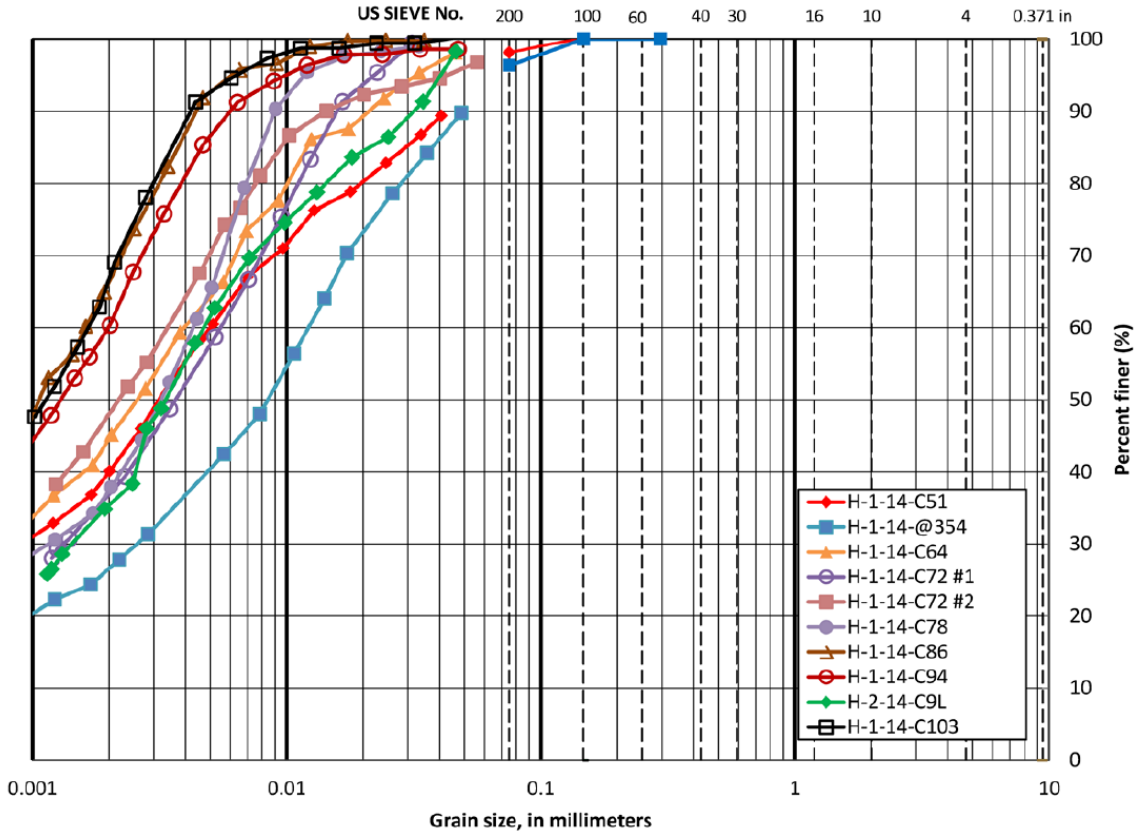

Figure 3.14: Grain-Size Curves for Advance Glaciolacustrine Samples [Hydrometer testing for data less than the No. 200 sieve, sieve testing for greater than the No. 200 sieve. From the same depth, two samples of H-1-14-C72 were tested as a consistency check, and average values are shown in Table 3.1 (from Riemer et al., 2015]

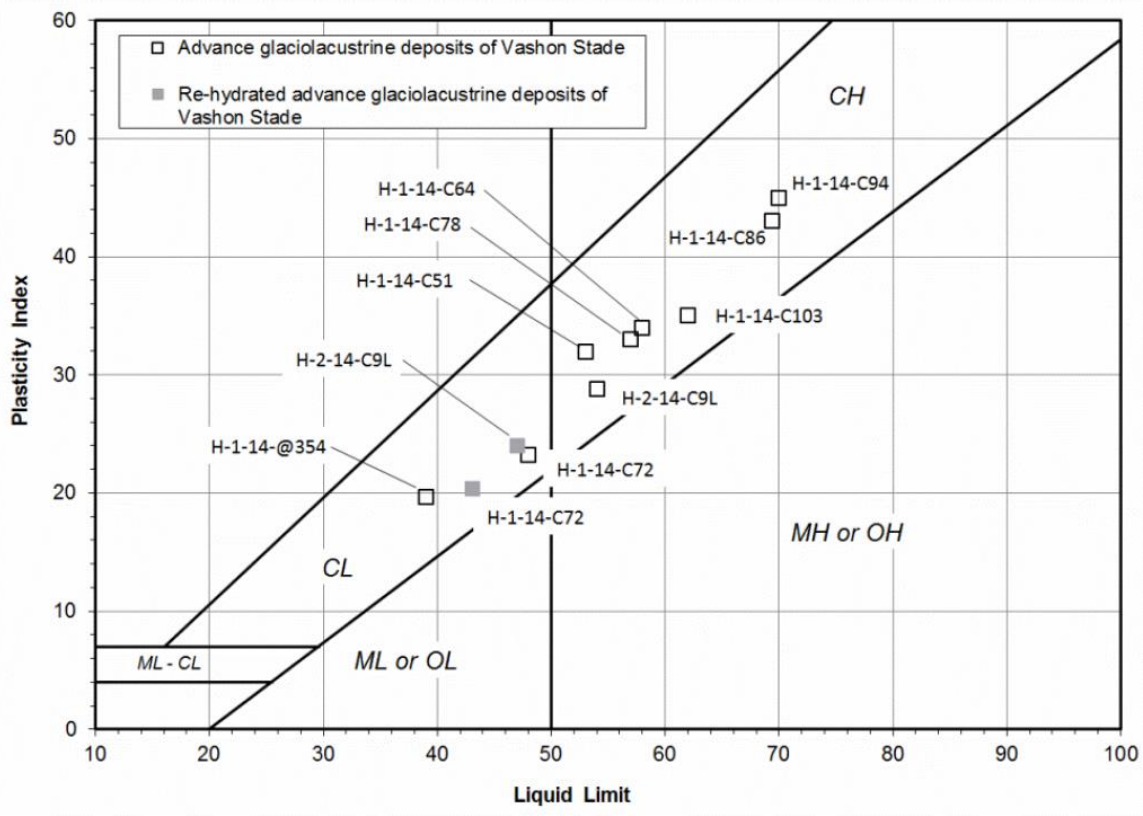

Figure 3.15: Plasticity Chart for Advance Glaciolacustrine Samples [Cx: Clay, Mx: Silt, Ox: Organic, xH: High plasticity, xL: Low plasticity (from Riemer et al., 2015)]

The deep coring and intact sampling of the materials behind the landslide headscarp seem to have provided a valuable insight into the intact sequence of the geological materials involved in this failure. In this phase, the subsequent geotechnical index testing and the resulting characterization of the selected samples generally confirm the stratigraphic sequence shown in Fig. 3.13. Furthermore, this data provides index test property values of adequate accuracy and spatial distribution through the stratigraphic section that can help develop geotechnical landslide models and can help estimate behavioral properties based on comparisons with similar glacial sediments from other landslide-prone areas in northwestern Washington (Savage et al., 2000).

Badger and D'Ignazio's (2018) study aimed to use geotechnical data from the small dataset of available published and public domain research to characterize, in general terms, geotechnical, geomorphic, and hydrogeological factors and their relative contribution to the deep-seated landslides' initiation within intact Qglv deposits; and within these deposits, to inform future hazard and risk assessments for first-time landslides. They conclude that a loss of cohesive strength rather than a hydroclimatic pore pressure response is, over the long term, the most important contributor to the reduction in stability and initiation of first-time landslides in Qglv deposits, in some cases.

Several tests such as standard penetration (ASTM D1586) (Landau Assoc., 1998; Galster and Laprade, 1991; Badger, 2015 and 2016), pocket penetrometer (ASTM WK27337) (Stark et al., 2017), hydraulic conductivity (Savage et al., 2000a; Morgan and Jones, 1995), Atterberg limits (ASTM 4318), laboratory vane shear (ASTM D4648), consolidation (ASTM D2435) (Stark et al., 2017; Laprade, 1982; Pyles et al., 2016; Riemer, 2016), torsional ring shear (ASTM D6467 and D7608) (Stark et al., 2017), and consolidated-drained direct shear tests (ASTM D3080) (Badger, 2016; Cooper Testing Laboratory, 2016; GeoTesting Express, 2016) were performed on the aforementioned advance glaciolacustrine clay.

Landslides which initiate earthen materials that have been previously unsheared are commonly called first-time landslides (Skempton and Hutchinson 1969). Qglv deposits are typically very stiff to hard, laminated to thinly-bedded, non-plastic silt to fat clay deposits (Mullineaux et al., 1965; Landau Associates, 1998; Badger, 2015 and 2016). The clay fraction consists mainly of illite, smectite, and chlorite (Gault, 2015).

Consistencies found to be very stiff to hard by standard penetration tests (ASTM D1586) (Landau Assoc., 1998; Galster and Laprade, 1991; Badger, 2015 and 2016). Table

3.2 presents the index properties established through laboratory testing (Landau Assoc., 1998; Riemer et al., 2015; Badger, 2016; GeoTesting Express, 2016).

Landslide	# of Samples	Moisture Content (%)*	Bulk Density (kg/m^3)*	SpG (Gs)*	LL*	PL*	PI*	LI*	Clay Content (%)*	Soil Classification	Reference
Oso	6	26-36 (30)	1870-1990 (1940)	2.77-2.81 (2.79)	48-70 (59)	24-26 (25)	23-45 (34)	−0.6-0.4 (0.1)	35-66 (47)	CL-CH	Riemer et al., 2015
Oso	14	24-42 (31)	1860-2010 (1940)	2.68-2.79 (2.74)	27-67 (49)	19-28 (22)	8-43 (27)	0.1-2.3 (0.4)	12-52 (27)	CL-CH	GeoTesting Express, 2016
Oso	78	12-41 (30)	1860-2160 (2020)	2.61-2.87 (2.78)	22-59 (44)	NP-31 (26)	NA-31 (19)	−1.7-2.0 (0.1)	16-52 (29)	ML-MH-CL-CH	Badger, 2016
Woodway	7	23-41 (30)			34-72 (41)	24-36 (25)	11-37 (17)	0-0.7 (0.3)		ML-MH	Landau Associates, 1998

Table 3.2: Geotechnical Index Properties of Qglv Deposits [* Value range (mean) (from Badger and D'Ignazio, 2018)]

The soil behavior, when sheared, was primarily plastic from the range of liquidity indices, with some samples indicating fragile and somewhat sensitive behavior (Holtz et al., 2011). The hydraulic conductivities of Qglv deposits ranging between 10^{-4} and 10^{-9} cm/s are reported in the Seattle area by Savage et al., (2000a). The ratio between horizontal and vertical conductivities was estimated for advance sand and silt deposits to be 100 - 200 by Morgan and Jones (1995); for Qglv deposits Badger and D'Ignazio (2018) expect similar or higher ratios.

Laprade (1982) did not detect any apparent correlation of pre-consolidation pressures with burial depth in his review of available consolidation testing data on Qglv deposits in the Seattle area. However, for samples proximal to high-conductivity stratigraphic units, a correlation of pre-consolidation pressure and burial depth was evident.

On relatively disturbed tube samples from the Oso landslide, constant strain-rate consolidation tests resulted in maximum pre-consolidation pressures from 1200 to 3600 kPa, and overconsolidation ratios (OCRs) ranging from 1 to 1.2, where Qglv is recently

exhumed below the new slide surface (Pyles et al., 2016; Riemer, 2016). Stark et al. conducted three consolidation tests on block samples of landslide debris for the Oso landslide, resulting in a maximum pre-consolidation pressure of 1628 kPa and OCRs ranging from 4 to 8.

There are few published or public-domain geotechnical investigations including shear strength characterization of intact Qglv deposits by laboratory testing and/or failure back-analysis. These include the landslides during the Seattle Freeway's construction in the 1960s (Palladino and Peck, 1972); the Woodway landslide in 1997 (Landau, 1998; Arndt, 1999; Savage et al., 2000a, 2000b); and the Oso landslide (Badger, 2016; Pyles et al., 2016; Cooper Testing Laboratory, 2016; GeoTesting Express, 2016; Stark et al., 2017).

Palladino and Peck (1972) reported in Seattle major differences in peak and residual strength values for glacially over-consolidated clays similar to those at Oso Landslide site with peak strength of 62 kPa (9 psi) cohesion and an angle of friction of 35°, residual strength characterized by zero cohesion and a frictional angle of 14° to 18° for disturbed clay.

For the Oso landslide, using consolidated-drained direct shear testing (ASTM D3080) and shearing samples perpendicular to bedding (Badger, 2016) and parallel to bedding (Badger, 2016; Cooper Testing Laboratory, 2016; GeoTesting Express, 2016) anisotropic strengths were examined. Failure envelopes are shown in Fig. 3.16.

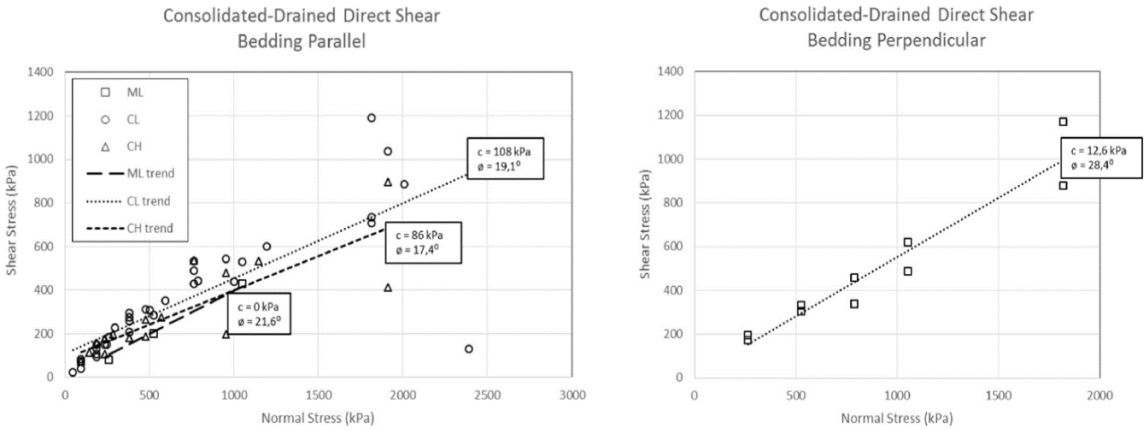

Figure 3.16: Direct Shear Test Peak Drained Strength Envelopes from on Samples Sheared Parallel to Bedding and Perpendicular to Bedding. (from Badger and D'Ignazio, 2018)

From the direct shear tests, typical stress-strain curves indicate brittle behavior with considerable strain softening to plastic behavior and minor strain hardening; between 3 and 7% strain, peak strength is commonly reached.

Torsional ring shear tests for fully softened (ASTM D7608) and residual (ASTM D6467) strengths for the Oso landslide have been performed (Badger, 2016; Cooper Testing Laboratory, 2016; Stark et al., 2017). Table 3.3 summarizes these data.

Reference	Peak Isotropic		Peak Anisotropic-Parallel		Peak Anisotropic-Perpendicular		Fully Softened	Residual
	Cohesion (kPa)	Friction	Cohesion (kPa)	Friction	Cohesion (kPa)	Friction		
Palladino and Peck, 1972	62	35°	–	–	–	–	–	13.5–17.5°
Arndt, 1999			–	–	–	–	–	
- ML (upper)	0	25°	–	–	–	–	–	22–24°
- CL/CH (lower)	0–38	15–27°	–	–	–	–		6–27°
Savage et al., 2000a	12	24°	–	–	–	–	–	–
Pyles et al., 2016	5–10	20°	–	–	–	–	20°	12°
Badger, 2016	–	–			12.6	28.4°		12–22°
- ML			0	21.6°				11.7–13.3° *
- CL			108	19.1°				20.4–22.2°
- CH			86	17.4°			22.8–23.2°	15.1–18.8°
Stark et al., 2017	–	–	–	–	–	–		
- ML/CL							25–34°	20–27°
- CH							21–32°	12–19°

Table 3.3: Shear Strength of Qglv Deposits [* Residual strength torsional ring shear results for dark gray, organic-rich silt (from Badger and D'Ignazio, 2018)]

Badger and D'Ignazio (2018) have synthesized available, hydrogeological and hydroclimatic data for three first-time landslides, including Oso landslide, in order to examine the role of precipitation in landslide initiation in intact Qglv deposits. They included a description of a fourth large-volume landslide, which occurred during summer dry season, with only existing surficial characterization.

The role of shear strength was also investigated. Badger and D'Ignazio (2018) found that the strength loss is significant and precipitous from the onset of failure. Through an intact overconsolidated clay test with pore pressure reinflation for long-term, Carey and Petley (2014) documented such catastrophic failure almost three months after the last stress state increase. Using the Morgenstern and Price (1965) limit equilibrium method with SLOPE/W 2018 software (Geoslope, 2018), they assess the pre-failure stability of three landslides for drained conditions, applying fully softened shear and the peak anisotropic (bedding-perpendicular and bedding-parallel) strengths of Qglv deposits shown in Table 3.3. The software discretizes the horizontal and vertical components for an anisotropic strength based on the slide surface orientation for each slice (gently sloping surfaces activate horizontal strength mainly, whereas steep surfaces activate vertical strength).

For Oso landslide, Fig. 3.17 serves as the soil profile model for back analysis, while Fig. 3.18 represents an average pressure head distribution estimated from the 3 to 4-year record of continuous pore pressure measurements for stability analyses. The anisotropic peak and fully softened strengths resulted in safety factors of 1.15 and 1.00 respectively, achieved without the assumption of the prior movement of the debris from the slope, the process that has been inferred by previous studies.

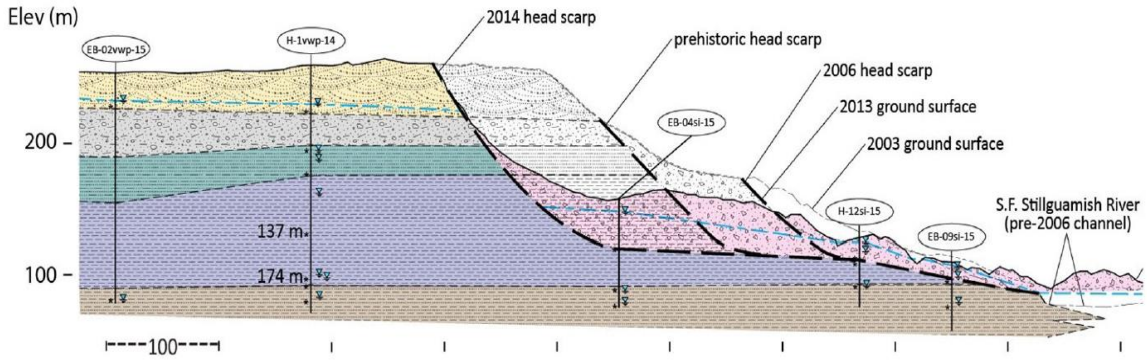

Figure 3.17: Geologic Section of the Oso Landslide (Interpreted), Based on 2014 and 2015 Geotechnical Borings (from Badger and D'Ignazio, 2018)

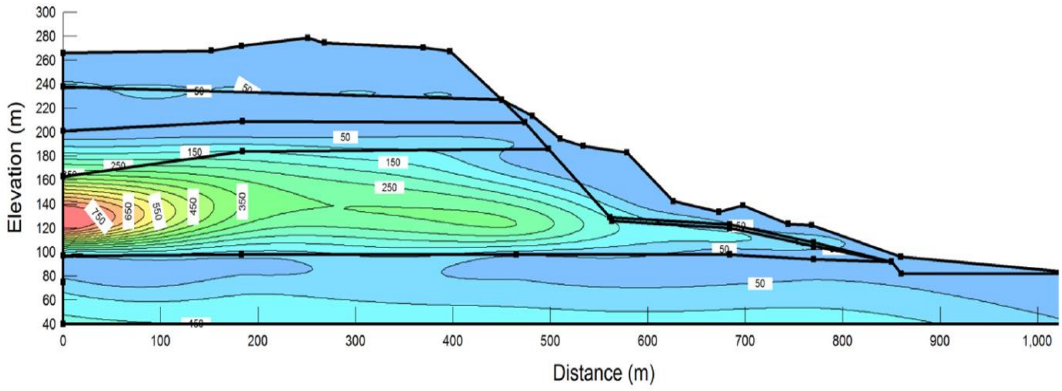

Figure 3.18: Pressure Head Distribution Estimation, 50 kPa Contours for the Oso Landslide (from Badger and D'Ignazio, 2018)

In order to evaluate the effect of anisotropy and the progressive strength loss on stability, they carried out sensitivity analyses on cohesion and friction both parallel and perpendicular to bedding. Strength parallel to bedding had much greater stability control than perpendicular to bedding mobilized strength (Fig. 3.19).

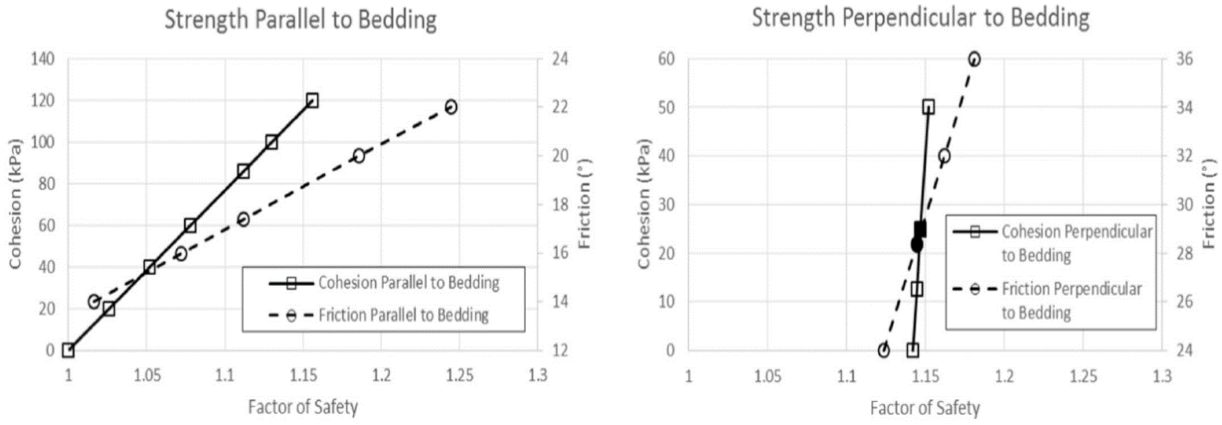

Figure 3.19: Factor of Safety Sensitivity to Strength Parameters (a) Parallel (φp=17.4° and c=86 kPa) and (b) Perpendicular (φp=28.4° and c=12.6 kPa) to Bedding (from Badger and D'Ignazio, 2018)

The back-analysis using the peak anisotropic and fully softened strengths and pore pressure regimes for intact Qglv deposits replicated the observed Oso landslide failure surface closely. Due to the remolded material being used, the test results reported are likely higher than horizontal shear field conditions, because of the bedding structure preservation in natural slopes. Furthermore, the modeled stability at peak anisotropic strength provided marginal stability and failure was achieved with a fully softened strength value. These results correspond to the hypothesis that slopes on Qglv deposits are stable, although rather marginally, when close-to-peak anisotropic strength conditions exist, and that the peak anisotropic strengths are reasonably approximate to the field conditions from direct shear tests.

Also, the long-understood behavior of loss of strength in overconsolidated silts and clays leads to instability for the measured range of fully softened strength. Stress loss is believed to occur primarily due to cohesion loss, based on comparable frictional strengths of fully softened and peak test results.

Stark et al. (2017) also presented the fully softened and residual strength envelopes for advance glaciolacustrine clay deposits (Fig. 3.20). Table 3.4 represents the summary of index properties and shear strength testing for upper and lower glaciolacustrine deposits (Stark et al. 2017). The fully residual and softened friction angles in Table 3.4 are in agreement with empirical correlations in Stark and Hussain (2013) and Gamez and Stark (2014) for the measured liquid limit and clay-size fraction values in Table 3.4. The previous laboratory vane shear and pocket penetrometer data and confirms that the undisturbed, overconsolidated glaciolacustrine clays are not sensitive and susceptible to significant strength loss like quick clays. The samples were obtained during various site visits by excavating with a shovel and hand trowel so that the samples are a better representation of the natural water content than surficial soils and thus not significantly drier or wetter than weather conditions at the time of the 2014 landslide.

Engineering property	Low-plasticity advanced glaciolacustrine	High-plasticity advanced glaciolacustrine
Liquid limit [ASTM D4318-10 (ASTM 2010a)]	34–38 (average = 36)	52–60 (average = 55)
Plastic limit	21–24 (average = 22)	25–29 (average = 26)
In situ water content (%)	23–28 (average = 25)	32–37 (average = 34)
Liquidity index	0.2–0.25	0.27–0.3
Sensitivity	1.4–2.2	2.8–3.3
Clay-size fraction (% <0.002 mm) [ASTM D422-07 (ASTM 2007)]	31–36%	51–56%
Fully softened friction angle (effective normal stresses of 12, 50, 100, and 400 kPa)	25–34°	21–32°
Residual friction angle (effective normal stresses of 50, 100, 400, and 700 kPa)	20–27°	12–19°

Table 3.4: Summary of Index Property and Shear Strength Testing for Upper and Lower Glaciolacustrine Deposits (Stark et al. 2017)

After the measured sensitivities and shear strengths, the failure mechanism investigation started focusing on the water-filled colluvium along the slope toe as the material that could have undergone a significant undrained strength loss and contributed to the 1.5-km run-out instead of the intact and heavily overconsolidated advanced glaciolacustrine clays (Stark et al., 2017).

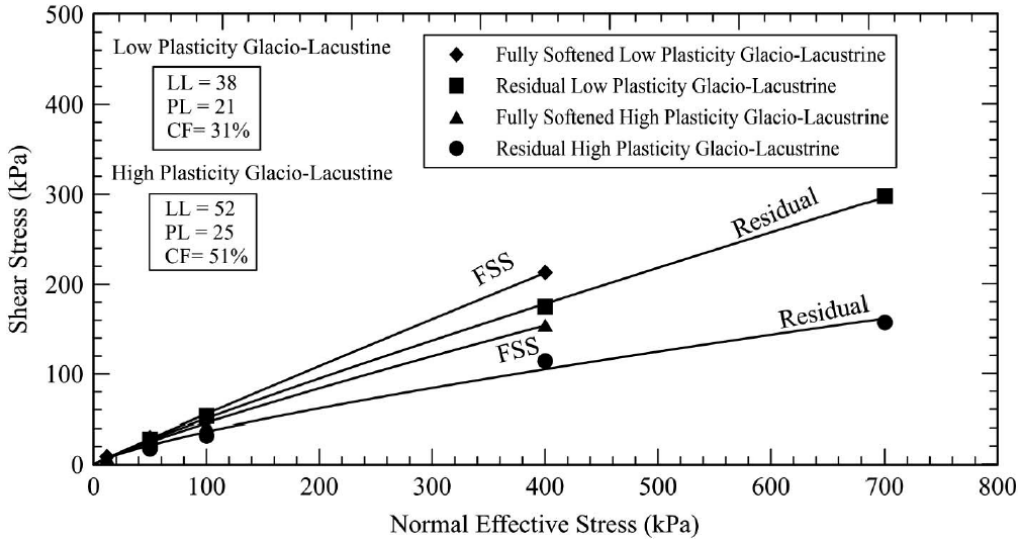

Figure 3.20: Residual and Fully Softened Strength Envelopes for Advance Glaciolacustrine Clay Deposits (from Stark et al., 2017)

3.4 Summary

First of all, the general information on Oso landslide, followed by the literature on hydrological mechanics, stability, subsurface conditions, material properties, and the history of the landslide were presented in this chapter. Second, the geotechnical soil characterization of Qglv deposits was summarized, following which, through several tests conducted by researchers, geotechnical, geomorphical and hydrogeological characteristics were examined.

CHAPTER 4: INVESTIGATION OF COLLUVIUM AND THE RUN-OUT

4.1 Introduction

Investigation of the colluvium by comparison of the colluvium volume with the run-out, and the experimental program, with test results and pre-analyses were presented in this chapter. Later, the results were also analyzed in greater detail as a summary.

4.2 Comparing the Volumes of the Colluvium and the Run-out

Using the following figures obtained from the literature, volume of the colluvium before and after the Oso landslide occurred was calculated.

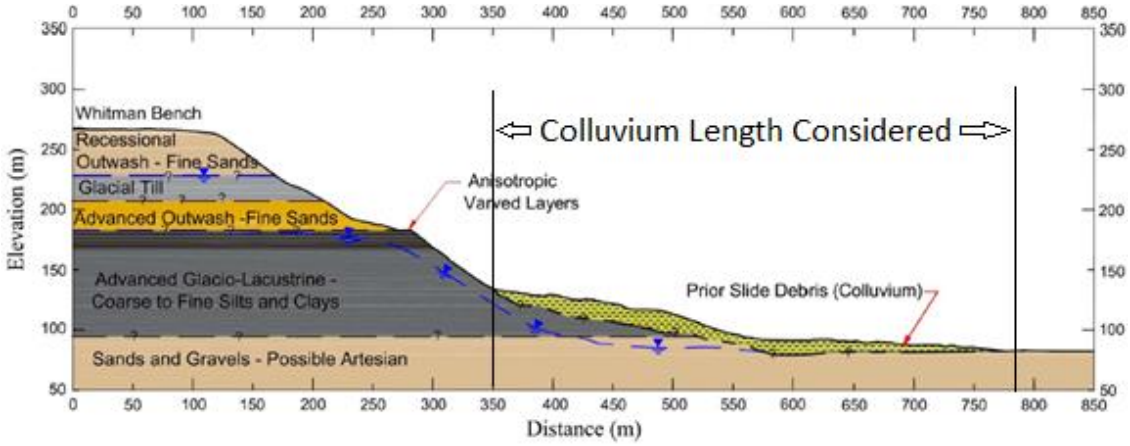

Figure 4.1: Slope Cross Section at Location in Figure 3.3 prior to 2014 Landslide (from Stark et al., 2017)

According to Fig 4.1, the total pre-2014 colluvium area before landsliding was calculated and using the width provided in Figure 4.3 (red zone between the yellow lines), the volume was found to be approximately 2.3×10^6 m^3. Using the topographic profile for height approximations presented in Fig. 4.2 (between the marked lines) and the plan view for width approximations in Fig. 4.3 (red zone between the pink lines), the total volume of

material after 780.78 m horizontal distance to the landslide terminus was found to be approximately $5.0x10^6$ m^3.

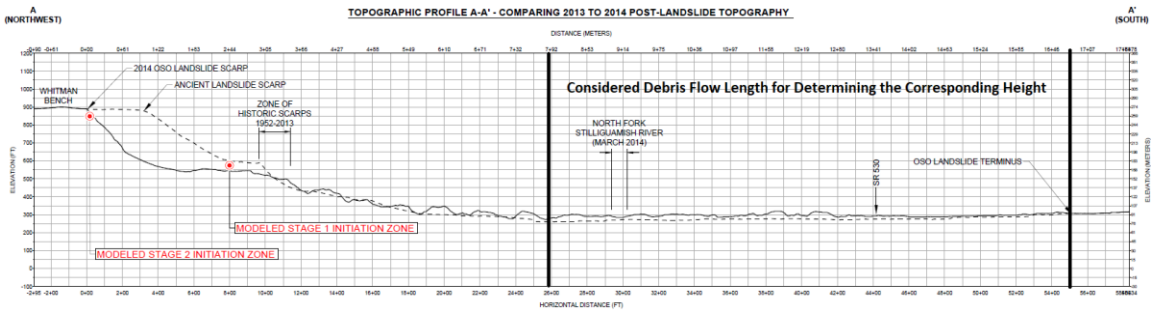

Figure 4.2: Profile Illustrating Starting Locations for Stage 1 and Stage 2 Events at Oso Landslide (Keeton et al., 2014)

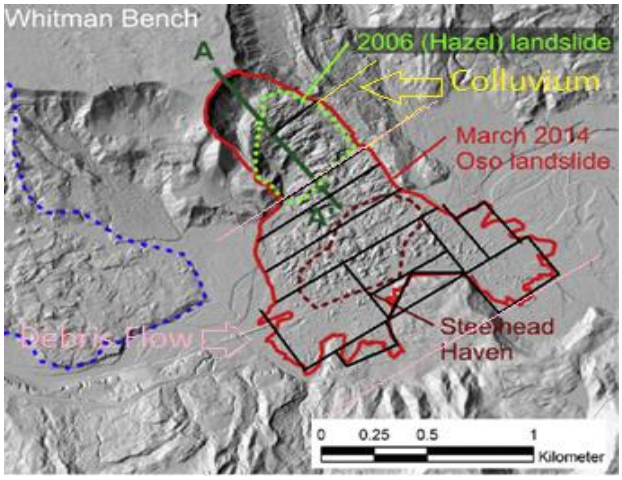

Figure 4.3: Detail of Area used for Calculation of Width for Volume (from Wartman et al., 2016)

This means that other materials, which might include the previously in-place outwash, till, lacustrine deposits, and/ or sediments in the river bed have flowed together to the landslide terminus. It also supports the hypothesis that the colluvium was pushed by the slide mass behind, and it was not the entire debris flow.

This result agrees with the calculated volume of materials in the literature, which had been found to be approximately $7.6x10^6$ m^3. However, rather than being 50% of the total volume, it was found to be approximately 31% of the total volume for Stage 1 (Flow of the Colluvium). Thus, as explained earlier, it should be noted that those relationships are very empirical, and not very helpful in understanding the mechanisms causing the mobility, and therefore in providing information to predict the mobility.

4.3 Laboratory Tests

4.3.1 INTRODUCTION

Water content is probably the most often measured soil characteristic for engineering purposes. Other, possibly the oldest and most widely accepted of all engineering tests on fine-grained soil which are used as an aid to estimate the engineering characteristics of soils for a variety of engineering purposes, including soil classification, earthwork specifications and in estimating the engineering properties of soils are the liquid limit, plastic limit, and the related indices. Lastly, one-dimensional consolidation tests are one of the main types of tests performed for geotechnical engineering purposes. Consolidation tests are intended to determine the magnitude and rate of consolidation of the soil if it is laterally restrained and axially drained, while under incrementally applied controlled-stress loading (ASTM2435/D2435M-11). This chapter discusses in depth the equipment and methods used in these tests on advance glaciolacustrine clay specimens obtained from Oso landslide site after the event. The various materials and the equipment used in the experiments are presented. The specimen preparation as an important part and the steps needed to prepare the specimen are provided. Liquid and Plastic (Atterberg) Limits and Plasticity Index Tests and One-Dimensional Consolidation Tests were conducted on the advance glaciolacustrine clay specimens obtained.

4.3.2 MATERIALS

This section provides information on the specific properties and known properties of the tested advance glaciolacustrine clay specimens. There are also some other materials discussed, such as water, filter papers, and porous stones.

4.3.2.1 Advance Glaciolacustrine Clay (S1 and D5 specimens)

Two specimens from the Oso landslide site have been obtained. D5 was obtained on 04/24/2014, while S1 was taken on 05/24/2014 at around 11:45 A.M. They have been preserved in plastic tight-seal bags before laboratory testing (Fig. 4.4).

Figure 4.4: S1 and D5 Advance Glaciolacustrine Clay Samples

Table 4.1 presents geotechnical index properties for the advance glaciolacustrine (Qglv) deposits from different references. With these results, they have an average natural moisture content, w_c, of 30%, a bulk density of 1967 kg/m^3, a specific gravity of 2.77,

liquid limit of 48%, 25% plastic limit, 24% plasticity index, liquidity index of 0.23, and 34% clay content.

Landslide	# of Samples	Moisture Content (%)*	Bulk Density (kg/m^3)*	SpG (Gs)*	LL*	PL*	PI*	LI*	Clay Content (%)*	Soil Classification	Reference
Oso	6	26-36 (30)	1870-1990 (1940)	2.77-2.81 (2.79)	48-70 (59)	24-26 (25)	23-45 (34)	−0.6-0.4 (0.1)	35-66 (47)	CL-CH	Riemer et al., 2015
Oso	14	24-42 (31)	1860-2010 (1940)	2.68-2.79 (2.74)	27-67 (49)	19-28 (22)	8-43 (27)	0.1-2.3 (0.4)	12-52 (27)	CL-CH	GeoTesting Express, 2016
Oso	78	12-41 (30)	1860-2160 (2020)	2.61-2.87 (2.78)	22-59 (44)	NP-31 (26)	NA-31 (19)	−1.7-2.0 (0.1)	16-52 (29)	ML-MH-CL-CH	Badger, 2016
Woodway	7	23-41 (30)			34-72 (41)	24-36 (25)	11-37 (17)	0-0.7 (0.3)		ML-MH	Landau Associates, 1998

Table 4.1: Geotechnical Index Properties of Qglv Deposits [* Value range (mean) (from Badger and D'Ignazio, 2018)]

Fig. 3.14 shows grain size distribution curves for the advance glaciolacustrine clay in Oso landslide site, as explained earlier. Fig. 4.5 represents S1 and D5 samples before testing.

Figure 4.5: S1 (on the left) and D5 (on the right) Samples

4.3.2.2 Other Materials

The additional materials used included the porous stones, filter papers, and water. The porous stones used for consolidation setups were typical standard porous stones. The porous stones allowed water to drain through the stone evenly. The stone was approximately ¼" in thickness and 2.9" in diameter for the bottom; 0.4" (thickness), and 2.47" (diameter) for the top. Glass microfiber Whatman brand filter papers have been used to prevent fines from clogging the porous stones. The filter papers were cut to fit the diameter of the specimen on top, and to cover the porous stone around the consolidation ring on the bottom. The water used to prepare the specimens for the tests before consolidation was simply deaired/ distilled water. The same water has been used for the consolidation test of sample S1, while tap water has been used for specimen preparation and during consolidation test of sample D5.

4.3.3 GENERAL REMOLDED SPECIMEN PREPARATION

The soil samples shown in Fig. 4.5 were pulverized using a mortar, rubber head pestle and hammer, and passed through 425-μm (No. 40) sieve, with the help of a brush (Fig. 4.6). Purpose of remolding was to better represent the material as it was in the disturbed colluvium on the slope.

Figure 4.6: First Pulverization of the Obtained Samples

4.3.4 PLASTICITY TESTS

4.3.4.1 Equipment

A mechanical liquid limit device consisting of a brass cup suspended from a carriage designed to control its fall onto the surface of a block of resilient material that serves as the base of the device was used. The apparatus used for the Atterberg limits tests are shown in Fig. 4.7.

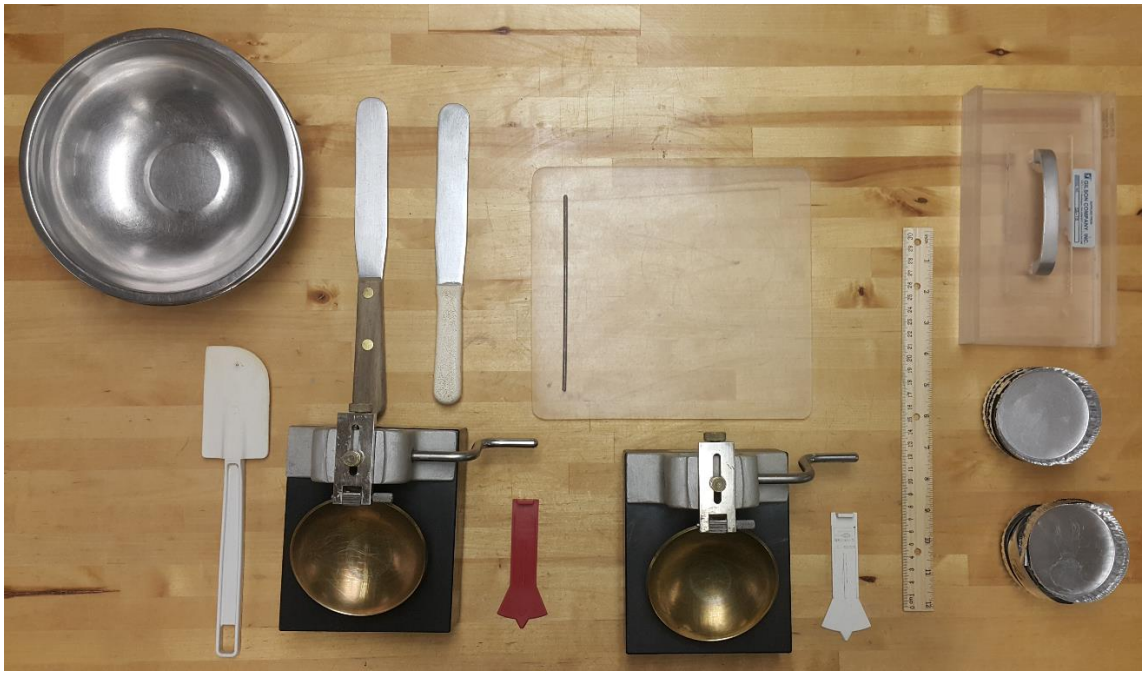

Figure 4.7: Apparatus Used for Liquid Limit, Plastic Limit, and Plasticity Index Tests

The instrument used was a liquid limit device operated by hand, having rubber feet, a brass cup, a cam, and carriage. The cam is designed to raise the cup smoothly and continuously to its maximum height over a distance of at least 180-degrees of cam rotation, without developing a downward or upward velocity when the cam follower leaves the cam. A flat grooving tool made of plastic with height adjustment gauge was also used (Fig. 4.8).

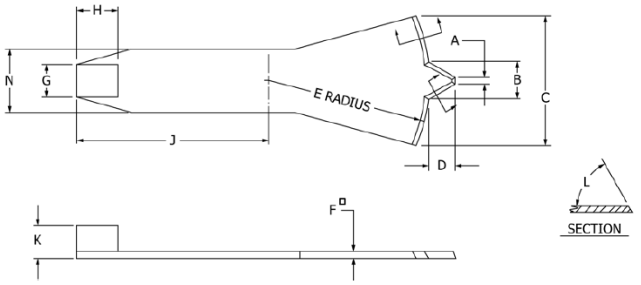

Figure 4.8: Grooving Tool (from ASTM 4318-17)

A ground glass plate was used for rolling plastic limit threads, with a rod of 1/8" diameter (3.2mm) to determine the thread diameter before collecting for plastic limit water content determinations.

Small, corrosion-resistant water content containers were used for water content determination for liquid and plastic limit tests, along with mixing and storage porcelain dishes, spatulas and wash bottles when necessary. Drying oven used for water content was meeting the requirements of ASTM D2216. 425-μm (No. 40) sieves have been used earlier during specimen preparation, which will be discussed later in the specimen preparation section. For this and following tests, balances meeting the requirements of ASTM D4753 were used for weighing specimens and determining the water content.

4.3.4.2 Specimen Preparation

Dry specimen preparation procedure described in ASTM D4318-17 was followed. All the samples (S1 and D5) were passed through the 425-μm (No. 40) sieve, except for a negligible soil fraction that was retained on the sieve (Fig. 4.9).

Figure 4.9: (a) Soil Retained on 425-μm (No. 40) Sieve, and (b) Fiber-Like Materials Removed from the Samples

Approximately 300 g of material was prepared by mixing thoroughly with deaired/distilled water on the glass plate or mixing dish using the spatula prior to beginning the tests.

4.3.4.3 Methods

Atterberg limits and plasticity index tests were performed on the samples, S1 and D5. ASTM D4318-17 standard test method was followed, and the tests are in general compliance with the ASTM designation. Approximately 300 g of material for the liquid limit and plastic limit test was used for each sample (S1 and D5).

4.3.4.3.1 Liquid Limit Test Procedure

Liquid Limit Test Method A (multipoint method) was followed, steps of which are provided below:

1. 150-200 g material passing 425-μm (No. 40) sieve was used, as recommended by the ASTM.
2. Specimen preparation procedure II (dry preparation) was followed as described in ASTM D4318-17, which was mentioned previously.

3. The sample (soil) was thoroughly remixed in the mixing dish and its water content adjusted until the consistency of the liquid limit device requires about 25 to 35 cup drops to close the groove.
4. A portion of the soil was placed in the cup of the liquid limit device using a spatula at the point where the cup rests on the base, squeezes down and spreads to a depth of around 10 mm at its lowest point to form an approximate horizontal area. Attention has been paid to remove air bubbles from the soil pat but form the pat with the fewest possible strokes. Unused soil was covered and kept in the mixing dish to retain the soil moisture.
5. In the soil pat, a groove was formed with the tool pulled forward by means of the ground, on a route that connects the highest point to the lowest point on the rim of the cup. When the groove was cut, the grooving tool was held against the cup surface and drawn in an arc, which kept the tool perpendicular to the cup surface throughout its movement. (Fig. 4.10).
6. The cup was lifted and dropped by turning around 2 drops a second until the two halves of the soil pat came into contact in a distance of 13 mm at the bottom of the groove. This distance was verified using the thickness of the grooving tool.
7. Number of drops (N), required to close the groove was recorded for four different trials, one of which had a range of 15-20 blows; one had 20-25 blows; another one 25-30 blows; and finally 30-35 blows.
8. A water content specimen was obtained by removing a piece of soil approximately the width of the spatula from the edge to the border of the groove cake at the right angle and including the part of the groove in which the soil was flowing together and placed in a container of known weight, and weighed right away.

9. Remaining soil was returned to the mixture in the dish. The cup and the grooving tool were washed, dried, and reattached to the carriage for the next trial.
10. The entire soil specimen was remixed by adding deaired/distilled water when it was required to decrease the drops to close the groove, increasing the water content. If the moisture content was high, a Milwaukee brand, model #1220 heat gun (1200W) was used in low setting, from approximately 10” distance to the soil mixture.
11. The water content was determined for each specimen from each trial in accordance with ASTM D2216-10.
12. The liquid limit was evaluated after all the water contents were determined and the points were plotted on the flow curve.

Figure 4.10: View of Liquid Limit Test Device

4.3.4.3.2 Plastic Limit Test Procedure

Plastic Limit Rolling Procedure I (hand rolling) was followed in steps as described below:

1. Approximately 20 g of soil was chosen from the material prepared for the liquid limit test from the remaining soil after the liquid limit test was completed.
2. The water content of the soil was reduced to a consistency, to which it can be rolled, by spreading, without sticking to the hands, mixing continuously on the glass plate, or in the mixing dish. When needed, drying process was accelerated using the same heat gun used, and explained earlier.
3. A portion of 1.5 to 2.0 g was selected from this plastic limit specimen and formed into an ellipsoidal mass.
4. It was rolled by hand (Procedure I). The mass was rolled between the palm or finger and the base glass platform with enough pressure to roll the mass over its entire length into a thread with a uniform diameter of 3.2mm (1/8") within no more than 2 minutes. A 3.2mm diameter rod was used to verify this diameter (Fig. 4.11).
5. The portions of the crumbled thread were collected and placed in a known-mass container.
6. From the plastic limit specimen, further 1.5 to 2.0 g of soil was selected, and Step 1 to 5 were repeated until the container had at least 6 g of soil.
7. Step 1 to 6 were repeated to make another container with at least 6 g of soil.
8. Water content of soils were determined in accordance with ASTM D2216-10, average of which giving the plastic limit (PL).

Figure 4.11: View of Plastic Limit Test

4.3.4.4 Sources of Error

4.3.4.4.1 Liquid Limit Tests

Operator Errors

The operator can make a number of liquid limit test errors, some of which can have a significant effect on the results. Some of the possible areas of trouble include:

1. In the brass cup, too much or too little soil: Sufficient soil should be placed in the cup so that the maximum thickness is about 1 cm.
2. Rate of blows: The rate at which the crank is turned on the liquid limit device can affect the outcomes. ASTM specifies that the crank should be rotated at 120 blows per minute.
3. Smoothness of the cup: A thin but hardened crust may develop if fine-grained soil is allowed to dry out in the brass cup for 5 or 10 minutes. This may result in a much rougher surface than in a clean cup. Therefore, it is important for all tests to use a clean cup.
4. Height of fall: A common mistake is to adjust the fall height incorrectly. It should be adjusted to 1 cm.

Influence of Drying the Soil Before Testing

The liquid limit test ASTM specification states that the soil used in the test should pass a No. 40 sieve. A fine-grained soil cannot be sieved at its natural water content. The standard procedure for performing a liquid limit test is therefore to air-dry the soil and then pulverize it before use.

4.3.4.4.2 Plastic Limit Tests

The main source of the operator error is probably simply a lack of care in testing. The soil must be rolled to the right diameter (1/8 inch) before the thread breaks down. If the thread diameter is not 1/8 "or the operator does not care about how the thread is rolled out, incorrect results will be obtained.

4.3.4.5 Test Results

Four water content specimens were taken for each sample, for the ranges of drops of 15-20, 20-25, 25-30, and 30-35 using the *Liquid Limit Method A (Multipoint Method)*. The relationship between the water content, w_c, and the corresponding number of drops, N, of the cup is plotted on a semilogarithmic graph with the water contents on the arithmetical scale as ordinates, and the number of drops on a logarithmic scale as abscissas. The best fitting straight line is drawn through the plotted points, and the water content regarding the intersection of the line with the 25- drop abscissa as the liquid limit, LL, of the soil and rounded to the nearest whole number.

Table 4.2 presents the water contents vs. the number of drops for liquid limit determination.

Water Content, w_c (%)	Drop #, N
50.6	15
47.2	26
46.1	30
45.0	34

Table 4.2: Corresponding Water Contents at Number of Drops for S1

The following figure illustrates the graphical method and the obtained liquid limit, LL, value for the S1 clay sample. As a result, S1 has a liquid limit of 48%.

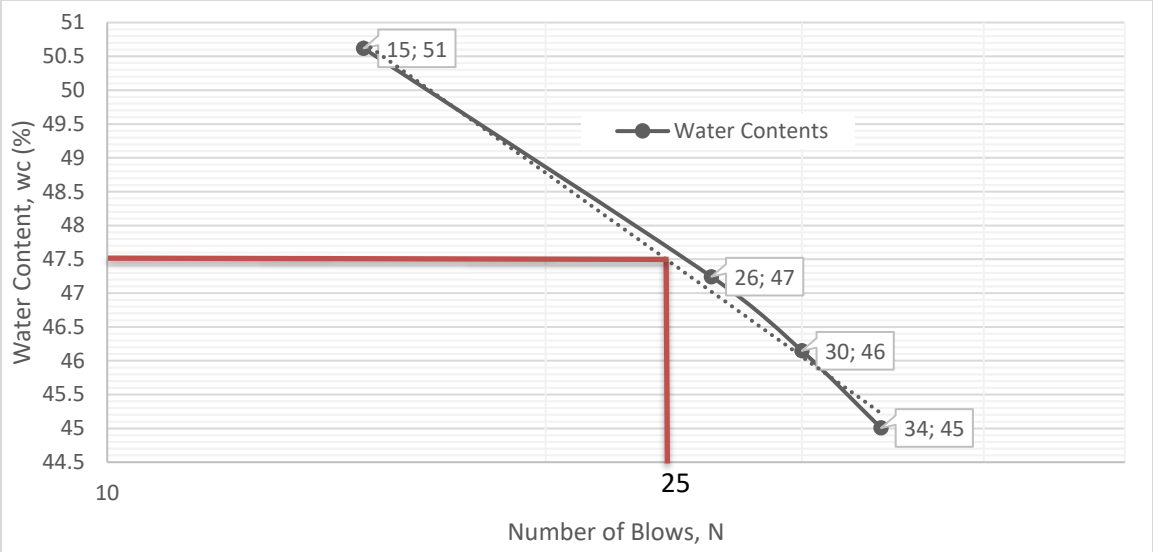

Figure 4.12: Determination of Liquid Limit for S1

The plastic limit, PL, water contents obtained are shown in Table 4.3 below. The average of the two water contents obtained is the plastic limit for S1, which is 25%.

Weight of Container (g)	Weight of Container Plus Wet Soil (g)	Weight of Container Plus Dry Soil (g)	Water Content, w_c (%)
2.26	10.63	8.95	25.1
2.32	8.49	7.29	24.1

Table 4.3: Corresponding Water Contents for Plastic Limit for S1

Plasticity index, PI, for S1 is calculated as follows:

$$\boldsymbol{PI = LL - PL}$$

$$PI = 48 - 25 = 23$$

Table 4.4 presents the water contents vs. number of drops for liquid limit determination.

Water Content, w_c (%)	Drop #, N
51.5	18
50.5	21
47.7	28
45.8	33

Table 4.4: Corresponding Water Contents at Number of Drops for S1

The following figure represents the graphical method and the obtained liquid limit, LL, value for the D5 clay sample. As a result, liquid limit of D5 was determined as 49%.

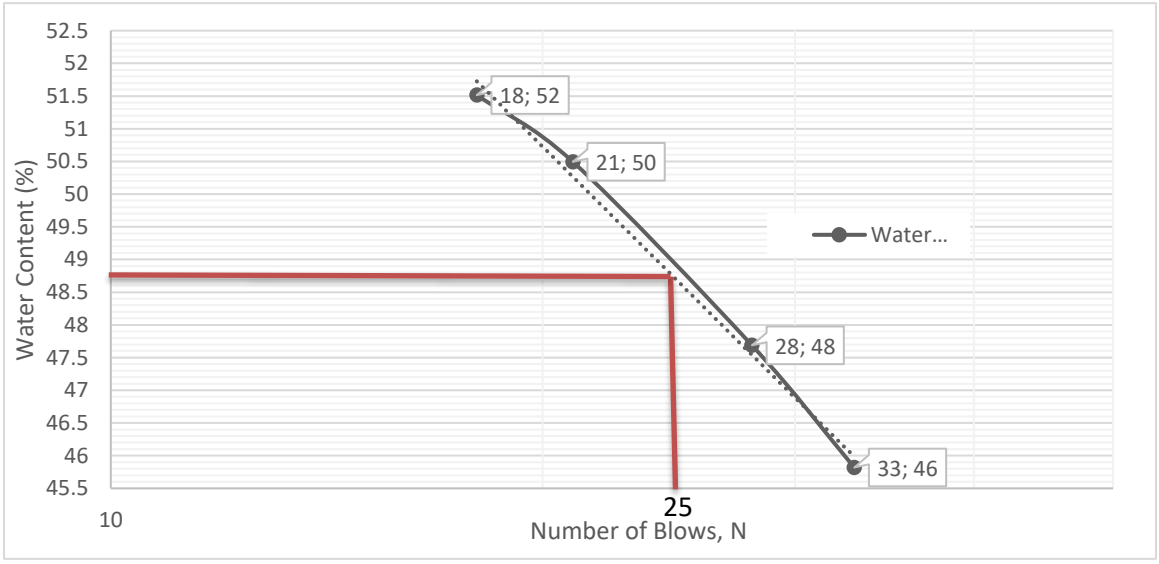

Figure 4.13: Determination of Liquid Limit for D5

The plastic limit water contents obtained are presented in Table 4.5 below. The plastic limit, PL, for D5, which is the average of the two water contents obtained is 24%.

Weight of Container (g)	Weight of Container Plus Wet Soil (g)	Weight of Container Plus Dry Soil (g)	Water Content, w_c (%)
2.54	9.68	8.33	23.3
2.25	8.12	6.96	24.6

Table 4.5: Corresponding Water Contents for Plastic Limit for D5

Plasticity index, PI, for D5 is calculated as follows:

$$\boldsymbol{PI = LL - PL}$$

$$\boldsymbol{PI = 49 - 24 = 25}$$

4.3.4.6 Pre-Analysis of the Test Results

Using the obtained Atterberg limits, plasticity charts from the literature were used to determine the characteristics of the tested samples. Undrained shear strengths were found using some of the reliable equations.

Fig. 4.14 illustrates plasticity indices against liquid limits for various soils (Lambe, 1951). Casagrande (1948) had collected similar data and represented them on the plasticity chart as shown in Fig. 4.15.

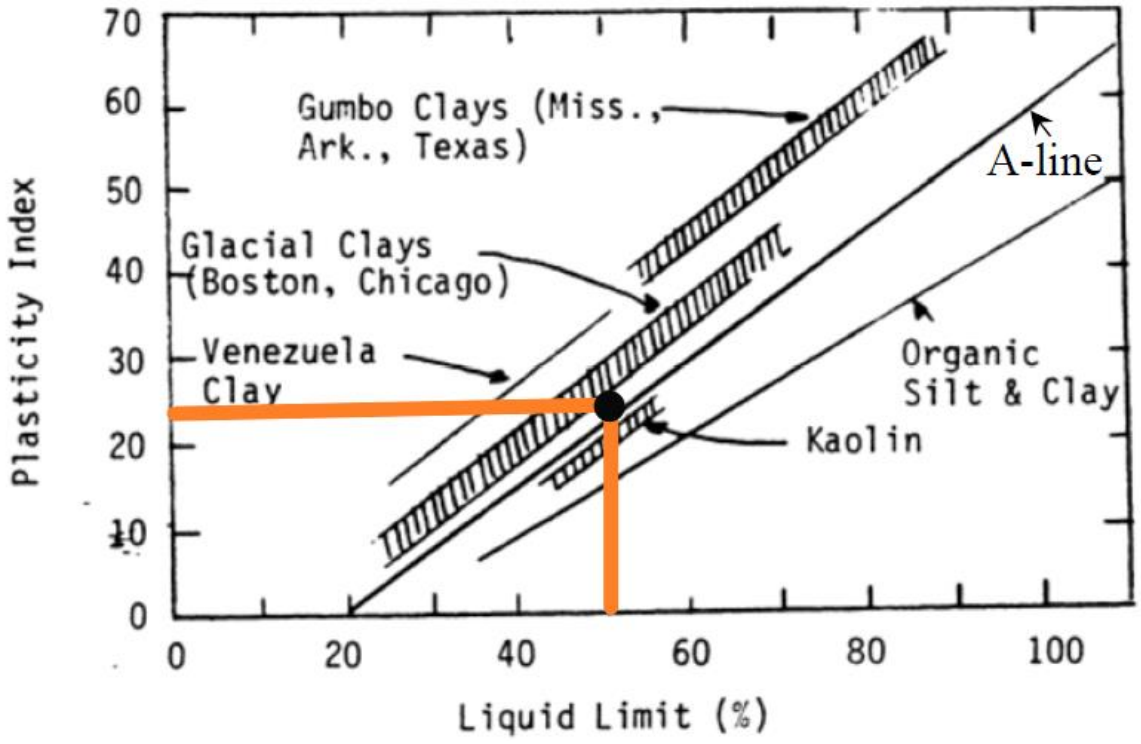

Figure 4.14: Plot of Plasticity Index vs. Liquid Limit for Various Soils (from Lambe, 1951)

Samples S1 and D5 are both above A-line, meaning they are on the clay or organic side, rather than silts or organics. For the samples tested, they are around medium to high plasticity boundary, however, for other samples tested in Qglv advance glaciolacustrine clay deposits, as described earlier in Chapter 3, they might be in the range of very low to very high plasticity. Fig. 4.14 also reveals that the tested Oso advance glacial lacustrine clay samples (S1 and D5) almost fell in the range of Boston and Chicago glacial clays as presented by Lambe (1951).

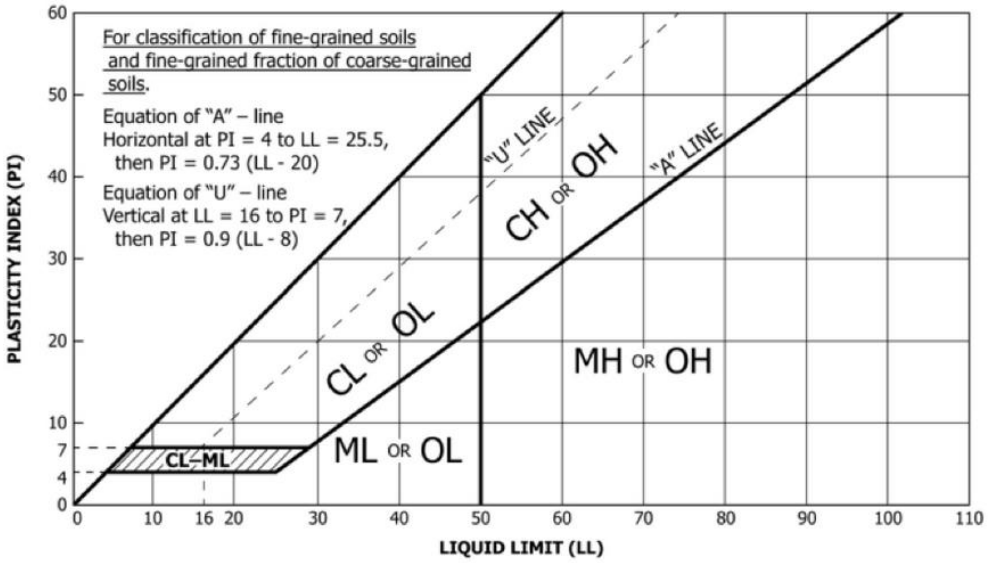

Figure 4.15: Plasticity Chart (from Casagrande, 1948)

The table below shows the interpretation of Casagrande's plasticity chart (Hind, 2017). According to the table, S1 and D5 are in Lean to Fat Clay range, considering their obtained clay contents. Another important outcome shows that they have no or slow dilatancy.

The correction factor for shear strength of normally consolidated soils as a function of the plasticity index was proposed by Skempton (1957). However, Muir Wood (1990) shows that there is appreciable scatter around the given equation for a wider variety of clays. Muir Wood (1983) presents a correlation for undrained shear strength (S_u) based on liquidity index, acceptable accuracy of which was given in Chapter 2. Being more convenient due to its availability through disturbed soil samples, this equation may inevitably allow for the reduction of water content by overconsolidation.

$$\boldsymbol{Su = 170e^{-4.6LI}\ (kPa)\ (Table\ 2.5)}$$

Liquid Limit	Plasticity Index Relative to A-line	Soil Class and Plasticity	Code
Liquid Limit <50% (L)	On or above	**Lean Clay**	CL
		Inorganic clays, sandy clays, silty clays, lean clays. Low to medium plasticity, no or slow dilatancy.	
	Below	**Silt**	ML
		Inorganic silts and very fine sands, rock flour, silty or clayey fine sands. Slight plasticity to non-plastic, slow to rapid dilatancy.	
Liquid Limit >50% (H)	On or above	**Fat Clay**	CH
		Inorganic clays, fat clays. High plasticity, no dilatancy.	
	Below	**Elastic Silt**	MH
		Micaceous or diatomaceous fine sandy and silty soils, elastic silts. Low to medium plasticity, no to slow dilatancy.	
Liquid Limit <30% (L)	Not applicable	**Silty Clay**	CL-ML
Plasticity Index 4 to 7%		Mixed zone where both CL and ML soils plot	

Table 4.6: USCS – Inorganic Fine-Grained Soils Component (from ASTM D2487, ASTM D2488 and Casagrande, 1948)

Equation given below, as described in the literature review chapter, was used to compute the liquidity index of both S1 and D5. An average liquidity index of 0.23 was found by other authors for the advance glaciolacustrine clay in Qglv deposits.

$$\boldsymbol{LI = \frac{w - PL}{LL - PL}}$$

Using the average natural moisture content (30%) presented for the Vashon (Qglv) advance glaciolacustrine clay samples, liquidity indices of 0.22 and 0.24 were found for S1 and D5, respectively. After the equation given by Muir Wood (1983), undrained shear strengths were found as 61.8 kPa (9 psi) for S1, and 56.36 kPa (8.2 psi) for D5. Another equation shown in Table 2.5 by Yang et al. (2006) results in similar results, 66.6 kPa (9.7 psi) for S1, and 61.6 kPa (8.9 psi) for D5.

4.3.5 ONE-DIMENSIONAL CONSOLIDATION TESTS ON REMOLDED SAMPLES

Generally, consolidation tests, as explained earlier, are intended to determine the magnitude and rate of consolidation of the soil if it is laterally restrained and axially drained, while under incrementally applied controlled-stress loading (ASTM2435/D2435M-11). Additionally, for the purposes of this thesis, it was performed to be able to see where all the various sources of data for void ratio of the colluvium/debris flow would plot on the obtained void ratio-vertical effective stress graphs, for an attempt to explain the failure mechanism by the critical state line and the remolded undrained shear strength loss, using their corresponding vertical effective stresses and void ratios from the consolidation test.

4.3.5.1 Equipment

A bench-top mounted loading frame involving a loading beam to be loaded with dead weights was used for the consolidation test (Fig. 4.16a). A consolidometer to hold the specimen in a ring was also used (Fig. 4.16b). The steel ring used, which is stiff enough to prevent significant lateral deformation of the specimen throughout the test, has a height of 0.75” and an inner diameter of 2.5”. Also, as described earlier, porous stones and filter papers were used. For axial deformation readings, an LVDT device was used, which is described later with the data acquisition system. The LVDT is rigidly attached to an external stand, and the travelling stem is attached to the top of the soil specimen.

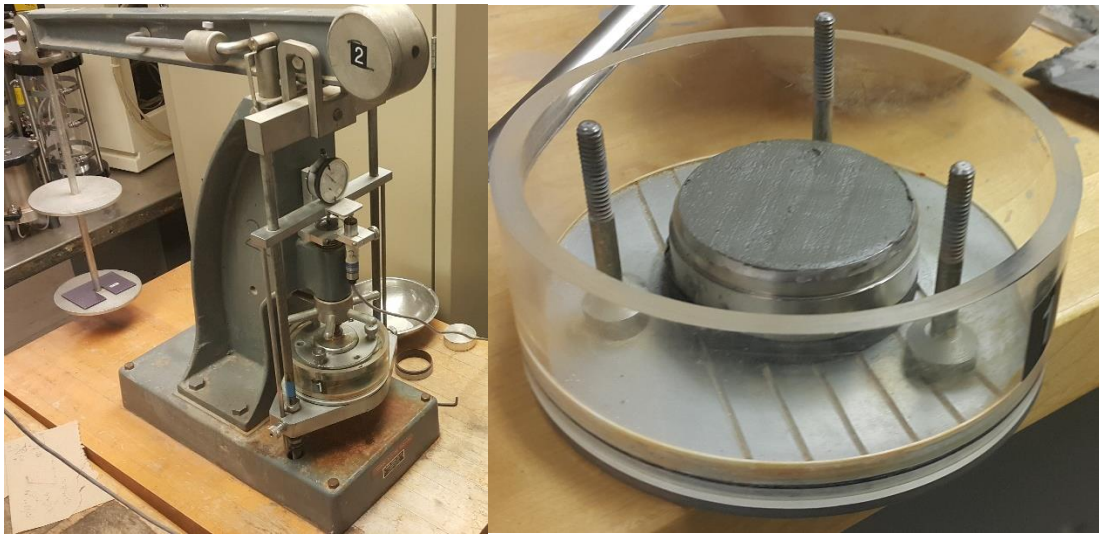

Figure 4.16: (a) Loading Frame, and (b) Consolidometer Used

The stem moves up (or down) due to swelling (or settlement) of the specimen, and this deformation is registered by the LVDT. A loading cap with porous stone was used, as well, on top of the specimen in the consolidation cell.

Vertical Displacement Reading Device (LVDT) and Data Acquisition System

The data acquisition system for the axial deformation reading (LVDT) on the loading frame is shown as a schematic in Fig. 4.17. A DC power supply with 14.2 volts was attached to a network module which was then connected to an Adio-8 module that had 8 channels for sensors. The LVDT was connected to one of these 8 channels. The network module was then connected to the computer which collected the data. TestNet data acquisition software was used to collect the data through each of the loading increments.

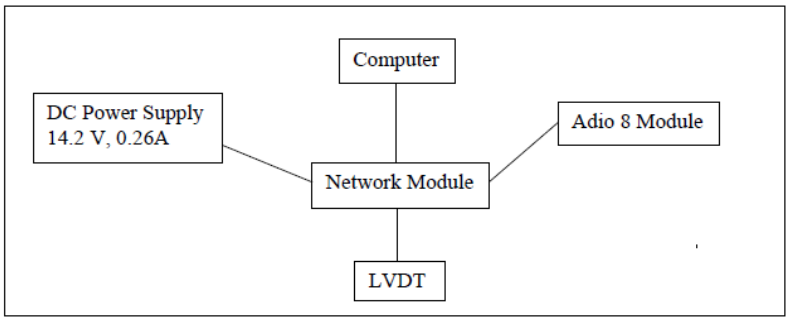

Figure 4.17: Data Acquisition System for Axial Displacement

An HS10 model LVDT with MG1032 serial number from Measurements Group, INC. was used (Fig. 4.18). Serial number also defines the calibration factor (CF) for the particular LVDT, and the desired unit, which is inches here. A signal voltage is measured from the LVDT with each movement (V_s). A zero sensor signal voltage is taken as a reference before the test is performed (V_{s0}). A 10V excitation is applied through the power supply (V_e). Displacement in inches is then calculated as follows:

$$\boldsymbol{D = CF * \left(\frac{Vs - Vs0}{Ve}\right)}$$

The reading schedule used for the axial deformation is given in Table 4.7.

# Reading	Interval (min.)
1	0
599	0.0167
50	1
16	15
38	30
20000	30

Table 4.7: LVDT Reading Schedule

Figure 4.18: LVDT Used during Consolidation Tests

Miscellaneous Equipment

All deaired/distilled water in the required tests mentioned above is drawn from a Humboldt deaerator. The deaerator is placed under a vacuum in which a spinning disk creates a jet to remove all trapped air via the vacuum.

4.3.5.2 Specimen Preparation

To better represent the glaciolacustrine clay in the liquefied colluvium on the slope, and to be able to describe the different behavior, the specimens were remolded at a water content to around their liquid limit (D5), and above the liquid limit (S1). The air-dried samples to be tested for consolidation were soaked in deaired/distilled water for S1, and tap water for D5, for at least 48 hours. They were shaken for 10 minutes on Buffalo vibrating plates before leaving them to wait, in order to remove the excess air in the soil (Fig. 4.19). They were then blenderized using commercial Hamilton Beach mechanical blenders for 10 min (Fig. 4.20). After mixing, they were washed into plasters of Paris dishes lined with filter papers (Fig. 4.21). The dishes help to remove the excess water from the slurry (USACE, 2013).

Figure 4.19: Soaked Sample on Vibrating Plate

Figure 4.20: Samples Blenderized

Figure 4.21: Wicking Out the Excess Water from Samples

4.3.5.3 Methods

One-Dimensional Consolidation tests using incremental loading were performed on the samples, S1 and D5. ASTM D2435/2435M-11 standard test method was followed, and the tests are in general compliance with the ASTM designation. Specimens were prepared as described in 3.4.3. A combination of *Test Method A*, during which a load increment duration of 24 h or multiplies is applied, and *Test Method B*, where the load increments are applied after 100% primary consolidation is reached, and time-deformation readings are required on all load increments was followed. Steps of the procedure are provided as follows:

1. The porous disks were boiled in tap water for at least 10 minutes, and kept in the water, until the temperature of the water has reached to room (laboratory) temperature before testing. Filter papers were saturated in dishes for at least 10 min.
2. The disturbed samples were placed into the rings using spatulas, attention paid while filling, in order to prevent any voids in the ring.
3. The initial wet mass for the specimen, M_{To}, in the consolidation ring was calculated to the nearest 0.01 g by measuring the mass of the ring with the specimen and subtracting the tare mass of the ring, M_r.
4. The initial height of the specimen, H_o, was determined to the nearest 0.01 mm [0.001 in.] based on the thickness of the specimen ring, $H_{r.}$
5. The initial volume of the specimen, V_0, was computed to the nearest 0.01cm^3 [0.01 $in.^3$] from the diameter of the ring and the initial specimen height.
6. Two natural water content determinations of soils were obtained in accordance with ASTM 2216-10.

7. A porous stone was placed on the consolidometer ground, followed upwards by a filter paper, the ring with soil inside, another filter paper on top of the soil, and finally the loading cap with another porous stone.
8. A seating load resulting in a total axial stress of 125 psf was applied for sample S1, and an approximate seating stress of 75 psf was applied for the D5. The specimens in the consolidometer were inundated to eliminate the air-water interface at the soil boundary and prevent immediate water content changes of the specimen due to lateral drainage.
9. A load increment ratio (LIR) of 2 was used, which involved loading with 125 psf, 250 psf, 500 psf, 1000 psf, 2000 psf, 4000 psf, and 8000 psf for S1, and up to 16000 psf for D5. In general, the load increments were applied after 24h, but longer intervals for particular increments, which are discussed later, were selected in order to identify the effects of secondary consolidation.
10. Unloading was applied by one-fourth as large as the preceding stress level, and the ultimate stress (seating stress) for both samples was 125 psf.
11. During loading and unloading for both samples, LVDT readings were taken, and recorded to spreadsheets, using the reading schedule in Table 4.7. This system is capable of recording the initial and final deformations, as recommended by the standard.
12. The specimens and the rings were removed from the consolidometer after the tests, and the final total mass of the specimen, M_{tf} to the nearest 0.01 g, by measuring the soil plus the ring and then subtracting the ring tare mass.
13. The height of the specimen, H_{et}, was measured to the nearest 0.001 mm [0.001 in.] by taking the average of at least four evenly spaced measurements over the top and bottom surfaces.

14. In order to determine the specimen dry mass and the water content, the entire specimen was dried in accordance with ASTM 2216-10.

Figs. 4.22 and 4.23 show a combination of schematics for the performed consolidation tests.

Figure 4.22: Specimens Before and After Consolidation Test

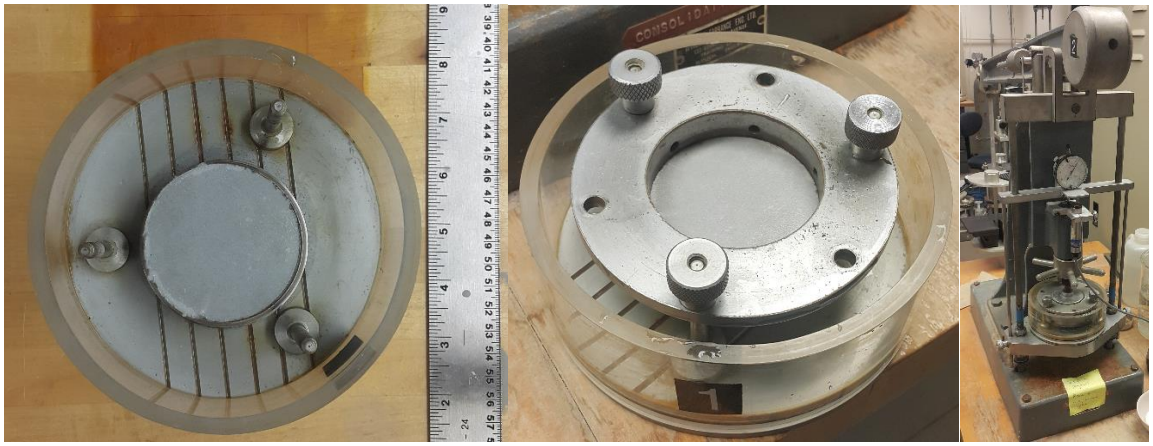

Figure 4.23: Specimens in Consolidometer and Consolidation Loading Frame

4.3.5.4 Sources of Error in One-Dimensional Consolidation Tests

Extruded Soil

With very soft, highly plastic clays, a considerable amount of soil is sometimes extruded between the loading cap and the ring. When the test is dismantled, the soil extruded should be scraped, oven dried and weighed together. The soil volume can be

estimated from the average void ratio and appropriate correction can be made. The errors are probably not important as long as the extruded amount of soil is only a small percentage of the total soil sample volume.

Trimming Problems

If the soil volume at the start of a test is supposed to be equal to the consolidation ring volume but the sample was incorrectly trimmed on the flat surfaces, then the initial void ratio is erroneous. Typically, a 0.002-inch trimming error results in a void ratio error of about 0.01. A zone of soil with relatively low hydraulic conductivity may be formed near the flat faces of the disc-shaped sample, if the soil sample surface is remolded by smearing the surface with the trimming tool. These thin layers of disturbed material increase the drainage time and underestimate the consolidation coefficient. The problem is minimized by cleanly trimming instead of chopping the surface.

Apparatus Deflection Errors:

If the deflection of the machine differs from the values used to reduce data, there will be errors. The deflections of the machine are normally determined in a matter of a few minutes with the two sheets of filter paper (used to protect the porous stones against encroachment) in the device. The filter paper gradually consolidates, and the usual process can result in machine deflections being underestimated at higher loads. This is not a problem with relatively compressible soils, which move very widely at high pressures, but may have problems with very hard, or stiff soils, which are not very deformed even at greater loads.

Error in Assuming the Soil is Saturated

If the final saturation degree is not 100 %, an error can be made in the calculation of the void ratios. An error in estimating the saturation level of 2 percent could lead to a 0.03 error in the calculated void ratio.

Error in Estimating the Specific Gravity of Solids

An error in the estimation of the specific gravity of solids might typically cause an error of about 0.03 in the calculated void ratio.

Ring Friction

The data reduction assumes that no loads on the soil sample are transferred to the consolidation ring by friction between the soil and the ring. If there is friction, then the stress in the top of the soil sample is higher than the stress in the bottom of the sample and, overall, it is less than expected. The best way to minimize ring friction is to use consolidation rings made of hard metals with polished surfaces. In addition, high specimen diameter to specimen thickness ratios minimize ring friction effects. The ring friction may not be significant except in the unloading section where large amounts of friction between the soil and the ring can be "locked."

4.3.5.5 Test Results

A steel ring with 0.75” height and 2.5” diameter was used in the oedometer described earlier. Starting with 125 psf seating load for S1, and 75 psf for D5, the samples were incrementally loaded up to 8000 psf, and to 16000 psf, respectively. The load was doubled after each successive loading, generally right after 24h. For S1, with an attempt to better indicate the secondary consolidation, 250 psf and 500 psf loading increments were

done approximately in 72h. For D5, the increments were around 30h duration for the lower loadings, while 50h duration was valid for the 8000 psf loading.

Axial strain, %, was calculated using the change in specimen height, ΔH, as follows:

$$\Delta H = d - d0 - da$$

where, d is the deformation reading at various times in test, d_0 is the initial deformation reading, and d_a is the apparatus deformation correction, which is discussed later in sources of error section. All the deformation readings are in length unit.

$$\varepsilon = \frac{\Delta H}{H0} * 100$$

where, ε is the axial strain in percent, ΔH is the change in specimen height, and H_0 is the initial specimen height, both in length unit.

Agreeing both by direct measurement, and by using the equation below, the dry mass of total specimens was calculated.

$$Md = \frac{MTf}{1 + wf}$$

where M_d is the dry mass of total specimen (g), M_{Tf} is the moist mass of total specimen after test (g), and w_f is the water content of entire specimen after test in decimal form.

Initial and final water content of the specimens, in percent, were calculated as follows:

$$w0 = \frac{MT0 - Md}{Md} * 100$$

$$\boldsymbol{wf = \frac{MTf - Md}{Md} * 100}$$

where; w_0 is the initial water content (%), M_{T0} is the moist mass of the specimen before test (g), and w_f is the final water content (%).

Initial dry density of the specimens was calculated as follows:

$$\boldsymbol{\rho d = \frac{Md}{V0}}$$

where V_0 is the initial volume of specimen, calculated by computing the volume of the ring.

Volume of solids was computed as:

$$\boldsymbol{Vs = \frac{Md}{G\rho w}}$$

where V_s is the volume of solids in cm^3, G is the specific gravity of the solids, which was 2.77 for our samples, as explained in earlier, and ρ_w is the density of water filling the pore space in g/cm^3 (0.9982 g/cm^3 was used). Using the calculated volume of solids, the equivalent height of solids was defined by the following equation:

$$\boldsymbol{Hs = \frac{Vs}{A}}$$

where H_s is the height of solids in cm, and A is the cross-sectional specimen area in the ring (cm^3).

Void ratios were calculated using following equations:

$$\boldsymbol{e0 = \frac{H0 - Hs}{Hs}}$$

$$\boldsymbol{ef = \frac{Hf - Hs}{Hs}}$$

where e_0 and e_f are the initial and the final void ratios, respectively, and H_f is the final specimen height in cm.

4.3.5.5.1 Test Results for S1

The specimen was prepared at a water content above its liquid limit. After calculating the corresponding axial strain for loading and unloading, following figure shows the obtained values against time. In the same manner, Fig. 4.25 plots void ratio vs. time. The obtained results are presented in Table 4.8. e_{f1} is the corresponding value for the final void ratio after 8000 psf loading, and e_{f2} is the void ratio after the unloading of 125 psf was complete.

D_r (cm)	6.35
H_0 (cm)	1.91
M_{T0} (g)	99.70
M_{Tf} (g)	83.23
M_d (g)	61.73
w_0 (%)	61.5
w_f (%)	34.8
ρ_d (kN/m^3)	10.03
V_s (cm^3)	22.33
H_s (cm)	0.70
e_0	1.70
e_{f1}	0.82
e_{f2}	0.90

Table 4.8: Consolidation Calculation Results for S1

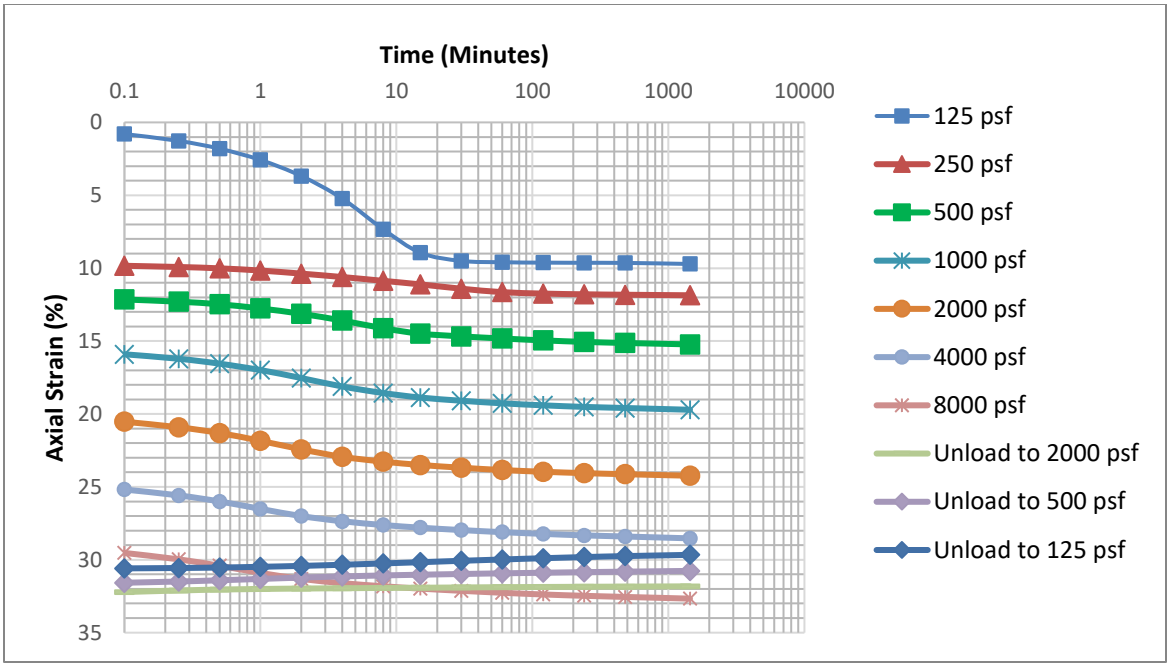

Figure 4.24: Time-Deformation Curves in Log-Scale for S1

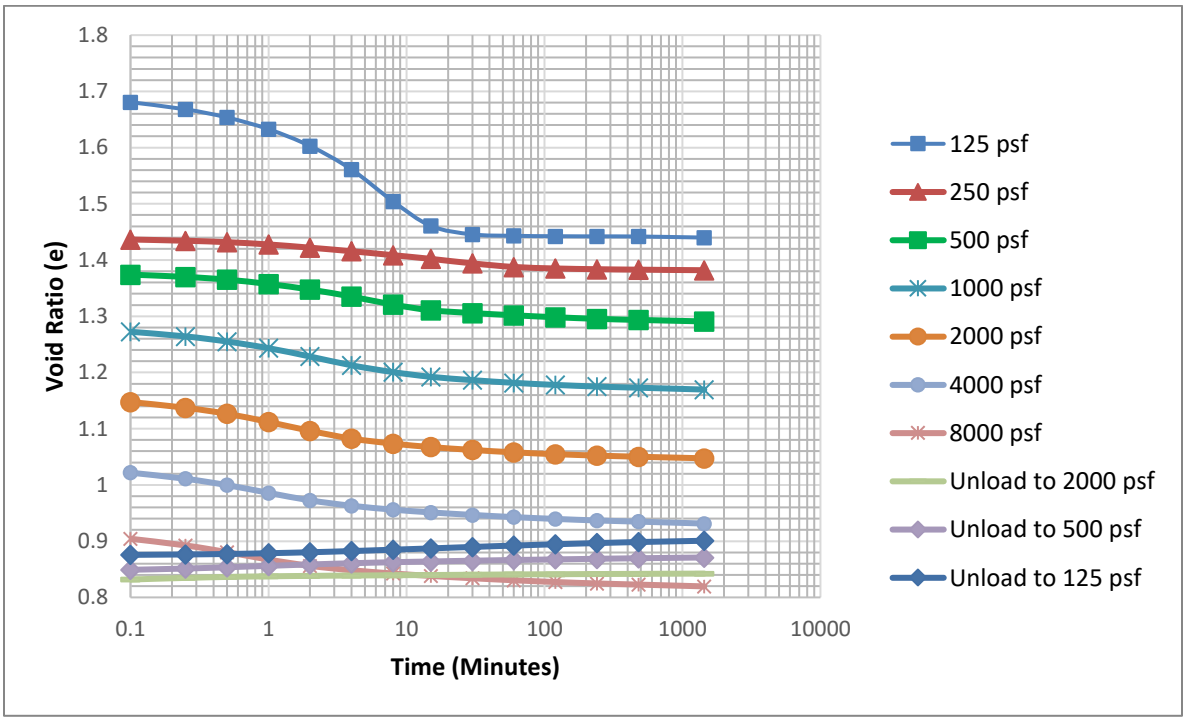

Figure 4.25: Time-Void Ratio Curves in Log-Scale for S1

4.3.5.5.2 Test Results for D5

The specimen was prepared at around its liquid limit. For D5 specimen, instead of a 125 psf seating pressure, 75 psf was used, and it was loaded up to an equivalent of 16000 psf stress, instead of 8000 psf. Also, the specimen was prepared and inundated in the consolidometer using tap water, as opposed to deaired/distilled water used for the S1 specimen. The time vs. void ratio and deformation curves are given below. Table 4.9 presents the obtained results. e_{f1} is the corresponding value for the final void ratio after 16000 psf loading, and e_{f2} is the void ratio after the unloading of 250 psf was complete.

D_r (cm)	6.35
H_0 (cm)	1.91
M_{T0} (g)	106.15
M_{Tf} (g)	91.58
M_d (g)	70.81
w_0 (%)	49.9
w_f (%)	29.3
ρ_d (kN/m^3)	11.51
V_s (cm^3)	25.61
H_s (cm)	0.81
e_0	1.36
e_{f1}	0.65
e_{f2}	0.76

Table 4.9: Consolidation Calculation Results for D5

Figures below show the consolidation curves against time.

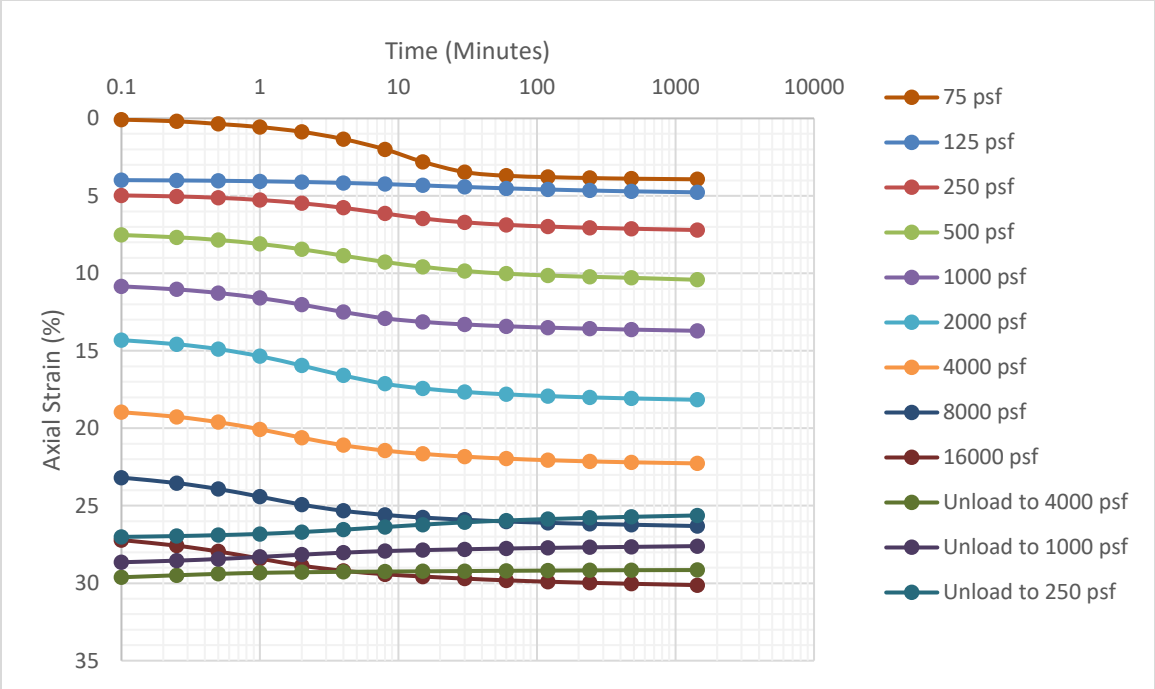

Figure 4.26: Time-Deformation Curves in Log-Scale for D5

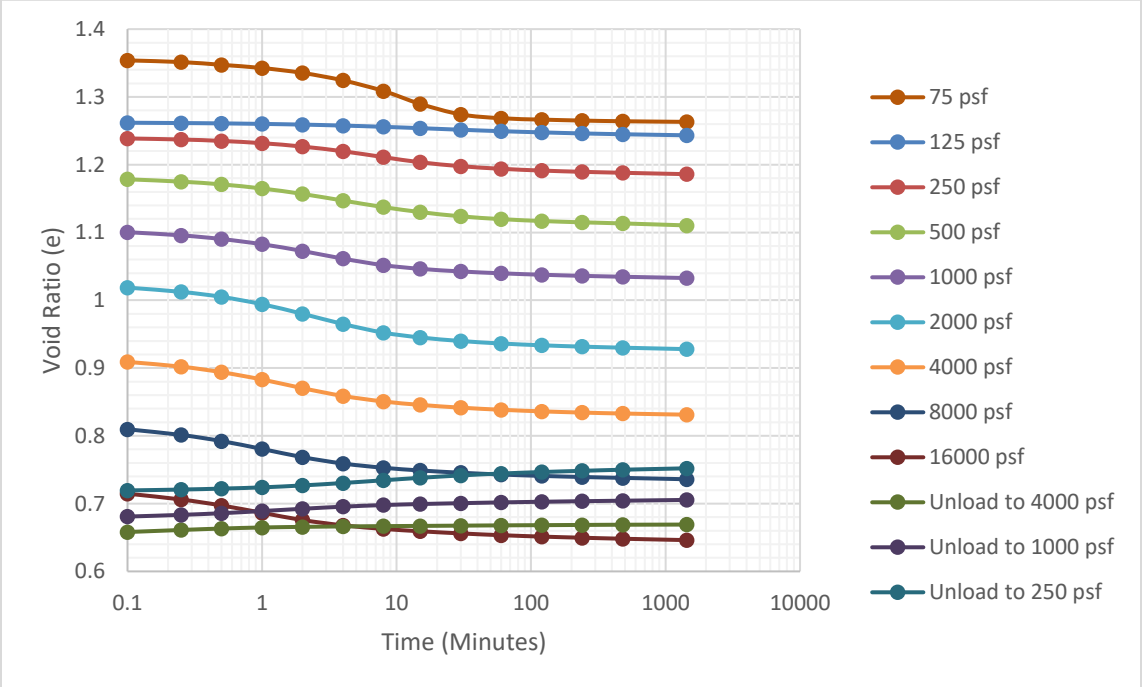

Figure 4.27: Time-Void Ratio Curves in Log-Scale for D5

4.3.5.6 Pre-Analysis of the Test Results

Axial strain vs. time plots were used to determine the coefficient of consolidation (c_v), by the logarithm of time method and the square root of time method. Coefficient of compressibility (α_v), and the hydraulic conductivity (k) were also computed for various loading stages. Pre-consolidation stresses for the samples were found from Casagrande Method by plotting axial strain (%) vs. axial effective stress (psf).

For each incremental pressure, the coefficient of consolidation, c_v was found using the log of time, and the square root of time methods. Coefficient of compression, α_v, and hydraulic conductivity, κ, were also determined. Figs. 4.28 and 4.29 illustrate an example of the procedure needed to get c_v for the S1 clay specimen subjected to vertical stress of 500 psf.

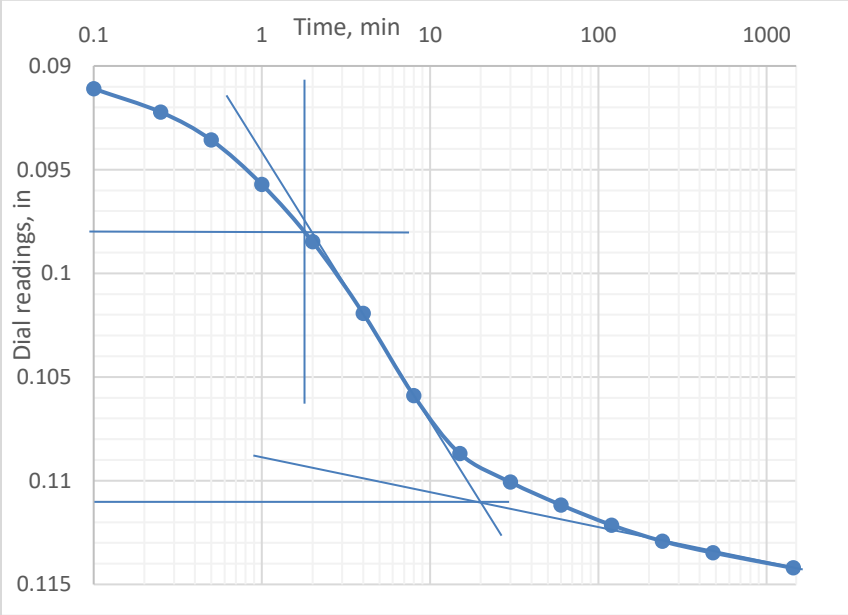

t_2	2	min
s_2	0.1019	in
t_1	0.5	min
s_1	0.0936	in
Δs	0.0084	in
s_0	0.0852	in
s_{100}	0.111	in
s_{50}	0.0981	in
t_{50}	1.8	min
c_v	0.0115	in^2/min
c_v	0.1147	ft^2/day

Figure 4.28: Log of Time Method for S1 Specimen Under 500 psf Vertical Stress

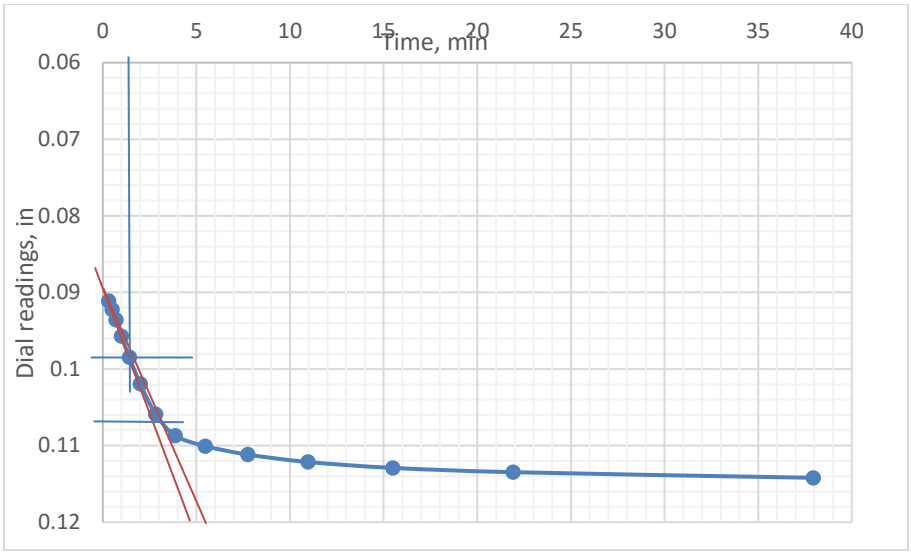

s_0	0.09	in
s_{100}	0.1089	in
s_{50}	0.0981	in
s_{90}	0.107	in
t_{45}	1.4	min
c_v	0.0119	in^2/min
c_v	0.1189	ft^2/day

Figure 4.29: Square Root of Time Method for S1 Specimen Under 500 psf Vertical Stress

Fig. 4.30 illustrates the soil body diagrams at initial condition, and after loading. Since all the change in the volume of the soil will be in the void space after loading, the change in volume will be equal to the change in void ratio, Δe. Then, under one-dimensional compression, the change must come only from vertical compression. Therefore, the axial strain, ε, equals to change in length of the soil element, Δ*l*, divided by the original length, l_0, or Δe over $(1+e_0)$. Thus, the consolidation curve can be plotted either strain vs. logσ′, or void ratio vs. logσ′.

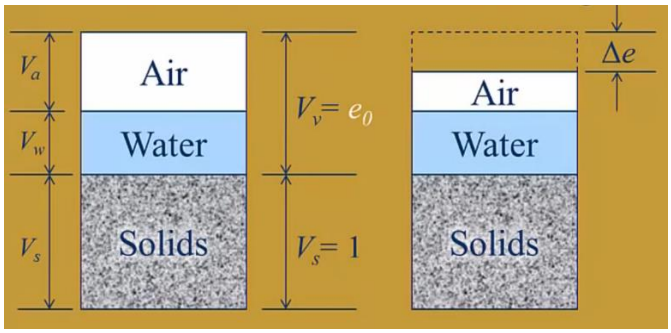

Figure 4.30: Diagrams Showing Soil Body at Initial Condition (left) and After Loading (right)

In addition to the equations given for the axial strain and void ratio calculations presented earlier, the change in void ratio can also be computed as:

$$\Delta \boldsymbol{e} = \boldsymbol{\varepsilon} * (\mathbf{1} + \boldsymbol{e0}) = \frac{\Delta \boldsymbol{H}}{\boldsymbol{H0}} * (\mathbf{1} + \boldsymbol{e0})$$

The void ratio at any effective stress is:

$$\boldsymbol{e} = \boldsymbol{e0} - \Delta \boldsymbol{e}$$

The parameter used to calculate the consolidation rate is called the consolidation coefficient, c_v, and is defined as follows:

$$\boldsymbol{cv} = \frac{\boldsymbol{k}}{\boldsymbol{mv}.\boldsymbol{\gamma w}} = \frac{\boldsymbol{k} * (\mathbf{1} + \boldsymbol{e0})}{\boldsymbol{av}.\boldsymbol{\gamma w}}$$

where *k* is the hydraulic conductivity from Darcy's Law, and m_v and α_v are the coefficients of compressibility defined as:

$$\boldsymbol{mv} = \frac{\boldsymbol{d\varepsilon}}{\boldsymbol{d\sigma'}}$$

$$\boldsymbol{av} = -\frac{\boldsymbol{de}}{\boldsymbol{d\sigma'}}$$

where d_ε and d_e are small changes in vertical strain and void ratio, respectively, resulting from a small effective stress increment, $d_{\sigma'}$.

The coefficient of consolidation is used to compute the rate of settlement from the expression:

$$\boldsymbol{Ti} = \frac{\boldsymbol{cv} * \boldsymbol{ti}}{\boldsymbol{Hdr^2}}$$

where T_i is the time factor and t_i is time for corresponding settlement, and H_{dr} is the drainage path length (T_{50}=0.197, T_{45}=0.159). Since the consolidation specimens were double drained:

$$\boldsymbol{Hdr = \frac{H}{2}}$$

where H is the specimen thickness under corresponding pressure.

The following results have been obtained for S1 using the given equations and graphical methods:

125 psf Consolidation			250 psf Consolidation			500 psf Consolidation		
αv	1.93E-03	ft^2/lb	αv	4.37E-04	ft^2/lb	αv	3.33E-04	ft^2/lb
k	1.11E-06	cm/s	k	4.28E-07	cm/s	k	3.48E-07	cm/s
$c_{v(1)}$	7.11E-02	ft^2/day	$c_{v(1)}$	1.10E-01	ft^2/day	$c_{v(1)}$	1.15E-01	ft^2/day
$c_{v(2)}$	8.36E-02	ft^2/day	$c_{v(2)}$	1.18E-01	ft^2/day	$c_{v(2)}$	1.19E-01	ft^2/day
1000 psf Consolidation			2000 psf Consolidation			4000 psf Consolidation		
αv	2.06E-04	ft^2/lb	αv	1.00E-04	ft^2/lb	αv	4.53E-05	ft^2/lb
k	2.62E-07	cm/s	k	1.69E-07	cm/s	k	1.20E-07	cm/s
$c_{v(1)}$	1.34E-01	ft^2/day	$c_{v(1)}$	1.67E-01	ft^2/day	$c_{v(1)}$	2.47E-01	ft^2/day
$c_{v(2)}$	1.37E-01	ft^2/day	$c_{v(2)}$	1.68E-01	ft^2/day	$c_{v(2)}$	2.39E-01	ft^2/day
			8000 psf Consolidation					
			αv	2.12E-05	ft^2/lb			
			k	5.28E-08	cm/s			
			$c_{v(1)}$	2.19E-01	ft^2/day			
			$c_{v(2)}$	2.12E-01	ft^2/day			

Table 4.10: Results from One-Dimensional Consolidation Test for the S1 Dataset

Note that, in the corresponding table, $c_{v(1)}$ is the coefficient of consolidation obtained through the logarithm of time method, using T_{50}, while $c_{v(2)}$ is the same coefficient obtained by the square root of time method, using T_{45}.

Fig. 4.31 illustrates the coefficient of consolidation, c_v in ft^2/day, against the void ratios during loading under various stresses.

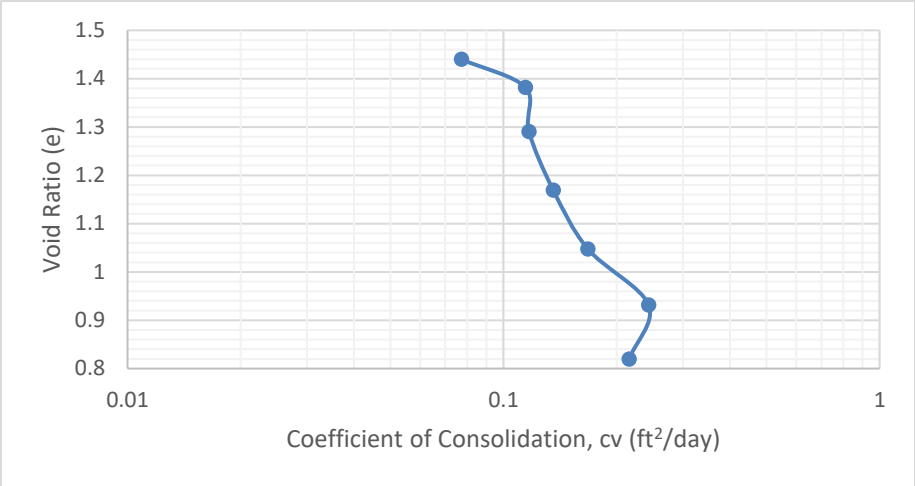

Figure 4.31: Void Ratio vs. Coefficient of Consolidation Curve for S1

The figure below presents the consolidation curve for S1 in void ratio manner.

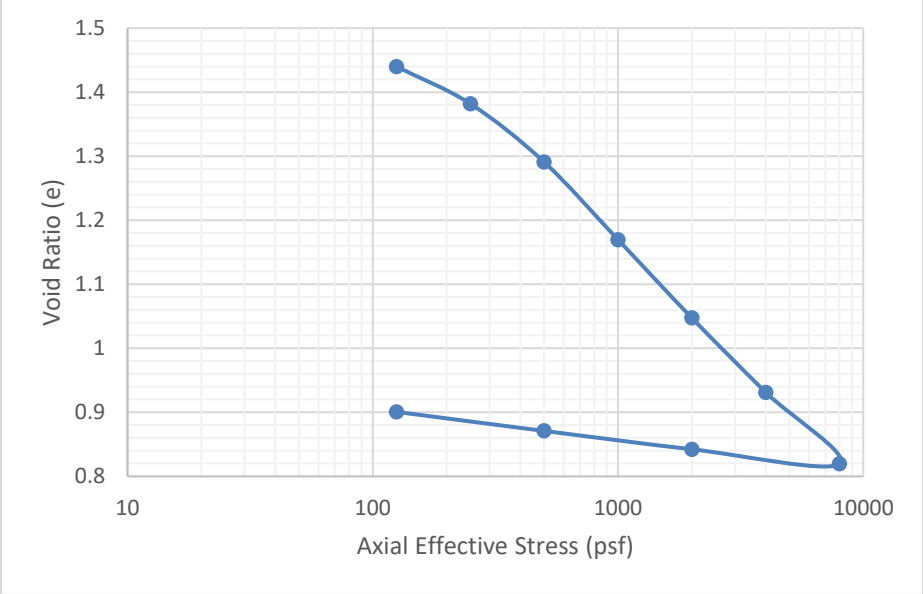

Figure 4.32: Void Ratio vs. Axial Effective Stress Plotted for End of Increments for S1

The following results in Table 4.11 have been obtained for D5 using the given equations and graphical methods. Fig. 4.33 represents the coefficient of consolidation, c_v in ft^2/day, against the void ratios during loading under various stresses.

75 psf Consolidation			125 psf Consolidation			250 psf Consolidation		
αv	1.21E-03	ft^2/lb	αv	3.78E-04	ft^2/lb	αv	4.24E-04	ft^2/lb
k	5.92E-07	cm/s	k	3.67E-07	cm/s	k	3.13E-07	cm/s
$c_{v(1)}$	5.32E-02	ft^2/day	$c_{v(1)}$	1.01E-01	ft^2/day	$c_{v(1)}$	7.63E-02	ft^2/day
$c_{v(2)}$	7.16E-02	ft^2/day	$c_{v(2)}$	1.02E-01	ft^2/day	$c_{v(2)}$	8.96E-02	ft^2/day
500 psf Consolidation			1000 psf Consolidation			2000 psf Consolidation		
αv	2.72E-04	ft^2/lb	αv	1.35E-04	ft^2/lb	αv	9.07E-05	ft^2/lb
k	2.83E-07	cm/s	k	1.86E-07	cm/s	k	1.18E-07	cm/s
$c_{v(1)}$	1.04E-01	ft^2/day	$c_{v(1)}$	1.33E-01	ft^2/day	$c_{v(1)}$	1.21E-01	ft^2/day
$c_{v(2)}$	1.16E-01	ft^2/day	$c_{v(2)}$	1.32E-01	ft^2/day	$c_{v(2)}$	1.31E-01	ft^2/day
4000 psf Consolidation			8000 psf Consolidation			16000 psf Consolidation		
αv	3.89E-05	ft^2/lb	αv	1.84E-05	ft^2/lb	αv	8.57E-06	ft^2/lb
k	7.71E-08	cm/s	k	3.46E-08	cm/s	k	1.70E-08	cm/s
$c_{v(1)}$	1.75E-01	ft^2/day	$c_{v(1)}$	1.57E-01	ft^2/day	$c_{v(1)}$	1.57E-01	ft^2/day
$c_{v(2)}$	1.76E-01	ft^2/day	$c_{v(2)}$	1.58E-01	ft^2/day	$c_{v(2)}$	1.63E-01	ft^2/day

Table 4.11: Results from One-Dimensional Consolidation Test for the D5 Dataset

Note that, in the corresponding table, $c_{v(1)}$ is the coefficient of consolidation obtained through the logarithm of time method, using T_{50}, while $c_{v(2)}$ is the same coefficient obtained by the square root of time method, using T_{45}.

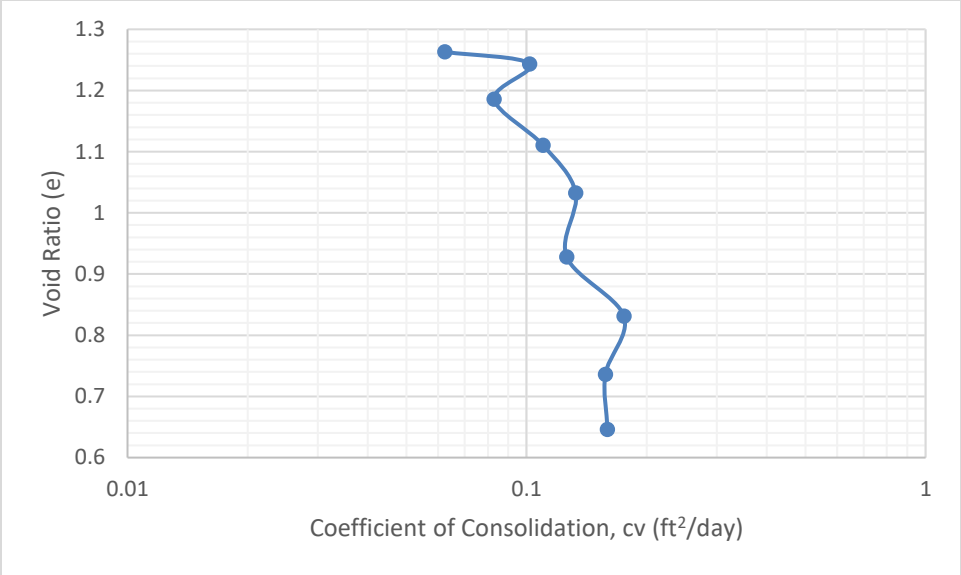

Figure 4.33: Void Ratio vs. Coefficient of Consolidation Curve for D5

Below is the figure illustrating the consolidation curve for D5.

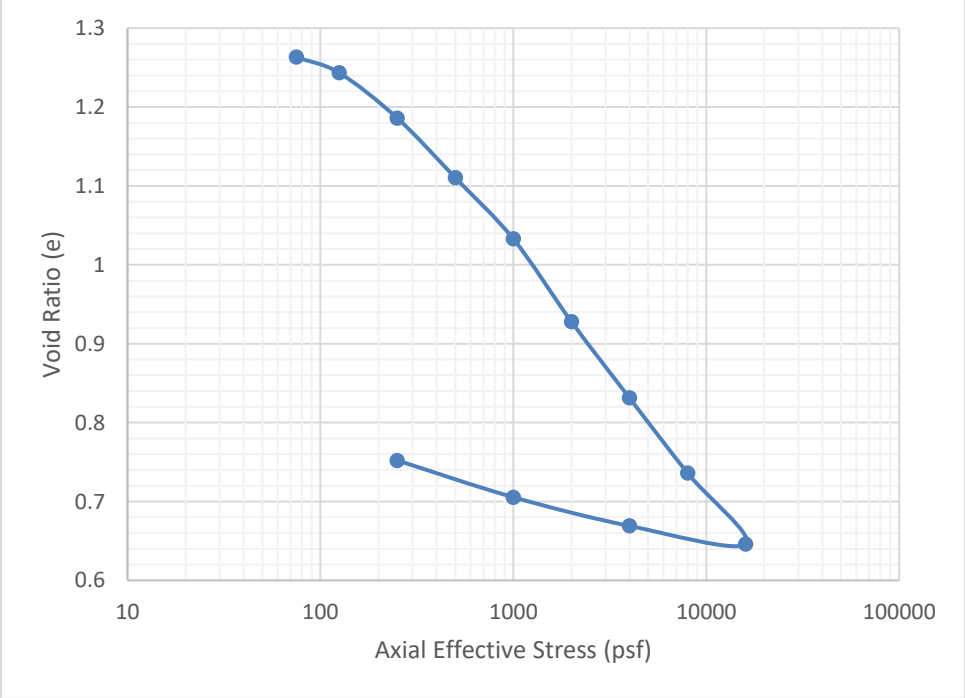

Figure 4.34: Void Ratio vs. Axial Effective Stress Plotted for End of Increments for D5

4.3.5.7 Determining the Pre-Consolidation Stress

Fig. 4.35 presents Casagrande Method to determine the pre-consolidation pressure for S1. As a result, determined pre-consolidation stress for S1 advance glaciolacustrine clay sample is approximately 260 psf (12.5 kPa).

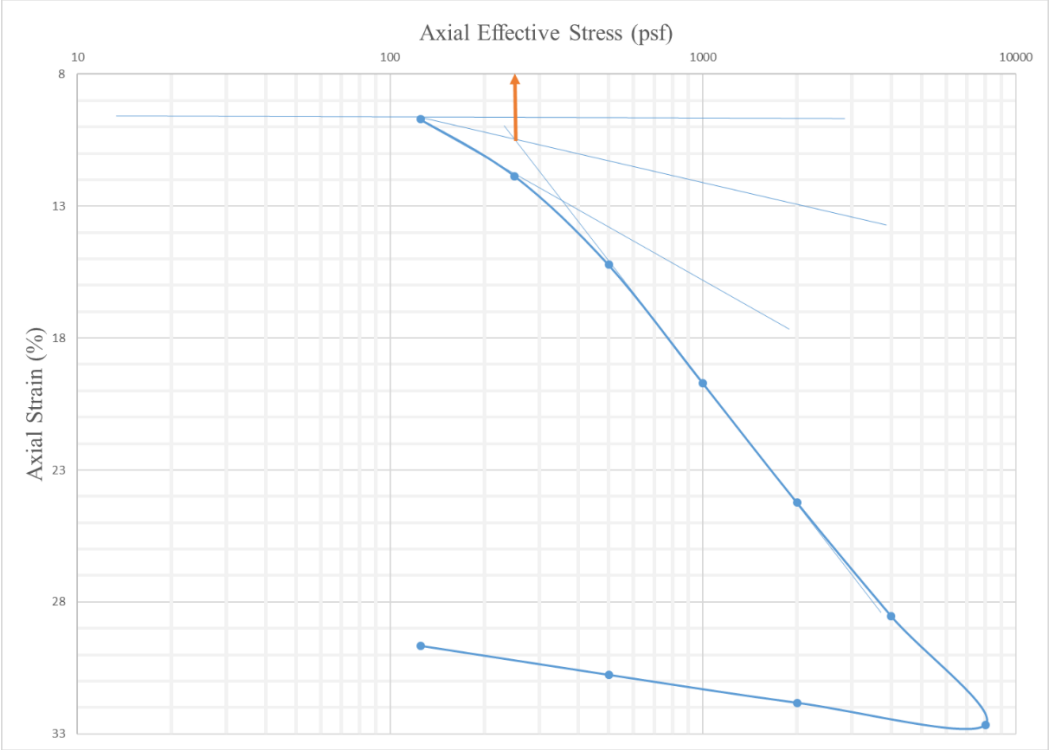

Figure 4.35: Evaluation of Pre-Consolidation Stress for S1 from Casagrande Method

Fig. 4.36 presents Casagrande Method to determine the pre-consolidation pressure for D5. As a result, determined pre-consolidation stress for D5 advance glaciolacustrine clay sample is approximately 230 psf (11 kPa).

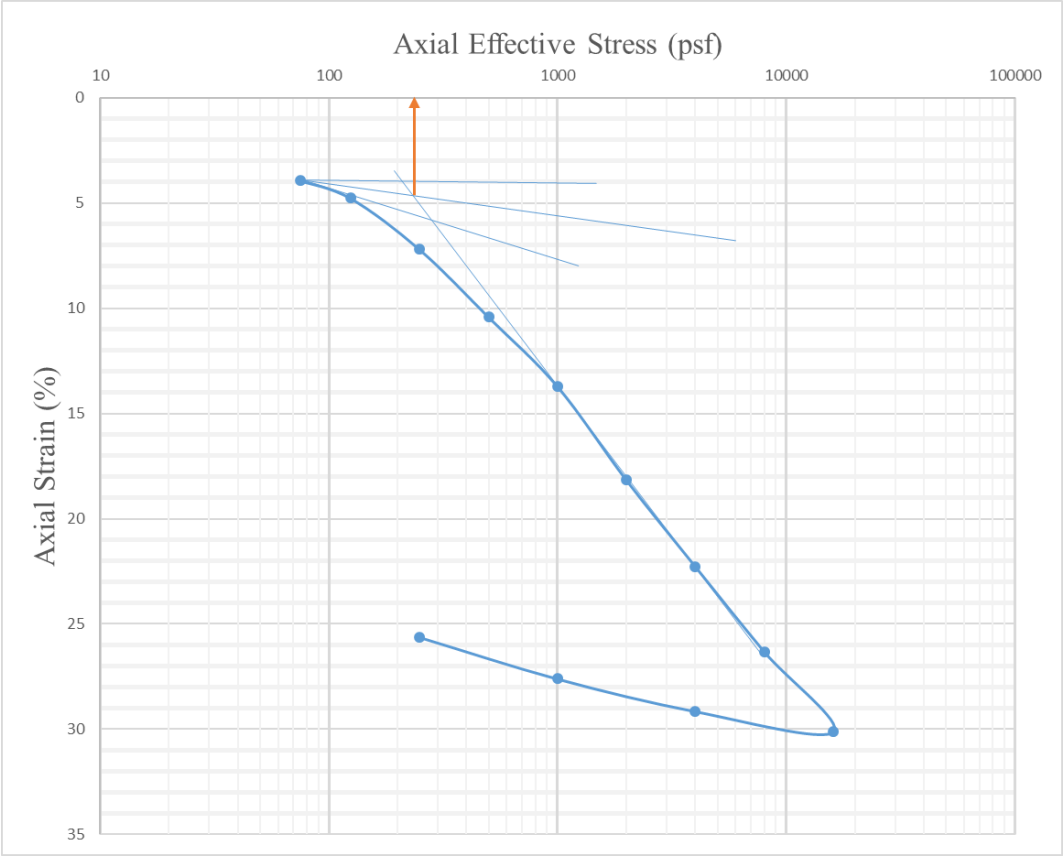

Figure 4.36: Evaluation of Pre-Consolidation Stress for D5 from Casagrande Method

Obtained pre-consolidation stresses represents approximately 2 to 4 ft (0.6 - 1.2 m) of overburden.

4.4 Analysis of the Findings

After the run-out and colluvium volume comparison, the outcome meant that the landslide terminus has been reached with other materials with the colluvium that could include previously in-place outwash, lacustrine, till deposits and/or sediments in riverbed.

Stark et al. (2017) presented the table below for the input parameters they used for limit equilibrium slope stability analyses. The method on how they obtained the total and saturated unit weights is vague, when their case study is examined.

Geologic deposit	Total and saturated unit weights (kN/m^3)	Effective stress friction angle or range of friction angle for stress-dependent strength envelope		
		Estimated peak (degrees)	Measured fully softened (degrees)	Measured residual (degrees)
Recessional outwash	20.0	28	—	—
Glacial till	20.0	35	—	—
Advanced outwash	19.0	30	—	—
Low-plasticity advanced glaciolacustrine	20.0	—	25–34	20–27
High-plasticity advanced glaciolacustrine	20.0	—	21–32	12–19
Sands and gravels	19.0	35	—	—
Prior slide debris (colluvium)	16.5	—	21–32	12–19

Table 4.12: Input Parameters for Limit Equilibrium Slope Stability Analyses (from Stark et al., 2017)

When the given saturated unit weight of 16.5 kN/m^3 is used to obtain a void ratio:

$$\boldsymbol{\gamma sat = \frac{\gamma w(Gs + e)}{1 + e}}$$

assuming fully saturated (S=1), and using specific gravity of 2.77, a void ratio of 1.6 is reached. Similarly:

$$\boldsymbol{wc = \frac{eS}{Gs}}$$

yields to a water content of 57.6%.

Iverson et al. (2015), based on their measurements of eight core samples used a bulk density of 2000 kg/m^3 (19.61 kN/m^3), initial sediment porosity of 0.38, and static critical-state sediment porosity of 0.36 for their numerical simulations. Using the porosity values:

$$\boldsymbol{e = \frac{n}{1 - n}}$$

results in void ratios of 0.61 and 0.56, respectively, for the given porosities, which would result in water contents of 22.02% and 20.22%, respectively. Using the bulk density given, a void ratio of 0.77, and water content of 27.84% is obtained.

Similarly, when Table 4.1 is observed, Oso Qglv deposits would have an average bulk density of 1966.67 kg/m^3 (19.3 kN/m^3) from three studies, resulting in similar natural water content and void ratio of Iverson et al. (2015).

Pyles et al. (2016) also estimated the soil unit weights, based on the soil descriptions and field tests (e.g. blow numbers) delineated on the field logs and laboratory measurements of soil density of the samples selected. They obtained the unit weight as 2002.31 kg/m^3 (19.64 kN/m^3) for lacustrine deposits, and 1842.12 kg/m^3 (18.1kN/m^3) for the earlier slide debris. These results would yield void ratios of 0.77 and 1.10, and water contents of 27.69% and 39.83%, respectively.

Keaton et al. (2014) also reported that four samples of lacustrine clays from these borings contained natural water content ranging from 27% to 31%, plastic limits from 23% to 27%, liquid limits from 44% to 56%, and shear strength from about 1 to 2 tons per square foot (100 to 200 kPa) (Thorsen, 1969). Table below represents the Atterberg limit testing results Keeton et al. (2014) provided.

Atterberg Limits					
Sample ID	PL (%)	LL (%)	PI (%)	Natural Water Content (%)	Comments
1A	31	75	44	41	
1B	27	60	33	87	
2A	26	55	29	24	
2B (HA-11)		-		16	Non-plastic
3A	26	28	2	33	Non-plastic
HA-2 (4.5-5.0 ft)	20	38	18	21	
HA-3 (1-3 ft)	29	43	15	30	
HA-4 (6-7 ft)	25	46	21	27	
HA-5 (7-7.5 ft)	28	36	8	29	Non-plastic
HA-6 (9.5-10 ft)	19	25	6	20	Non-plastic
HA-6 (12-12.5 ft)	21	44	24	20	
HA-7 (1 ft)		-		20	
JW-2	27	58	31	53	
JW-3	19	21	2	21	Non-plastic
JW-4	26	62	36	21	Top of Lacustrine

Table 4.13: Summary of Atterberg Limit Testing for the Obtained Material Passing No. 40 Sieve (from Keeton et al., 2014)

Therefore, there is a conflict between all the other available study and Stark et al. (2017), considering the saturated unit weight used, resulting in different void ratios and water contents. This might be made clear if the term “colluvium”, proposed by Stark et al. (2017), was known to certain extent to be able to describe the material, and understand the different failure mechanism hypotheses presented. Although their data seems more consistent with the normally consolidated, remolded glaciolacustrine clay, it does not seem to be supported by the available data. Galster and Laprade (1991) provided wet densities between 1600 (15.69 kN/m^3) and 1920 kg/m^3 (18.83 kN/m^3) for the glaciolacustrine clay but did not provide the source of obtaining these results either, as Savage et al. (2000) proposed.

Figure 4.37 shows void ratio against vertical effective stress for the conducted and collected test results in the same plot, to better identify the samples compared to each other. Unless noted else in the legend, they were the data for glaciolacustrine deposits. If researchers provided different data with the glaciolacustrine deposits, both were included, by noting both in the legend. It should be noted that S1 was remolded at a water content (w_c = 61.5%), higher than its liquid limit (LL = 48%), and D5 (w_c = 49.9%) at around its liquid limit (LL = 49%), to better represent the in-place material at failure. Using their initial water contents before the consolidation tests in the liquidity relationship given, S1 would have a liquidity index, LI = 1.59, and D5 as LI = 1.04, which might make them susceptible to liquefaction.

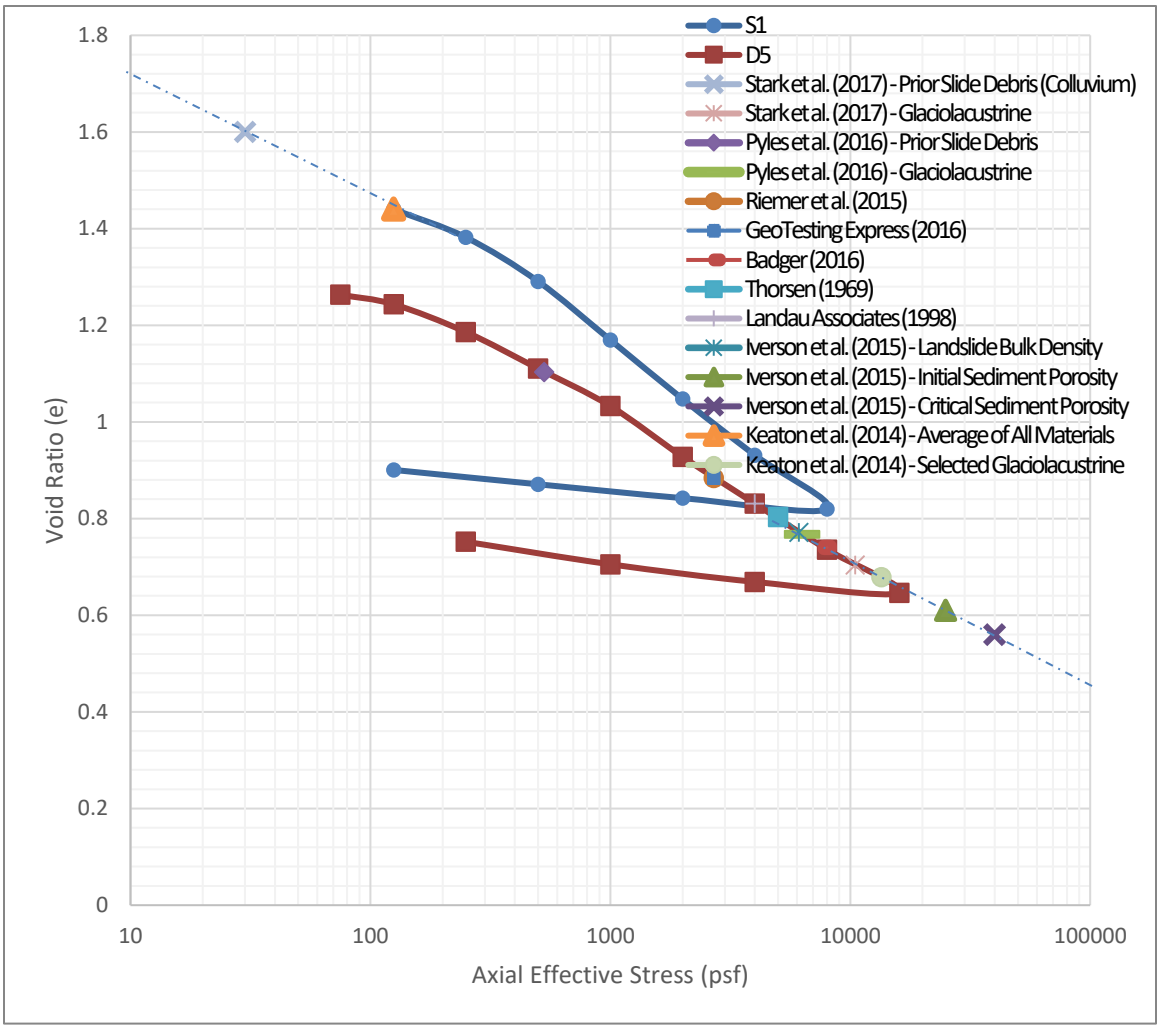

Figure 4.37: Void Ratio vs. Axial Effective Stress Plot for the Two Tested Samples

As can be seen from the figure, many of the collected data agree with the obtained test results. However, the corresponding void ratio for the unit weight proposed by Stark et al. (2017) for the colluvium, would only be possible under very low vertical effective stress (ca. 25 psf = 1.2 kPa), high liquidity index, and high water content. At the end of the first pressure increment of 125 psf (=5.99 kPa) for S1, its initial void ratio, e_0 = 1.70, at 61.5% water content, reduced to 1.43. The prior slide debris (colluvium) unit weight

provided by Pyles et al. (2016), on the other hand, agrees with the obtained test results for the advance glaciolacustrine clay, as well as their unit weight given for glaciolacustrine deposits.

Also, data from Keaton et al. including all materials tested does barely agree with the test results. If only the materials with properties that are closer to advance glaciolacustrine clay are chosen (HA-2 to HA-6), which is indicated as “selected glaciolacustrine” in the figure, it also agrees with the test results.

CHAPTER 5: INVESTIGATING HYPOTHESES ABOUT THE CAUSE OF THE "LIQUEFACTION"

5.1 Introduction

The following hypotheses about the cause of the liquefaction is investigated to understand how the colluvium acted like a liquid and flowed across the valley when it was sheared by the slide mass pushing on it:

1) Was its liquidity index greater than 1, so that it flowed when it was disturbed?
2) Was it on the wrong side of the critical state line, so that it liquefied when it was disturbed?
3) Was its "remolded" undrained shear strength so small that it would behave like a liquid relative to the shear stresses imposed?

Using the correlation between liquefaction susceptibility and grain size distribution, water content, plasticity, sensitivity, liquidity index and effective consolidation stress given in Chapter 2, an attempt is made to examine the agreement of the tested specimens with those descriptions of mechanism. The conducted consolidation tests are also used to utilize the data from the literature, and to determine if the information available is consistent with that description of the mechanism, and with our data.

Table 5.1 represents the combined the results obtained from the literature, and this thesis.

Landslide	# of Samples	Moisture Content (%)*	Bulk Density (kg/m^3)*	SpG (Gs)*	LL*	PL*	PI*	LI*	Clay Content (%)*	Soil Classification	Reference
Oso	6	26-36 (30)	1870-1990 (1940)	2.77-2.81 (2.79)	48-70 (59)	24-26 (25)	23-45 (34)	—0.6-0.4 (0.1)	35-66 (47)	CL-CH	Riemer et al., 2015
Oso	14	24-42 (31)	1860-2010 (1940)	2.68-2.79 (2.74)	27-67 (49)	19-28 (22)	8-43 (27)	0.1-2.3 (0.4)	12-52 (27)	CL-CH	GeoTesting Express, 2016
Oso	78	12-41 (30)	1860-2160 (2020)	2.61-2.87 (2.78)	22-59 (44)	NP-31 (26)	NA-31 (19)	—1.7-2.0 (0.1)	16-52 (29)	ML-MH-CL-CH	Badger, 2016
Woodway	7	23-41 (30)			34-72 (41)	24-36 (25)	11-37 (17)	0-0.7 (0.3)		ML-MH	Landau Associates, 1998
Oso	4	27-31 (29)			44-56 (50)	23-27 (25)				CL	Shannon (1952)
Oso	15	16-87 (52)			21-75 (48)	19-31 (25)	2-44 (23)			CL-CH-ML-SC-SM	Keaton et al., 2014
Oso^1	19	23-28 (25)			34-38 (36)	21-24 (22)		0.2-0.25 (0.23)	31-36 (34)		Stark et al., 2017
Oso^2	19	32-37 (34)			52-60 (55)	25-29 (26)		0.27-0.3 (0.29)	51-56 (54)		Stark et al., 2017
Oso	2				48-49 (49)	24-25 (25)	23-25 (24)			CL-CH	Mert, 2019

Table 5.1: Summary of the Obtained Results for Qglv (Advance Glaciolacustrine Clay) Deposits [* Value range (mean)]

Note that in the table Oso^1 is the tests conducted on the low plasticity advance glaciolacustrine clays, and Oso^2 is the one for high-plasticity samples by Stark et al. (2017). It should also be noted that some sample definitions as to their material type and the location of collecting were not very clear in the report presented by Keaton et al. (2014) (given in Table 4.13, e.g., 1B, having a water content of 87%, and a liquid limit of 60%, only HA-3 is clearly described as a lacustrine clay sample). Stark et al. (2017) presented liquidity index test results obtained on 12 samples as between 0.2 and 0.3, thus claimed advance glaciolacustrine clay would likely not undergo a significant strength loss if disturbed. However, Fig. 4.37 shows that they might have higher liquidity indices and fall in a wide range of effective stresses. They also provided sensitivity results, obtained from 8 samples as ranging from 1.4 to 3.3, which describe the samples as slightly to medium sensitive (Mitchell, 1976).

5.2 Effects of Water Content, Plasticity and Liquidity Index

According to ASTM adapted Chinese Criteria given in Figure 5.1, S1 having an LL of 48%, PL of 25%, and a PI of 23%; and D5 having an LL of 49%, PL of 24%, and a PI of 25%, both specimens are likely to fall in the non-liquefiable zone. Green dots on the figure were marked according to the available data for the average values of water content and liquid limits, also considering their plasticity indices. The red dots are from Keaton et al. (2014), and the two samples which fall into the potentially liquefiable zone are the non-plastic (PI=2) samples. 3A is classified as ML, and JW-3 is classified as SC-SM, which may indicate that they are not the members of the glaciolacustrine deposit. However, considering the results obtained from literature for different samples of advance glaciolacustrine clay, especially the low plasticity clay samples with lower clay content are likely to be liquefaction susceptible, but it is not possible to see their exact liquid limit, water content, plastic limit, and plasticity index, rather only their cumulated synthesized average values.

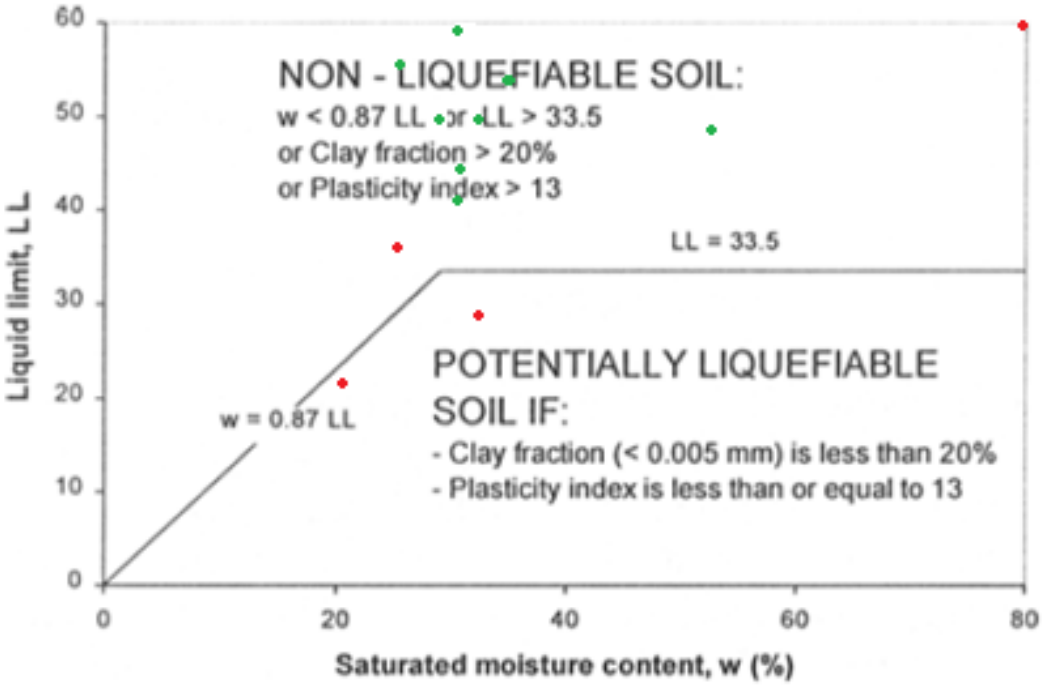

Figure 5.1: Adapted Chinese Criteria to ASTM Soil Properties Definition (from Perlea, 2000)

According to the Modified Chinese Criteria given in Table 2.4, further sampling and testing are required for the samples having liquid limit of less than 32%, and clay contents greater than 10% (Note that none of the tested specimens had clay contents less than 10% and liquid limits less than 32% at the same time).

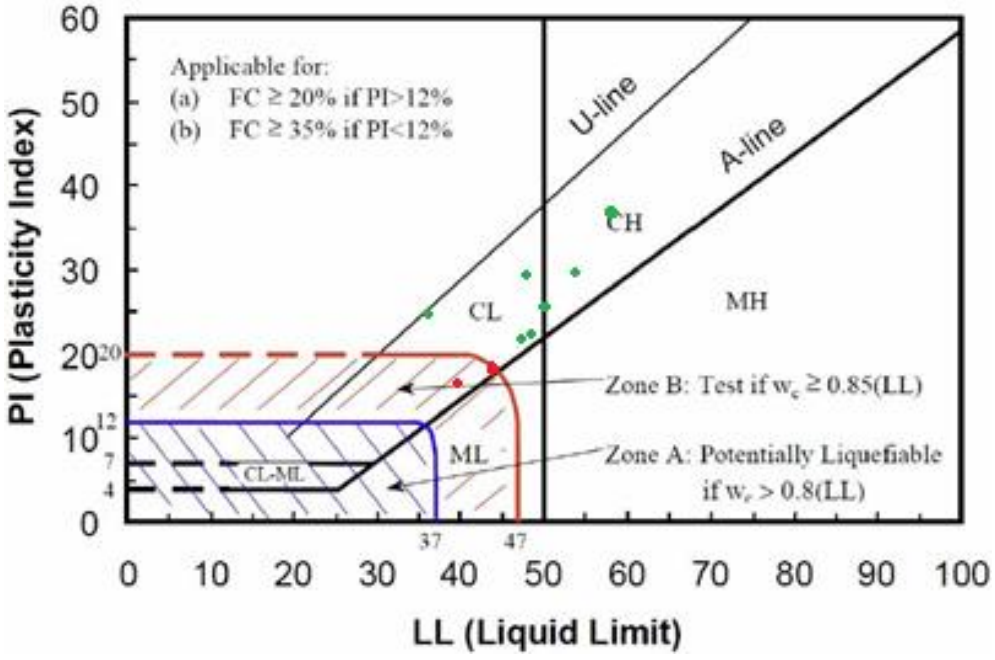

Figure 5.2: Criteria Proposed by Seed et al. (2003) for Liquefaction Susceptibility

Using the criteria proposed by Seed et al. (2003), both S1 and D5, again, are likely to fall in Zone C, which implies non-liquefiable, but might be sensitive. All the collected data points are marked in Fig. 5.2. Considering the obtained average values, 2 sets of data fall in Zone B, where specimens having $w_c \geq 0.85LL$ should further be tested. However, when the minimum plasticity indices and liquid limits given in Table 5.1 are considered, some of them might fall in Zone A, where they are described as potentially liquefiable, and Zone B. Therefore, it is also uncertain to an exact point for the soil tested.

For the liquefaction susceptibility criteria proposed by Bray and Sancio (2006) in Fig. 5.3, considering the obtained average values for plasticity indices and w_c/LL values of the datasets, they are all in the "not susceptible" zone, however, lower plasticity samples (PI $\leq$ 20), depending on their w_c/LL may or may not fall in the susceptible zones considering each sample.

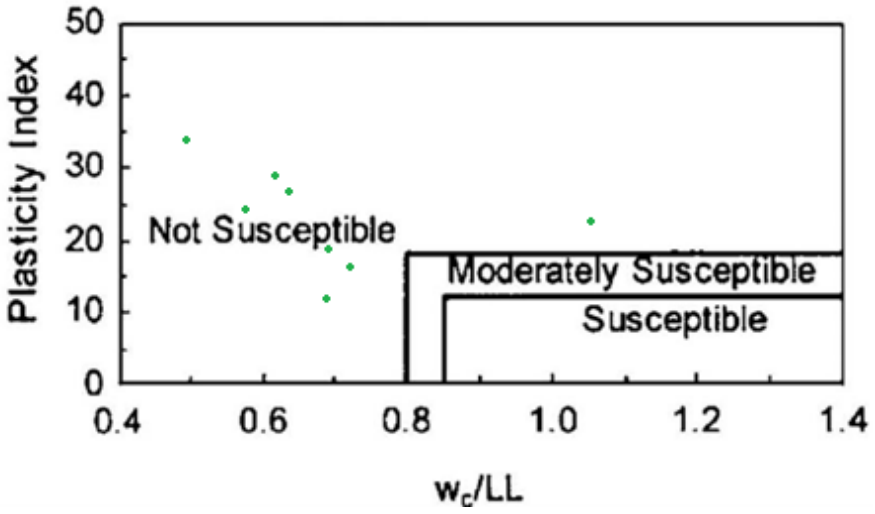

Figure 5.3: Criteria Proposed by Bray and Sancio (2006) for Liquefaction Susceptibility

Equation given below, as described in the literature review chapter, was used to compute the liquidity index of both S1 and D5. An average liquidity index of 0.23 was found by other authors for the advance glaciolacustrine clay in Qglv deposits.

$$LI = \frac{w - PL}{LL - PL}$$

Using the average natural moisture content (30%) presented for the Vashon (Qglv) advance glaciolacustrine clay samples, liquidity indices of 0.22 and 0.24 were found for S1 and D5, respectively. Using their initial water contents before the consolidation tests in the liquidity relationship given, S1 (w_0 = 61.5%) would have a liquidity index, LI = 1.59, and D5 (w_0 = 49.9%) as LI = 1.04, which might make them susceptible to liquefaction. But since they are remolded, this would not reflect the case in-situ.

According to the relationship proposed between effective consolidation stress, sensitivity, and liquidity index (Mitchell, 1993), low-medium sensitivity samples having lower liquidity indices fail under lower vertical effective stresses. The samples tested and resulted with sensitivities of 1.4 to 3.3, having liquidity indices of 0.2 to 0.3 would fail

under 1 kg/cm^2 (2048.2 psf) to 8 kg/cm^2 (16385 psf) vertical effective stress (Fig. 5.4). However, the relationship was not constructed for the actual soil, so it may not agree with the Oso debris.

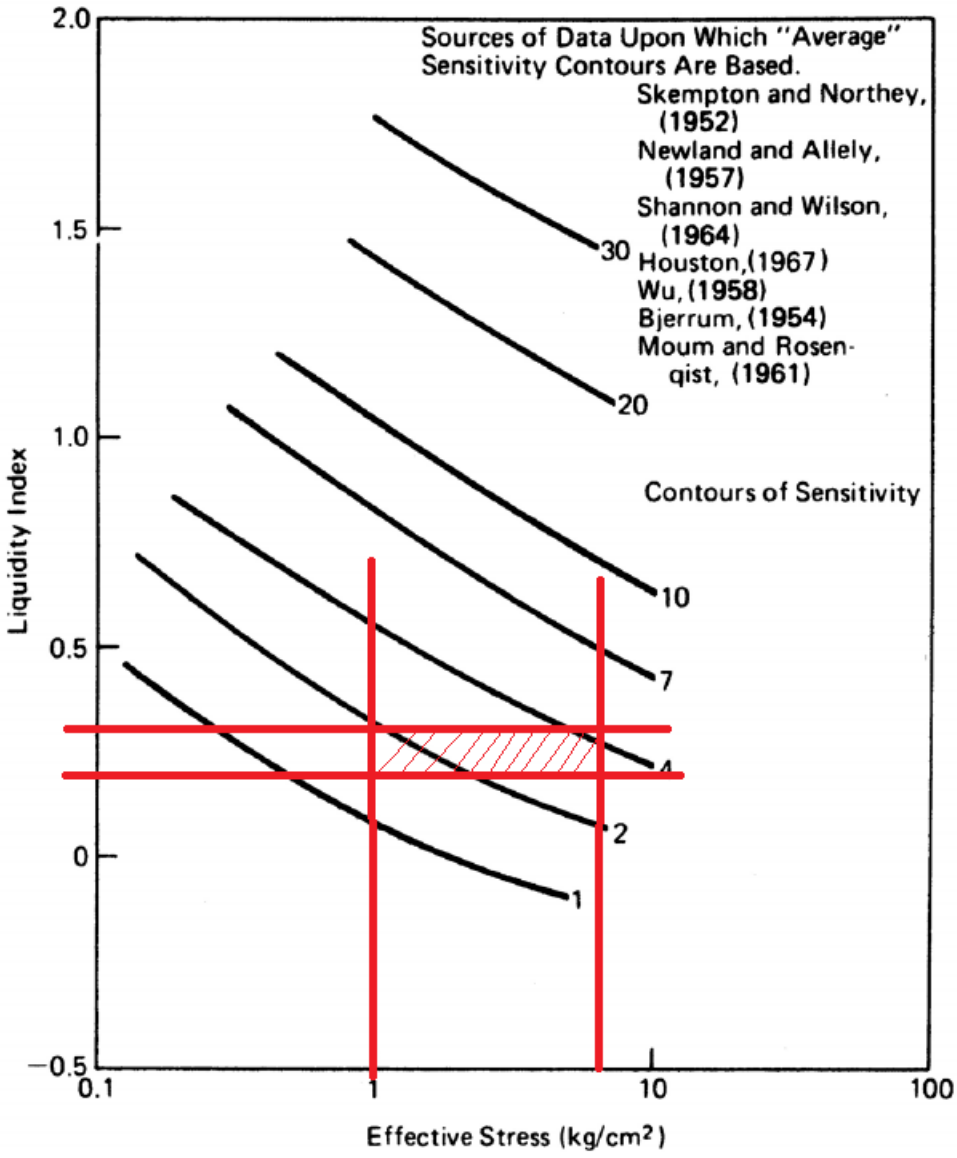

Figure 5.4: Relationship between Effective Consolidation Stress, Sensitivity, and Liquidity Index (Mitchell, 1993)

From the relationship between liquidity index and remolded undrained shear strength (Mitchell, 1993) in Fig. 5.5, the advance glaciolacustrine clay samples from the Oso landslide, having liquidity indices ranging from -1.7 to 2.3, would have remolded shear strength of 0.23 kPa (=4.80 psf) (LI=2.3) to 10000 kPa (=208854 psf) (LI=0.2), the latter might not fall into the reasonable range. However, it is a beneficial indicator as to how much lower it can go in terms of remolded shear strength, and a support for the claim of Stark et al. (2017), that advance glaciolacustrine clay having LI = 0.2 to 0.3, would likely not undergo a significant strength loss if disturbed (still not clear for the colluvium).

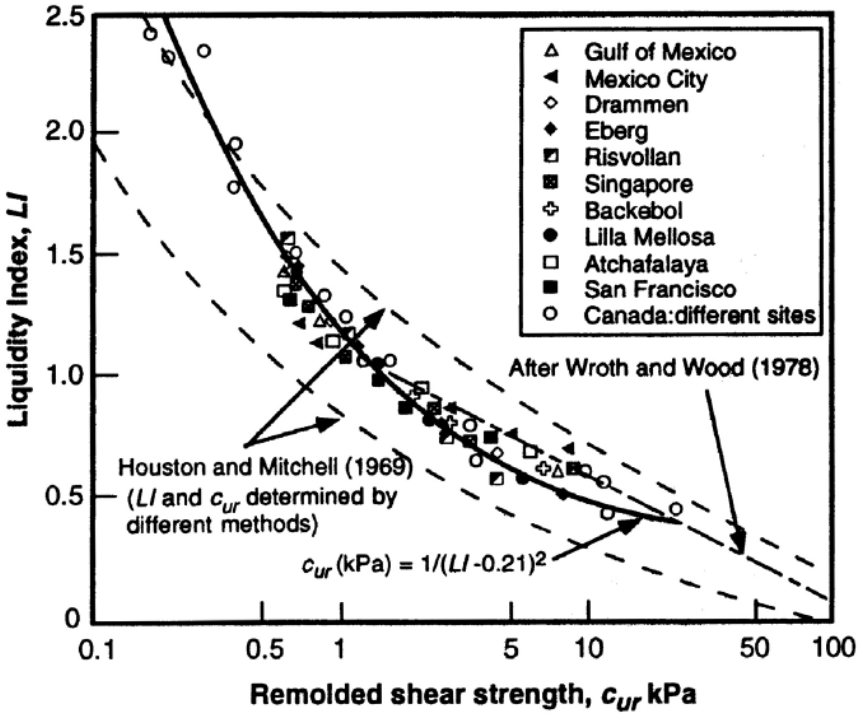

Figure 5.5: Relationship between Liquidity Index and Remolded Undrained Shear Strength (Mitchell, 1993)

Nevertheless, when all synthesized data is considered, it is seen that it is hard to decide if the materials examined are susceptible to liquefaction and undrained shear strength loss.

5.3 Critical State Line

Dilation and strain softening on pre-existing shear surfaces and elsewhere in the glacial-lacustrine unit may be contributing factors to the debris flow. In an overconsolidated state, the glaciolacustrine deposits are on the slopes of the valley undergoing a shear stress caused by the slope. Thus, they dilate over time, increase hydraulic conductivity, absorb more water, soften and weaken. Furthermore, strength degradation could occur on pre-existing shear surfaces in the glacial-lacustrine deposits to residual values. The beds of the glacial-lacustrine deposit contain high plasticity clay and the reduction in strength to the residual value could have taken place gradually along a shear surface and may have led to the initial drainage and the subsequent undrained flow failure. To investigate if the available data falls above the critical state line, work conducted by Casey (2014) was used (Fig. 5.6).

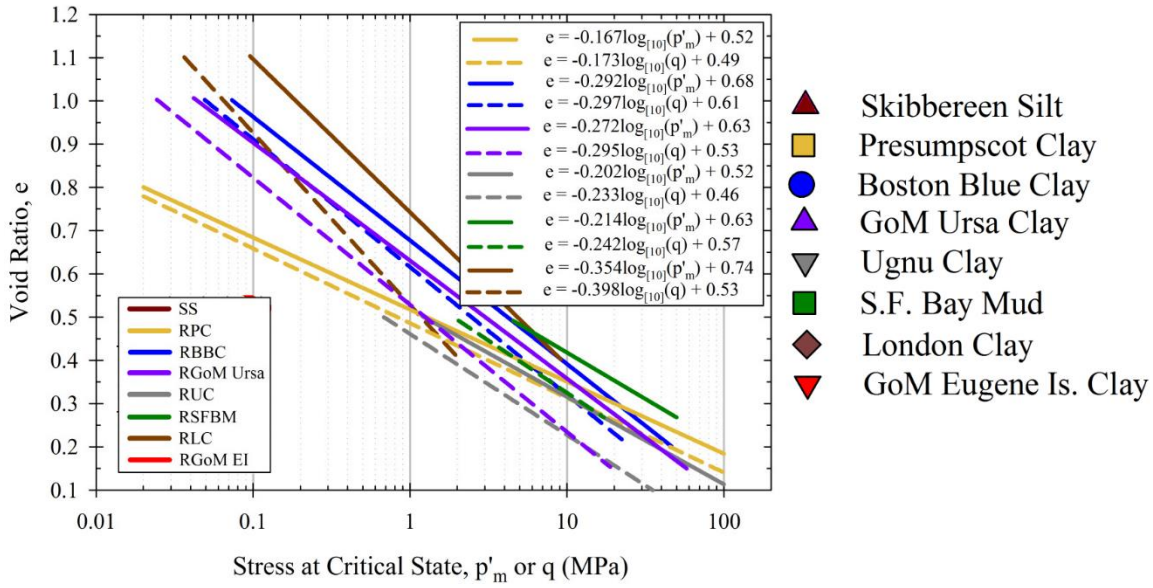

Figure 5.6: Critical State Lines of Mean Effective Stress and Shear Stress for Various Soils (Casey, 2014)

As explained earlier, and can be seen in Fig. 5.7, the most similar soil from the available reference to the advance glaciolacustrine clay in Oso landslide is the Boston Blue Clay.

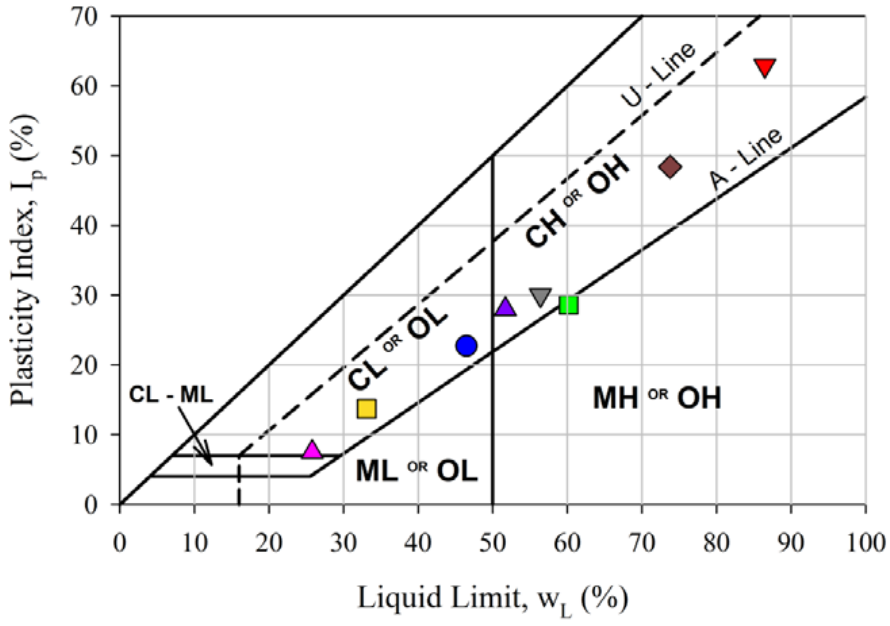

Figure 5.7: Plasticity Charts for Soils in Fig. 5.6 (Casey, 2014)

The critical state line for Boston Blue Clay is reconstructed with the given equation, and the collected available data is plotted and presented in Fig. 5.8. Mean effective stress, p'_m, was calculated as:

$$\boldsymbol{p'm} = \frac{\mathbf{1}}{\mathbf{3}}(\boldsymbol{\sigma 1'} + \mathbf{2}\boldsymbol{\sigma 3'})$$

where σ_1' and σ_3' are the major principle stresses. For σ_3', $K_0 = 0.5$ assumption was made, as follows:

$$\sigma 3' = \sigma 1' * K0$$

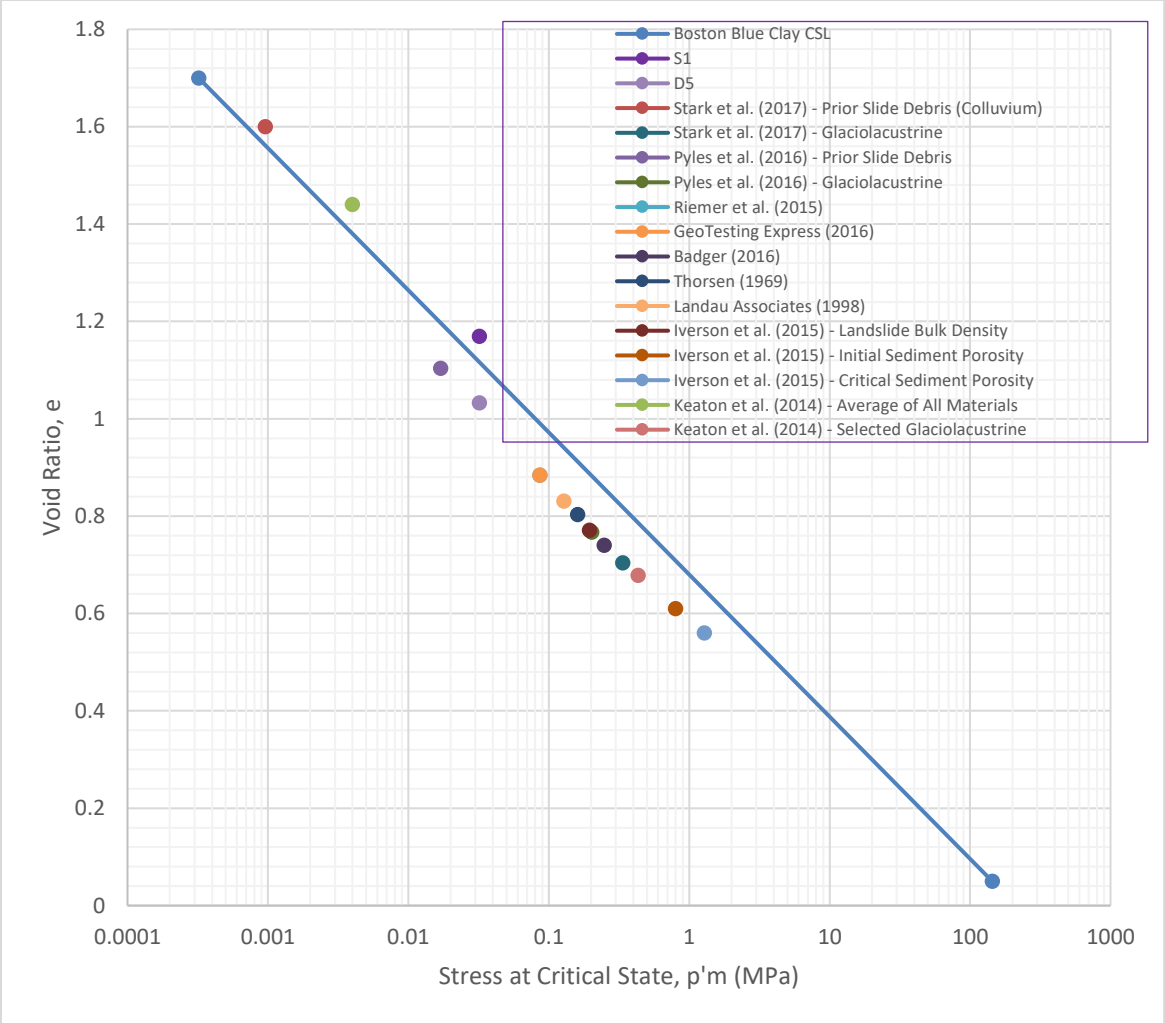

Figure 5.8: Boston Blue Clay Critical State Line and Available Data Plotted

According to the figure, three samples plots above this particular critical state line:

- **Keaton et al. (2014) for the Average of "All Materials" Tested:**

  The most plausible reason for why it was above the critical state line is, as explained before, that the materials tested varied greatly, and did not only involve the advance glaciolacustrine clay, but the average of all the different materials as given in Table 4.13. When only the similar material to the glaciolacustrine clay is chosen (H2 to H6 in the table), it falls below this particular critical state line.

- **Tested S1 Specimen:**

The tested specimen (S1) was remolded at a water content of 61.5% (LL = 48%), and D5 was remolded at a water content of 49.9% (around its liquid limit = 49%, LI = 1.04). This was on purpose to see if it would liquefy above LI = 1 ($LI_{(S1)}$ = 1.59), and apparently, it might have resulted as expected for S1. There might be a chemical effect of using dearied/distilled water for S1, and tap water for D5 during specimen preparation, however, considering the low organic content of the specimens, this effect might be negligible. Since this CSL is not exactly for the debris flow soil itself, this result might also be vague.

- **Stark et al. (2017) – Prior Slide Debris (Colluvium):**

As explained earlier, there is an uncertainty of how the colluvium saturated unit weight assumption was made by the authors. If this assumption is correct, then the material might have fallen above the critical state line. However, Pyles et al. (2016) also proposed a unit weight for the earlier slide debris based on the soil descriptions and field tests (e.g. blow numbers) delineated on the field logs and laboratory measurements of soil density of the samples selected, and their data plot under the critical state line. Also, all the other synthesized data do not support the unit weight, and determined values using the unit weight such as void ratio and water content that was proposed by Stark et al. (2017).

As a result it is hard to explain the liquefaction behavior of the debris flow based on the CSL, since it was a similar, but not identical line for the debris, and the available data, even for the remolded specimen tested, were not obtained for a representative case.

5.4 Low Remolded Undrained Shear Strength

When the role of shear strength was also investigated. Badger and D'Ignazio (2018) found that the strength loss is significant and precipitous from the onset of failure. Through

an intact overconsolidated clay test with pore pressure reinflation for long-term, Carey and Petley (2014) documented such catastrophic failure almost three months after the last stress state increase. The back-analysis using the peak anisotropic and fully softened strengths and pore pressure regimes for intact Qglv deposits replicated the observed Oso landslide failure surface closely. Due to the remolded material being used, the test results reported are likely higher than horizontal shear field conditions, because of the bedding structure preservation in natural slopes. Furthermore, the modeled stability at peak anisotropic strength provided marginal stability and failure was achieved with a fully softened strength value. These results correspond to the hypothesis that slopes on Qglv deposits are stable, although rather marginally, when close-to-peak anisotropic strength conditions exist, and that the peak anisotropic strengths are reasonably approximate to the field conditions from direct shear tests.

Also, the long-understood behavior of loss of strength in overconsolidated silts and clays leads to instability for the measured range of fully softened strength. Stress loss is believed to occur primarily due to cohesion loss, based on comparable frictional strengths of fully softened and peak test results. Long-term stability pattern followed by sudden collapse corresponds to the behavior of time dependent strength loss of overconsolidated clays and silts, and progressive failure. Back-analyses using peak anisotropic strength and limit-equilibrium methods under drained conditions show initial stability of the slopes; failure is calculated near the fully softened strength. After the equation given by Muir Wood (1983), undrained shear strengths were found as 61.8 kPa (9 psi) for S1, and 56.36 kPa (8.2 psi) for D5. Another equation shown in Table 2.5 by Yang et al. (2006) results in similar results, 66.6 kPa (9.7 psi) for S1, and 61.6 kPa (8.9 psi) for D5. It should be noted that these strengths are more likely to be between the residual and the peak shear strengths, rather than being the remolded strengths only.

In order to estimate what the remolded undrained shear strength is based on the information compiled for the colluvium and assessing whether the remolded undrained shear strength is small enough to cause flow, the data provided by Pyles et al. (2016) was used (Table 5.2).

Unit #	Material	Unit Weight (pcf)	OCR	c_u residual (ksf)	ϕ_u residual (deg)	c' TXC peak (ksf)	ϕ' TXC peak (deg)	c' DS peak 90 to bed (ksf)	ϕ' DS peak 90 to bed (deg)	c' DS peak (ksf)	ϕ' DS peak (deg)	c' softened (ksf)	ϕ' softened (deg)	c' residual (ksf)	ϕ' residual (deg)	c_u/σ_v' TXC	ϕ_u TXC (deg)	c_u/σ_v' TXE	ϕ_u TXE (deg)	c_u/σ_v' DSS	ϕ_u DSS (deg)
1a	Recessional Sand and Gravel above GWT	120	1.0	_	_	0	43	_	_	_	_	_	_	_	_	_	_	_	_	_	_
1b	Recessional Sand and Gravel below GWT	130	1.0	_	_	0	43	_	_	_	_	_	_	_	_	_	_	_	_	_	_
2	Recessional Silt	125	1.0	_	_	0	38	_	_	_	_	_	_	_	_	_	_	_	_	_	_
3	Till	140	2.0	_	_	2	40	_	_	_	_	_	_			_	_	_	_	_	_
4	Advance Outwash Silt and Sand	125	1.5	_	_	0	38	_	_	_	_	_	_	_	_	_	_	_	_	_	_
5a	Upper (one-third) Lacustrine Clayey Silt	125	1.3	_	_	0	30	0	26	0	22	0	20	0	12	0.41	0	0.31	0	0.35	0
5b	Upper (one-third) Lacustrine Silty Clay	125	1.3	_	_	0	30	0	26	0	22	0	20	0	12	0.41	0	0.31	0	0.35	0
6a	Lower Lacustrine Clayey Silt under Bench	125	1.3	_	_	0	30	0	26	0	22	0	20	0	12	0.41	0	0.31	0	0.35	0
6b	Lower Lacustrine Silty Clay under Bench	125	1.3	_	_	0	30	0	26	0	22	0	20	0	12	0.41	0	0.31	0	0.35	0
6c	Lower Lacustrine Clayey Silt under Slide	125	1.5	_	_	0	30	0	26	0	22	0	20	0	12	0.41	0	0.31	0	0.35	0
6d	Lower Lacustrine Silty Clay under Slide	125	1.5	_	_	0	30	0	26	0	22	0	20	0	12	0.41	0	0.31	0	0.35	0
7a	Bear Lake Sand under Bench	130	1.3	_	_	0	40	_	_	_	_	_	_	_	_	_	_	_	_	_	_
7b	Bear Lake Sand under Slide	130	1.3	_	_	0	40	_	_	_	_	_	_	_	_	_	_	_	_	_	_
8a	M2 Slide Debris above toe of slide above GWT	115	1.0	0.15	0.0	0	26							0	12						
8b	M2 Slide Debris above toe of slide below GWT	115	1.0	0.15	0.0	0	26							0	12						
9a	Eastern M1 Slide Debris above toe of slide	115	1.0	0.08	0	_	_					0	20	0	12						
9b	Western M1 Slide Debris above toe of slide	115	1.0	0.10	0	_	_					0	20	0	12						
10a	Eastern 2006 Debris Field below toe of slide	115	1.0	0.04	0	_	_							0	12						
10b	Western 2006 Debris Field below toe of slide	115	1.0	0.05	0	_	_							0	12						

Note: 1 ksf = 1000 psf = 47.87 kPa

Table 5.2: Estimated Engineering Properties of Soils (from Pyles et al., 2016)

After triaxial compression (TXC), triaxial extension (TXE) and direct simple shear (DSS) tests, they have obtained s_u/σ_v' for the glaciolacustrine deposits as 0.41, 0.31, and 0.35, respectively. Using the data, corresponding lines were plotted for changing undrained shear strength against vertical effective stress.

Obtaining the liquidity indices for the samples as explained earlier, using the relationship given by Yang et al. (2006), their remolded undrained shear strengths were assessed. Then, the corresponding vertical effective stresses to their water contents (or void ratios) on the consolidation curve obtained earlier were determined. These values then were plotted on the same graph with the available data for undrained shear strength and vertical effective stresses given by Pyles et al. (2016) (Fig. 5.9).

$$\boldsymbol{Su = 159.6e^{-3.97LI}\ (kPa)\ (Yang\ et\ al.,2006)}$$

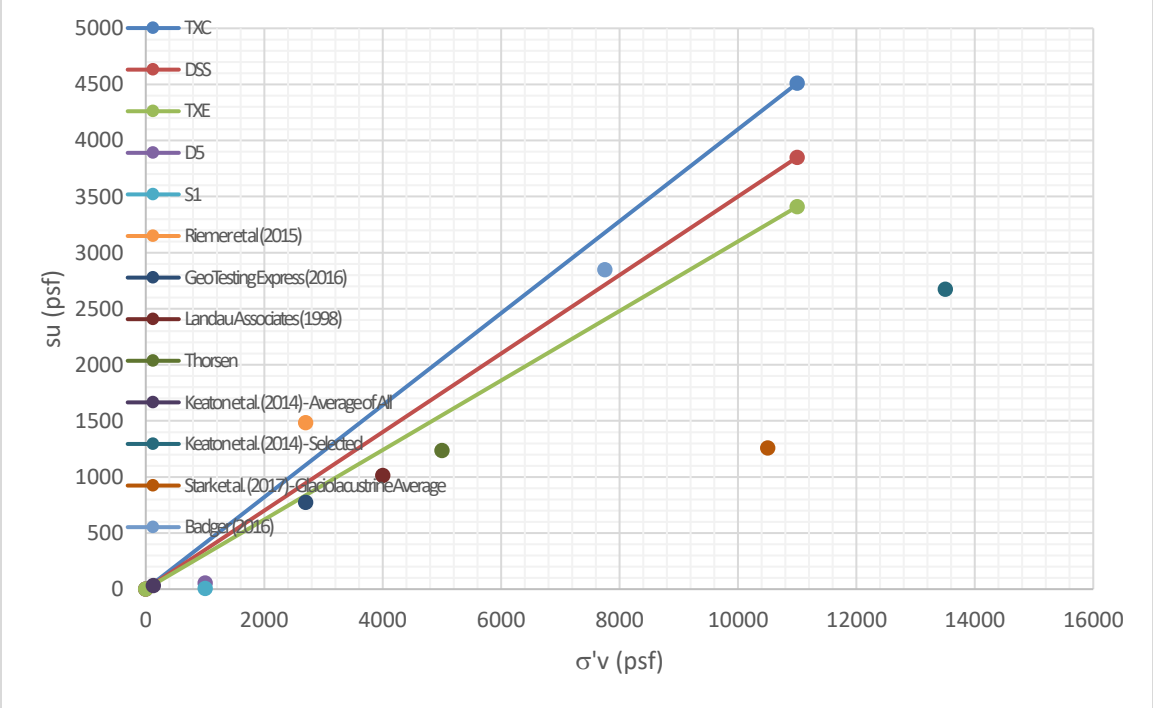

Figure 5.9: Failure Envelopes for the Undrained Shear Strength

As can be seen from the figure, there is a scatter for all the data above and below the failure envelopes at their corresponding vertical effective stresses under consolidation.

It should be noted that the data for the colluvium from Stark et al. (2017) and Pyles et al. (2016) could not have been used, since the corresponding values of liquid limit and plastic limit were not available, which are necessary to calculate the liquidity index.

However, this data might not represent the actual data, and thus is hard to explain again why it flowed like a liquid, since a better characterization of the debris is also needed.

5.5 Summary

Answers to the following questions regarding the hypotheses about the cause of the liquefaction was investigated to understand how the colluvium acted like a liquid and flowed across the valley when it was sheared by the slide mass pushing on it:

1) Was its liquidity index greater than 1, so that it flowed when it was disturbed?
2) Was it on the wrong side of the critical state line, so that it liquefied when it was disturbed?
3) Was its "remolded" undrained shear strength so small that it would behave like a liquid relative to the shear stresses imposed?

Using the correlation between liquefaction susceptibility and grain size distribution, water content, plasticity, sensitivity, liquidity index and effective consolidation stress given in Chapter 2, an attempt was made to examine the agreement of the tested specimens with those descriptions of mechanism. The conducted consolidation tests are also used to utilize the data from the literature, and to determine if the information available is consistent with that description of the mechanism, and with our data.

According to the ASTM adapted Chinese Criteria, S1 having an LL of 48%, PL of 25%, and a PI of 23%; and D5 having an LL of 49%, PL of 24%, and a PI of 25%, both

specimens are likely to fall in the non-liquefiable zone. When the available datapoints were marked on the corresponding chart, and the two samples from Keaton et al. (2014) which fall into the potentially liquefiable zone were the non-plastic (PI=2) samples. 3A was classified as ML, and JW-3 was classified as SC-SM, which may indicate that they are not the members of the glaciolacustrine deposit. However, considering the results obtained from literature for different samples of advance glaciolacustrine clay, especially the low plasticity clay samples with lower clay content are likely to be liquefaction susceptible, but it is not possible to see their exact liquid limit, water content, plastic limit, and plasticity index, rather only their cumulated synthesized average values.

According to the Modified Chinese Criteria, further sampling and testing are required for the samples having liquid limit of less than 32%, and clay contents greater than 10% (Note that none of the tested specimens had clay contents less than 10% and liquid limits less than 32% at the same time).

Using the criteria proposed by Seed et al. (2003), both S1 and D5, again, were likely to fall in Zone C, which implies non-liquefiable, but might be sensitive. All the collected data points were marked, and considering the obtained average values, 2 sets of data fall in Zone B, where specimens having $w_c \geq 0.85LL$ should further be tested. However, when the minimum plasticity indices and liquid limits given in Table 5.1 are considered, some of them might fall in Zone A, where they are described as potentially liquefiable, and Zone B. Therefore, it is also uncertain to an exact point for the soil tested.

For the liquefaction susceptibility criteria proposed by Bray and Sancio (2006), considering the obtained average values for plasticity indices and w_c/LL values of the datasets, they are all in the "not susceptible" zone, however, lower plasticity samples ($PI \leq 20$), depending on their w_c/LL may or may not fall in the susceptible zones considering each sample.

Using the average natural moisture content (30%) presented for the Vashon (Qglv) advance glaciolacustrine clay samples, liquidity indices of 0.22 and 0.24 were found for S1 and D5, respectively. Using their initial water contents before the consolidation tests in the liquidity relationship given, S1 (w_0 = 61.5%) would have a liquidity index, LI = 1.59, and D5 (w_0 = 49.9%) as LI = 1.04, which might make them susceptible to liquefaction. But since they are remolded, this would not reflect the case in-situ.

According to the relationship proposed between effective consolidation stress, sensitivity, and liquidity index (Mitchell, 1993), low-medium sensitivity samples having lower liquidity indices fail under lower vertical effective stresses. The samples tested and resulted with sensitivities of 1.4 to 3.3, having liquidity indices of 0.2 to 0.3 would fail under 1 kg/cm^2 (2048.2 psf) to 8 kg/cm^2 (16385 psf) vertical effective stress. However, the relationship was not constructed for the actual soil, so it may not agree with the Oso debris.

From the relationship between liquidity index and remolded undrained shear strength (Mitchell, 1993), the advance glaciolacustrine clay samples from the Oso landslide, having liquidity indices ranging from -1.7 to 2.3, would have remolded shear strength of 0.23 kPa (=4.80 psf) (LI=2.3) to 10000 kPa (=208854 psf) (LI=0.2), the latter might not fall into the reasonable range. However, it is a beneficial indicator as to how much lower it can go in terms of remolded shear strength, and a support for the claim of Stark et al. (2017), that advance glaciolacustrine clay having LI = 0.2 to 0.3, would likely not undergo a significant strength loss if disturbed (still not clear for the colluvium). Nevertheless, when all synthesized data is considered, it is seen that it is hard to decide if the materials examined are susceptible to liquefaction and undrained shear strength loss.

To investigate if the available data falls above the critical state line, work conducted by Casey (2014) was used. As explained earlier, and can be seen in Fig. 5.7, the most similar soil to the advance glaciolacustrine clay in Oso landslide is the Boston Blue Clay.

The critical state line for Boston Blue Clay is reconstructed with the given equation, and the collected available data is plotted and presented in Fig. 5.8. Mean effective stress, p'_m, was calculated with an assumption of $K_0 = 0.5$.

According to the figure, three samples plots above this particular critical state line:

- **Keaton et al. (2014) for All Materials Tested:**

The most plausible reason for why it was above the critical state line is, as explained before, that the materials tested varied greatly, and did not only involve the advance glaciolacustrine clay, but the average of all the different materials as given in Table 4.13. When only the similar material to the glaciolacustrine clay is chosen (H2 to H6 in the table), it falls below the critical state line. According to the figure, three samples plots above this particular critical state line only.

- **Tested S1 Specimen:**

The tested specimen (S1) was remolded at a water content of 61.5% (LL = 48%), and D5 was remolded at a water content of 49.9% (around its liquid limit = 49%, LI = 1.04). This was on purpose to see if it would liquefy above LI = 1 ($LI_{(S1)}$ = 1.59), and apparently, it might have resulted as expected for S1. There might be a chemical effect of using dearied/distilled water for S1, and tap water for D5 during specimen preparation, however, considering the low organic content of the specimens, this effect might be negligible. Since this CSL is not exactly for the debris flow soil itself, this result might also be vague.

- **Stark et al. (2017) – Prior Slide Debris (Colluvium):**

There is an uncertainty of how the colluvium saturated unit weight assumption was made by the authors. If this assumption is correct, then the material would have fallen above the critical state line. However, Pyles et al. (2016) also proposed a unit weight for the earlier slide debris based on the soil descriptions and field tests (e.g. blow numbers)

delineated on the field logs and laboratory measurements of soil density of the samples selected, and their data plot under the critical state line. Also, all the other synthesized data do not support the unit weight, and determined values using the unit weight such as void ratio and water content that was proposed by Stark et al. (2017).

As a result it is hard to explain the liquefaction behavior of the debris flow based on the CSL, since it was a similar, but identical line for the debris, and the available data, even for the remolded specimen tested, were not obtained for a representative case.

In order to estimate what the remolded undrained shear strength is based on the information compiled for the colluvium and assessing whether the remolded undrained shear strength is small enough to cause flow, the data provided by Pyles et al. (2016) was used.

After triaxial compression (TXC), triaxial extension (TXE) and direct simple shear (DSS) tests, they have obtained s_u/σ_v' for the glaciolacustrine deposits as 0.41, 0.31, and 0.35, respectively. Using the data, corresponding lines were plotted for changing undrained shear strength against vertical effective stress.

Obtaining the liquidity indices for the samples, using the relationship given by Yang et al. (2006), their remolded undrained shear strengths were assessed. Then, the corresponding vertical effective stresses to their water contents (or void ratios) on the consolidation curve obtained earlier were determined. These values then were plotted on the same graph with the available data for undrained shear strength and vertical effective stresses given by Pyles et al. (2016).

As a result, there is a scatter for all the data above and below the failure envelopes at their corresponding vertical effective stresses under consolidation. However, this data might not represent the actual data, and thus is hard to explain again why it flowed like a liquid, since a better characterization of the debris is also needed.

It should be noted that the data for the “colluvium” from Stark et al. (2017) and Pyles et al. (2016) could not have been used, since the corresponding values of liquid limit and plastic limit were not available, which are necessary to calculate the liquidity index. However, the general trend all the other available data is likely enough to support that the remolded undrained shear strength loss would possibly occur in the colluvium as well. Having similar results earlier with the Stark et al. (2017) data, the average data considering all the materials from Keaton et al. (2014) displays failure.

CHAPTER 6: CONCLUSIONS AND RECOMMENDATIONS

Landslides cause damage to property, injury and death and have an adverse effect on various resources. For example, after years of sliding event, water supplies, fisheries, waste disposal systems, forests, dams and roads can still be affected. One of the most disastrous landslides in the U.S. occurred in Washington state, taking 43 lives and destroying about 50 homes of the Steelhead Drive Community (Keaton et al. 2014; Iverson et al. 2015 and Wartman et al. 2016).

The primary objectives of this research were to compare the volume of the 2014 debris run-out with the volume of the colluvium at the toe of the slope prior to the 2014 slide, to estimate the properties of the colluvium, to explore hypotheses about how the strength of the colluvium reduced enough for it to flow like a liquid, and to provide guidance for future projects to identify the possibility of a large run-out like this event.

To achieve these objectives, a literature review and an experimental program comprising the following was conducted:

1. Compiling all the available information about the 2014 debris flow,
2. Conducting supplementary laboratory testing on remolded samples from the slope,
3. Summarizing the synthesized available literature on the mechanisms of the 2014 debris flow,
4. Investigating hypotheses to explain the Oso debris flow.

Conducting a literature review, the empirical mobility predictions for debris flows and Oso landslide were discussed. Liquefaction and cyclic mobility, liquidity index, sensitivity and effective consolidation stress, rainfall-induced debris flows, field stress path and the stress transfer, one-dimensional consolidation and void ratio, and the steady-state lines for soils with various fines content and the description of the intrinsic compression

line and other hypotheses that might have led to the 2014 debris flow were also presented. The relations between Atterberg limits and the liquidity index and the remolded shear strength and water content have been examined subsequently. A further description was also provided for the debris flows and the deposition.

The general information on Oso landslide, followed by the literature on hydrological mechanics, stability, subsurface conditions, material properties, and the history of the landslide were presented, the geotechnical soil characterization of Qglv deposits was summarized, following which, through several tests conducted by researchers, geotechnical, geomorphical and hydrogeological characteristics were examined.

Answers to the following questions regarding the hypotheses about the cause of the liquefaction was investigated to understand how the colluvium acted like a liquid and flowed across the valley when it was sheared by the slide mass pushing on it:

- Was its liquidity index greater than 1, so that it flowed when it was disturbed?
- Was it on the wrong side of the critical state line, so that it liquefied when it was disturbed?
- Was its "remolded" undrained shear strength so small that it would behave like a liquid relative to the shear stresses imposed?

Two main conclusions can be drawn:

1) After the run-out and colluvium volume comparison, the outcome meant that the landslide terminus has been reached with other materials with the colluvium that could include previously in-place outwash, lacustrine, till deposits and/or sediments in riverbed.
2) It is hard to explain why the debris flowed like a liquid, and the liquiefaction behavior of the debris flow based on the CSL, since it was a similar, but not

identical line for the debris, and the available data, even for the remolded specimen tested, were not obtained for a representative case.

Future research follow up may consist of:

- Obtaining more specific data from the field for the actual soil conditions, such as a better representative of water content and shear strength,
- Better characterization of the colluvium or the debris,
- A device might be constructed to better represent the field conditions that the debris flow undergone,
- Using the more specific undrained shear strengths to further analyze and compare with the tests that can present the undrained shear strength, directly or indirectly,
- Further testing the samples that are likely to fall in moderately-susceptible or potentially-susceptible to liquefaction,
- Performing isotropically (ICU) and/or anisotropically consolidated undrained (ACU) triaxial tests to better represent the debris flow failure path, and to plot the actual critical-state lines of the soils to determine the contractive/dilative behavior of the specimens for liquiefaction and strength loss susceptibility.

References

[Anderson, A.A., Sitar, N., (1995). *"Analysis of Rainfall-Induced Debris Flows",* ASCE, J. Geotech. Engrg., 121(7): 544-552

Andrews, D.C.A., & Martin, G.R. 2000. Criteria for liquefaction of silty soils. *Proceedings of the 12th World Conference on Earthquake Engineering* (12WCEE), Paper No. 0312.

Armstrong, J.E., Crandell, D.R., Easterbrook, D.J., Noble, J.B., (1965). Late Pleistocene Stratigraphy and Chronology in Southwestern British Columbia and Northwestern Washington. Vol. 76. Geological Society of America Bulletin v, pp. 321–330.Badger, T. C. (2015). "Geotechnical report: SR 520 MP 35 to 41 geotechnical study, Washington." Washington Dept. of Transportation, Olympia, WA.

Arndt, B.P., (1999). Determination of the Conditions Necessary for Slope Failure of a Deep-Seated Landslide at Woodway, Washington. Colorado School of Mines M.S. thesis, 223 p.

ASTM D2216-10, (2010). Standard Test Methods for Laboratory Determination of Water (Moisture) Content of Soil and Rock by Mass, ASTM International, West Conshohocken, PA, www.astm.org

ASTM D2435 / D2435M-11, (2011). Standard Test Methods for One-Dimensional Consolidation Properties of Soils Using Incremental Loading, ASTM International, West Conshohocken, PA, www.astm.org.

ASTM D2487-06, (2006).Standard Practice for Classification of Soils for Engineering Purposes (Unified Soil Classification System)

ASTM D2488-09a, (2009). Standard Practice for Description and Identification of Soils (Visual-Manual Procedure)

ASTM D4318-17e1, (2017). Standard Test Methods for Liquid Limit, Plastic Limit, and Plasticity Index of Soils, ASTM International, West Conshohocken, PA, www.astm.org.

Badger, T.C., (2015). SR 530 MP 35 to 41 Geotechnical Study. 198 Washington State Department of Transportation

Badger, T.C., 2016. SR 530 Landslide: Geotechnical Data Report. Washington State

Badger, T.C., D'Ignazio, M. (2018). First-time landslides in Vashon advance glaciolacustrine deposits, Puget Lowland, U.S.A.

Been, K., and Jefferies, M.G. (1985). A state parameter for sands. Géotechnique, **35**(2): 99–112.

Beverage,J .P., and J. K. Culbertson (1964), Hyperconcentrations of suspended sediments, J . Hydraul. Div. Am. Soc. Civ. Eng.,90(HY6), 117-128, 1964

Bishop, A. W. (1967). "Progressive failure—with special reference to the mechanism causing it." *Proc, Geotechnical Conference,* Oslo, Norway, Vol. 2, 142-150.

Bjerrum L. (1954). Geotechnical properties of Norwegian marine clays. Géotechnique;4(2):49-69.

Bjerrum L. (1973). Problems of soil mechanics and construction on soft clays and structurally unstable soils (collapsible, expansive and others). In: Proceedings of the 8th International Conference on Soil Mechanics and Foundation Engineering, Moscow; p. 111-59.

Bobet, A., Hwang, J., Johnston, C.T., Santagata, M., Canadian Geotechnical J., (2011), 48(7): 1100-1115.

Bouckovalas, G.D., Andrianopoulos, K.I., and Papadimitriou, A.G. 2003. A critical state interpretation for the cyclic liquefaction resistance of silty sands. Soil Dynamics and Earthquake Engineering, **23**(2): 115–125.

Boulanger, Ross & Idriss, I. (2004). Evaluating Cyclic Failure in Silts and Clays. REPORT NO. UCD/CGM-04/01 Center for Geotechnical Modeling Department of Civil & Environmental Engineering University of CaliforniaBurland, J.B. (1990). On the compressibility and shear strength of natural clays. Géotechnique, 40(3): 329–378.

Bray, J.D., & Sancio, R.B. 2006. Assessment of the liquefaction susceptibility of fine-grained soils. *Journal of Geotechnical and Geoenvironmental Engineering*. 132 (9): 1165–1177.

Bray, J.D., & Sancio, R.B. 2008. Closure: Assessment of the liquefaction susceptibility of fine-grained soils. *Journal of Geotechnical and Geoenvironmental Engineering*. 134 (7): 1031–1034.

Butterfield, R., (1979), "A Natural Compression Law for Soils (an Advance on e–log p0)," Ge´otechnique, Vol. 29(4), pp. 469–480.

Cao, Q., Henn, B., and Lettenmaier, D. P. (2014). "Analysis of local precipitation accumulation return periods preceding the 2014 Oso mudslide." Department of Civil and Environmental Engineering, Univ. of Washington, Seattle.

Carey, J.M., Petley, D.N., (2014). Progressive shear-surface development in cohesive materials; implications for landslide behavior. Eng. Geol. 177, 54–65.

Casagrande, A. Classification and identification of soils. Transactions, ASCE, vol.113, 901-930.

Casagrande, A., (1971). "On Liquefaction Phenomena," *Geotechnique,* London, England, Vol. **XXI,** No. 3, Sept., 1971, pp. 197-202.

Casagrande, A., (1975). "Liquefaction and Cyclic Deformation of Sands, A Critical Review," *Harvard Soil Mechanics Series No. 88,* Harvard University, Cambridge, Mass.

Castro, Gonzalo & J. Poulos, Steve. (1977). Factors affecting liquefaction and cyclic mobility. ASCE J Geotech Eng Div. 103. 501-516.d

Castro, G., Poulos, S.J., and Leathers, F.D. (1985). Re-examination of slide of Lower San Fernando dam. Journal of Geotechnical Engineering, ASCE, **111**(9): 1093–1107.

Cerato, A. B. & Lutenegger, A. J. (2004). Determining intrinsic compressibility of fine-grained soils. J. Geotech. Geoenviron. Engng, ASCE 130, No. 8, 872–877.

Cooper Testing Laboratory, (2016). Unpublished soil testing results, prepared for the Washington Office of the Attorney General.

Corominas, J. (1996), The angle of reach as a mobility index for small and large landslides, Canadian Geotechnical Journal, 33, pp. 260–271**.**

Cruden, D.M., (1991). "A simple description of a landslide", *Bulletin IAEG*, No. 43, pp.27-29.

Department of Transportation, pp. 355 http://www.wsdot.wa.gov/publications/ fulltext/Projects/SR530/SR530MP35to41GeotechnicalStudy.pdf.

Dolinar B. (2010). Predicting the normalized, undrained shear strength of saturated fine-grained soils using plasticity-value corrections. Applied Clay Science;47(3-4):428-32.

Dragovich, J. D., Stanton, B. W., Lingley Jr, W. S., Griesel, G. A., and Polenz, M. (2003). "Geologic map of the mount Higgins 7.5-minute quadrangle, Skagit and Snohomish Counties, Washington." Rep. No. 2003-12, Washington Divisions of Geology and Earth Resources, Olympia, WA.

Eckersley. J. D. (1990), "Instrumented laboratory flowslides." *Geotechnique.* London. England. 40(3), 489-502.

Ellen. S. D. (1988). "Chapter 6: description and mechanics of soil slip/ debris flows in the storm." *Profl. Paper 1434: Landslides, Floods, and Marine Effects of the Storm of January* 3-5, 1982, *in the San Francisco Bay Region, California,* S. D. Ellen and G. F. Wieczorek. cds.. U.S. Geological Survey, Washington, D.C. 63-112.

Galster, R.W., Laprade, W.T., (1991). Geology of Seattle, Washington United States of

America. Bulletin of the Association of Engineering Geologists 235–302.

Gamez, J., and Stark, T. D. (2014). "Fully softened shear strength at low stresses for levee and embankment design." J. Geotech. Geoenviron. Eng., 10.1061/(ASCE)GT.1943-5606.0001151, 06014010.

Garga, V.K., and Zhang, H. (1997). Volume changes in undrained triaxial tests on sands. Canadian Geotechnical Journal, **34**: 762–772.

Gault, A.M., (2015). The Mineralogy and Strength Characteristics of Selected Glaciolacustrine Clays in the Puget Sound Region, Unpublished Report. University of Washington (60 p).

Geoslope, (2018). Slope/W Version 9.0.0. pp. 15234.

GeoTesting Express, (2016). Unpublished soil testing results, prepared for the Washington Office of the Attorney General.

Gibson, R.E., Schiffman, R.L., and, Cargill K.W., (1981). "The theory of one-dimensional consolidation of saturated clays, II. Finite nonlinear consolidation of thick homogeneous layers.", Canadian Geotechnical J., 18(2): 280-293.

Gilbert, R., Montgomery, D., Anderson, S., Keaton, J., Benoit, J., deLaChapelle, J. and Wartman, J. (2016), "Lessons about Managing Landslide Risk from the 2014 Oso, Washington Landslide" 5ICFGE Proceedings

Graham J, Li ECC. (1985). Comparison of natural and remolded plastic clay. Journal of Geotechnical Engineering;111(7):865-81.

Gratchev, I. B., Sassa, K., Fukuoka, H., (2006). "How Reliable is the Plasticity Index for Estimating the Liquefaction Potential of Clayey Sands?", J. Geotech. Geoenviron. Eng., 132(1): 124-127.

Harr. R. D. (1977), "Water flux in soil and subsoil on a steep forested slope." *J. Hydro.,* 33(1/2), 37-58.

Heim, A., (1932), Bergsturz und Menschenleben. Naturforschenden Gesellschaft, Zürich. Translated by Skermer, N.A., 1989. Landslides and Human Lives. BiTech Publishers, Vancouver, British Columbia.

Henn, B., Cao, Q., Lettenmaier, D. P., Magirl, C. S., Mass, C., Bower, J. B., St. Laurent, M., Mao, Y., Perica, S. (2015), Hydroclimatic Conditions Preceding the March 2014 Oso landslide. *J. Hydrometeor*, v. 16, p. 1243–1249.

Hind, K.J. (2017). "The Casagrande plasticity chart –does it help or hinder the NZGS soil classification process?", Proc. 20th NZGS Geotechnical Symposium., Eds. GJ Alexander & CY Chin, Napier

Hirata, S., Yao, S., and Nishida, K., (1990), “Multiple Regression Analysis between the Mechanical and Physical Properties of Cohesive Soils,” Soils and Foundations., Vol. 30(3), pp. 91–108.

Holtz, R.D., Kovacs, W.D., Sheahan, T.C., (2011). An Introduction to Geotechnical Engineering, 2nd Edition. Prentice Hall.

Hong, Z.S.; Yin, J., Cui, Y.J., (2010). Geotechnique, London, Vol. 60, Iss. 9, (Sep 2010): 691-700.

Hungr, O., Corominas, J. & Eberhardt, E. (2005), Estimating landslide motion mechanism, travel distance and velocity. In *Landslide Risk Management*. Edited by O. Hungr, R. Fell, R. Couture & E. Eberhardt, A.A. Balkema, Leiden, pp. 99-128.

Hunter, G. J., and Fell, R. (2003a). “Mechanics of failure of soil slopes leading to” rapid” failure.” Fast slope movements: Prediction and prevention for risk mitigation, L. Picarelli, ed., Patron Editore, Bologna, Italy, 283–290.

Hynes, M.E. (1999). "Dam lessons learned from major earthquakes this year." *Private Communication.*

ldriss, I.M. (1985). "Evaluating seismic risk in engineering practice." *Proc.. 11 th Int. Conf. on Soil Mechanics and Foundation Engrg* San Francisco, Vol 1,255-320.

Iverson, R.M., (1997), The physics of debris flows: *Reviews of Geophysics,* v. 35, pp. 245-296.

Iverson, R.M. 1997a. The physics of debris flows. *Reviews of Geophysics* 35: 245-296.

Iverson, R. M. (2003), “The debris-flow rheology myth,” *Proc. Debris-Flow Hazards Mitigation: Mechanics, Prediction and Assessment,* Millpress, Rotterdam, ISBN 90 77017 78 X.

Iverson, R. M., et al. (2015). “Landslide mobility and hazards: Implications of the 2014 Oso disaster.” Earth Planetary Sci. Lett., 412(1), 197–208.

Iverson, R. M., and George, D. L. (2016). “Modelling landslide liquefaction, mobility bifurcation and the dynamics of the 2014 Oso disaster.” Géotechnique, 66(3), 175–187.

Jaboyedoff, M., Horton, P., Loye, A and Pedrazzini, A. (2008), Runout – Empirical Approaches, Workshop on Quantitative Landslide Risk Assessment and Risk Management, Barcelona, Spain, powerpoint presentation.

Japan Society of Civil Engineers (1977). *"Earthquake resistant design for civil engineering structures. Earth structures and foundations in Japan."*

Johnson, A.M., (1984). Debris flow, in Slope Instability, edited by D. Brunsden and D. B. Prior, pp. 257-361, John Wiley, New York.

Johnson, K, A. (1987). "An investigation of the mechanisms of debris flow initiation," PhD thesis. University of California, Berkeley.

Johnson, K. A., and Sitar, N. (1989). "Significance of transient pore pressures and local slope conditions in debris flow initiation." *Proc., 12th Int. Conf. on Soil Mech. and Found. Engrg.,* A. A. Balkema, Brookfield. Vt., Vol. 2, 1619-1622.

Johnson. K. A., and Sitar, N. (1990). "Hydrologic conditions leading to debris flow initiation." *Can. Geotech.* J., 27(6), 789-801.

Kayabali, K., and Tufenkci, O. O., (2010), “Shear Strength of Remolded Soils at Consistency Limits,” Canadian Geotech. Journal, Vol. 47(3), pp. 259–266.

Keaton, J.R., Wartman, J., Anderson, S., Benoit, J., De La Chapelle, J., Gilbert, R., Montgomery, D.R., (2014). The 22 March 2014 Oso Landslide, Snohomish County. Geotechnical Extreme Events Reconnaissance (GEER), Washington, pp. 186.

Kim, J. W., Lu, Z., Qu, F., and Hu, X. (2015). “Pre-2014 mudslides at Oso revealed by InSAR and multi-source DEM analysis.” Geomatics Nat. Hazards Risk, 6(3), 184–194.

Kishida, H. (1969). "Characteristics of liquefied sands during Mino-Owari, Tohnankai and Fukui earthquakes." *Soils and Foundations,* Vol.9, No. I, 75-92.

Koumoto, T., and Houlsby, G. T., (2001), “Theory and Practice of the Fall Cone Test,” Ge´otechnique., Vol. 51(8), pp. 701–712.

Kramer, S.L. (1989). Uncertainty in steady state liquefaction evaluation procedures. Journal of Geotechnical Engineering, ASCE, **115**(10): 1402–1419.

Lade. P. V. (1992). "Static instability and liquefaction of loose fine sandy slopes." *J. Geotech. Engrg.,* ASCE. 118(1),51-71.

Lade. P. V. (1993). "Initiation of static instability in the Nerlerk berm." *Can. Geotech. J..* 30(6), 895-904.

Lambe, T.W. (1951). Soil Testing for Engineers, Wiley, New York, 165 p.

Landau Associates, (1998). Geotechnical Engineering Services Woodway Landslide

Dominican Reflection Center Woodway, Washington, Prepared for Dominican Sisters of Edmonds. (76 p).

Laprade, W.T., (1982). Geologic Implications of Pre-Consolidated Pressure Values, Lawton Clay, Seattle, Washington, Unpublished Report. (20 p).

Legros, F., (2002), The mobility of long-runout landslides, *Engineering Geology*, v. 63, p. 301-331.

Leroueil, S., Tavenas, F., and Lebihan, J. P., (1983), "Proprie´te´s Caracte´ristiques des Argyles de l'est du Canada," Canadian Geotech. Journal, Vol. 20(4), pp. 681–705.

Locat, J., and Demers, D., (1988), "Viscosity, Yield Stress, Remolded Strength and Liquidity Index Relationships for Sensitive Clays," Canadian Geotech. Journal, Vol. 25(4), pp. 799–806.

Major, J.J. and Iverson, R.M. 1999. Debris-flow deposition — effects of pore-fluid pressure and friction concentrated at flow margins. *Geological Society of America Bulletin* 111: 1424-1434.

McDougall, S., (2006), A new continuum dynamic model for the analysis of extremely rapid landslide motion across complex 3D terrain. Ph.D. Dissertation, Department of Earth and Ocean Sciences, University of British Columbia, Canada, 253 pp.

Mitchell, J. K. (1976). *Fundamentals of Soil Behavior*, 1st Edition, John Wiley and Sons, Inc.

Mitchell, J. K. (1993). *Fundamentals of Soil Behavior*, 2nd Edition, John Wiley and Sons, Inc.

Morgan, D.S., Jones, J.L., (1995). Numerical model analysis of the effects of groundwater withdrawals on discharge to streams and springs in small basins typical of Puget sound lowland, Washington. USGS Water Supply Paper W 2492 (73 p).

Morgenstern, N.R., Price, V.E., (1965). The analysis of the stability of general slip surfaces. Géotechnique 15 (1), 79–93.

Muir Wood, D. (1983). Index properties and critical state soil mechanics. In Proceedings of the Symposium on Recent Developments in Laboratory and Field Tests and Analysis of Geotechnical Problems, Bangkok, 6–9 December 1983. A.A. Balkema, Rotterdam, the Netherlands. pp. 301–309.

Muir Wood, D. (1990). Soil behaviour and critical state soil mechanics. Cambridge University Press, Cambridge, UK.

Mullineaux, D.R., Waldron, H.H., Rubin, M., (1965). Stratigraphy and chronology of late

interglacial and early Vashon glacial time in Seattle area, Washington. U.S. Geol.

Surv. Bull. 1194-0 (14 p).

National Research Council, (1985). Reducing losses from landsliding in the United States. Washington, D.C.: National Academy Press.

NGI (2002), "Early Soil Investigations for 'Fast Track Projects," Report 521553, Norwegian Geotechnical Institute, Oslo, Norway.

O'Kelly, Brendan C., (2013). "Atterberg Limits and Remolded Shear Strength—Water Content Relationships," Geotechnical Testing Journal, Vol. 36, No. 6, pp. 1–9.

O'Kelly, B. C., (2013a), "Characterisation and Undrained Strength of Amorphous Clay," Proceedings of the Institution of Civil Engineers, Geotechnical Engineering, Vol. 166.

Olsen, H.W. (1989). "Sensitive strata in Bootlegger Cove formation." *Journ. of Geotechnical Engrg.,* ASCE, 115(9), 1239-1251.

Palladino, D.J., Peck, R.B., (1972). Slope failures in an overconsolidated clay, Seattle, Washington. Géotechnique 22, 563–595.

Perlea, V., (2000), "Liquefaction of Cohesive Soils", ASCE, Soil Dynamics and Liquefaction, GSP 107, pp. 58-76.

Pierson,T . C., and J. E. Costa, (1987) A rheologic classification of subaerial sediment-water flows, in Debris Flows/Avalanches: Process Recognition and Mitigation, Rev. Eng. Geol., vol. 7, edited by J. E. Costa and G. F. Wieczorek, pp. 1-12, Geol. Soc. of Am., Boulder, Colo.

Polito, C.P., & Martin II, J.R. 2001. Effects of nonplastic fines on the liquefaction resistance of sands. *Journal of Geotechnical and Geoenvironmental Engineering.* 127 (5): 408–415.

Poulos, S. J., Castro, G., and France, J. (1985). "Liquefaction evaluation procedure." J. *Geotech. Engrg.,* 111(6), 772-792.

Pyles, M.R., Rogers, J.D., Bray, J.D., Skaugset, A., Storesund, R., Schlieder, G., (2016). Expert Opinion Report (SR 530 Landslide), Prepared for Washington State Attorney General Office. Vol. 295.

Rickenmann, D. (1999), Empirical relationships for debris flows, Natural Hazards, 19, pp. 47–77

Rickenmann, D. (2005), Runout prediction methods, M. Jakob, O. Hungr (Eds.), Debris-flow Hazards and Related Phenomena, Praxis, Chichester, UK, pp. 305–324.

Riemer. M. F. (1992). 'The effects of testing conditions on the constitutive behavior of loose, saturated sands under monotonic loading." PhD thesis, University of California, Berkeley.

Riemer, M.F., Collins, B.D., Badger, T.C., Toth, C., Yu, Y.C., (2015). Geotechnical soil characterization of intact quaternary deposits forming the march 22, 2014 SR-530 (Oso) landslide, Snohomish County, Washington. U.S. Geological Survey Open-File Report 2015-1089 25 p.

Riemer, M.F., (2016). Unpublished soil testing results, prepared for the Washington Office

of the Attorney General.

Sasitharan, S., Robertson, P. K., Sego, D. C., and Morgenstern, N. R. (1993), "Collapse behavior of sand." *Can. Geotech.* J., 30(4), 569-577.

Savage, W.Z., Morrisey, M.M., Baum, R.L., (2000a). Geotechnical properties for landslideprone Seattle-area glacial deposits. U.S. Geological Survey Open-File Report 00-28, 6.

Savage, W.Z., Baum, R.L., Morrissey, M.M., Arndt, B.P., (2000b). Finite-element analysis of the Woodway landslide, Washington. U.S. Geol. Surv. Bull. 218 (13 p).

Seattle Times. (2016). "Building toward disaster." ⟨http://projects.seattletimes.com/2014/building-toward-disaster/⟩ (Oct. 3, 2016).

Seed, H.B., Seed, R.B., Harder, L.F., and Jong, H.L. (1989). "Re-evaluation of the Lower San Fernando dam - Report 2: Examination of the post-earthquake slide of February 9, 1971." *Contract Report GL-89-2, US. Army Engineer WES, Vicksburg, Mississippi.*

Seed, R B., Cetin, K.O., Moss, R.E.S., Kammerer, A., Wu, J., Pestana, J., Riemer, M., Sancio, R.B., Bray, J.D., Kayen, R.E., & Faris, A. (2003). Recent advances in soil liquefaction engineering: a unified and consistent framework. Keynote presentation, *26th Annual ASCE Los Angeles Geotechnical Spring Seminar,* Long Beach, CA.

Shannon, W. D. (1952). "Report on slide on north fork Stillaguamish River near Hazel." U.S. Dept. of Game and Fisheries, Washington, DC.

Skempton AW. (1957). Discussion of the planning and design of the new Hong Kong airport. Proceedings of the Institution of Civil Engineers 1957;7:305-7.

Skempton, A.W., Hutchinson, J.N., (1969). Stability of natural slopes. Proceedings, 7th International Conference on Soil Mechanics, Mexico 3, 291–340.

Sladen, J.A., and Handford, G. (1987). A potential systematic error in laboratory testing of very loose sands. Canadian Geotechnical Journal, **24**: 462–466.

Stark, T.D. and Contreras, I.A. (1998). "Fourth Avenue landslide during 1964 Alaskan earthquake." J. *Geotech. and Geoenvironmental Engrg.,* ASCE, 124(2), 99-109.

Stark, T. D., and Hussain, M. (2013). "Drained shear strength correlations for slope stability analyses." J. Geotech. Eng., 10.1061/(ASCE)GT.1943-5606.0000824, 853–862.

Stark, T. D., Baghdady, A. K., Hungr, O., Aaron, J. (2017). "Case Study: Oso, Washington, Landslide of March 22, 2014—Material Properties and Failure Mechanism", ASCE, Downloaded from ascelibrary.org by University of Washington Libraries on 04/27/17.

Stephens, I., (2013), "Testing Procedure for Estimating Fully Softened Shear Strengths of Soils Using Reconstituted Material", US Army Corps of Engineers, ERDC/GSL GeoTACS TN-13-1

Steven L. Kramer, H. Bolton Seed, ASCE, (1988). *Journal of Geotechnical Engineering,* 114(4): 412-430

Sun, Q., Zhang, L., Ding, X., Hu, J., and Liang, H. (2015). "Investigation of slow-moving landslides from ALOS/PALSAR images with TCPInSAR: A case study of Oso, USA." Remote Sens., 7(1), 72–88.

Tanaka. T., Yasuhara, M., Sakai, H., and Marui, A. (1988). "The Hachioji experimental basin study-storm runoff processes and the mechanism of its generation." J. *Hydrol.,* 102(1-4), 139-164.

Tanaka H. (1994). Vane shear strength of a Japanese marine clay and applicability of Bjerrum's correction factor. Soils and Foundations;34(3):39-48.

Tart, R. G. (2016). "Why the Oso landslide caused so much death and destruction." Proc., 2016 Geotechnical and Structural Engineering Congress, ASCE, Reston, VA, 1545–1554.

Terzaghi, K., Peck, R. B., and Mesri, G., (1996), Soil Mechanics in Engineering Practice, 3rd edn. Wiley, NY.

Thevanayagam, S., and Martin, G.R. 2002. Liquefaction in silty soils—screening and remediation issues. Soil Dynamics and Earthquake Engineering, **22**: 1035–1042.

Thevanayagam, S., Shenthan, T., Mohan, S., & Liang, J. 2002. Undrained fragility of clean sands, silty sands, and sandy silts. *Journal of Geotechnical and Geoenvironmental Engineering*. 128 (10): 849–859.

Thorsen, G. W. (1969). "Landslide of January 1967 which diverted the north fork of the Stillaguamish River near Hazel." Dept. of Natural Resources, Geology and Earth Resources Division, Olympia, WA.

Tohno, I. and Yasuda, S. (1981). "Liquefaction of the ground during the 1978 Miyagiken-Oki earthquake." *Soils and Foundations,* 21 (3), 18-34.

Turabian, K. L. (1987). A Manual for Writers of Term Papers, Theses, and Dissertations. 5th ed. Chicago: The University of Chicago Press.

Vaid, Y.P., and Sivathayalan, S. (1996). Errors in estimates of void ratio of laboratory sand specimens. Canadian Geotechnical Journal, **33**: 1017–1020.

Varnes, D. J., (1978). Slope movement types and processes in Landslides—Analysis and Control, edited by R. L. Schustera nd R. J. Krizek, Spec. Rep. Natl. Res. Counc. Transp. Res. Board, 176, pp. 11-33, Natl. Acad. of Sci., Washington, D.C.

Wang, W. (1979). "Some findings in soil liquefaction." *Report Water Conservancy and Hydro-electric Power Scientific Research Institute,* Beij ing, China, 1 - 17.

Wang, W. (1981). "Foundation problems in aseismatic design of hydraulic structures." *Proc., Joint U.S.-P.R.C. Microzonation Workshop,* Harbin, China, 15- I - 15-13.

Wang, G., Sassa, K., 2001. Factors affecting rainfall-induced flowslides in laboratory flume tests. Ge´otechnique 51 (7), pp. 587–599.

Wartman, J., Montgomery, D., Anderson, S., Keaton, J., Benoit, J., deLaChapelle, J. and Gilbert, R. (2016), "The 22 March 2014 Oso Landslide, Washington, USA," *Geomorphology,* v. 253, pp. 275–288.] [Campbell, W. G. 1990. Form and Style in Thesis Writing, a Manual of Style. Chicago: The University of Chicago Press.

Weyman, D. R. (1973). "Measurements of the downslope flow of water in a soil." J. *Hydrol., 20(3/4), 267-288.*

Wroth, C. P., and Wood, D. M., (1978), "The Correlation of Index Properties With Some Basic Engineering Properties of Soils," Canadian Geotech. Journal, 15(2), pp. 137–145.

Yang, S. L., Kvalstad, T., Solheim, A., and Forsberg, C. F., (2006), "Parameter Studies of Sediments in the Storegga Slide Region," Geo-Marine Letters, Vol. 26(4), pp. 213–224.

Yang, S.L., Sandven, R., Grande, L., (2006). "Steady-state lines of sand-silt mixtures.", Canadian Geotechnical J., 43(11): 1213-1219.

Yilmaz, I., (2000), "Evaluation of Shear Strength of Clayey Soils by Using Their Liquidity Index," Bulletin of Engineering Geology and the Environment, Vol. 59(3), pp. 227–229.

Zentar, R., Abriak, N.-E., and Dubois, V., (2009), "Fall Cone Test to Characterize Shear Strength of Organic Sediments," ASCE Geotech. and Geoenviron. Eng., Vol. 135(1), pp. 153–157.]

Vita

Ahmet Ali Mert was born in Mersin, Turkey, and raised in various Turkish cities. He graduated from Yesilkoy Anatolian High School in Istanbul in 2007 and began attending Eskisehir Technical University (f.k.a. Anadolu University) in Fall 2007. He lived in the Czech Republic for one semester as an exchange student in Civil Engineering in 2010. He graduated in Civil Engineering and Environmental Engineering (second major) at Eskisehir Technical University in June 2012. After working as a civil and geotechnical engineer for about four years, and completing his Master's degree coursework at Istanbul Technical University, he started his graduate education in Geotechnical Engineering at the University of Texas in Spring 2017.

Email: ahmetalimert@gmail.com

This thesis was typed by the author.